Monodisperse Platinum and Rhodium Nanoparticles as Model Heterogeneous Catalysts

by

Michael Edward Grass

B.A. (Pomona College) 2002

A dissertation submitted in partial satisfaction of the

requirements for the degree of

Doctor of Philosophy

in

Chemistry

in the

Graduate Division

of the

University of California, Berkeley

Committee in charge:

Professor Gabor A. Somorjai, Chair
Professor Peidong Yang
Professor Alexis T. Bell

Fall 2008

The dissertation of Michael Edward Grass is approved:

Chair _____ Date _____

_____ Date _____

_____ Date _____

University of California, Berkeley

Fall 2008

Monodisperse Platinum and Rhodium Nanoparticles as Model Heterogeneous Catalysts

by Michael Edward Grass

Abstract

Monodisperse Platinum and Rhodium Nanoparticles as Model Heterogeneous Catalysts

by

Michael Edward Grass

Doctor of Philosophy in Chemistry

University of California, Berkeley

Gabor A. Somorjai, Chair

Model heterogeneous catalysts have been synthesized and studied to better understand how the surface structure of noble metal nanoparticles affects catalytic performance. In this project, monodisperse rhodium and platinum nanoparticles of controlled size and shape have been synthesized by solution phase polyol reduction, stabilized by polyvinylpyrrolidone (PVP). Model catalysts have been developed using these nanoparticles by two methods: synthesis of mesoporous silica (SBA-15) in the presence of nanoparticles (nanoparticle encapsulation, NE) to form a composite of metal nanoparticles supported on SBA-15 and by deposition of the particles onto a silicon wafer using Langmuir-Blodgett (LB) monolayer deposition. The particle shapes were analyzed by transmission electron microscopy (TEM) and high resolution TEM (HRTEM) and the sizes were determined by TEM, X-ray diffraction (XRD), and in the case of NE samples, room temperature H_2 and CO adsorption isotherms. Catalytic studies were carried out in homebuilt gas-phase reactors. For the nanoparticles supported on SBA-15, the catalysts are in powder form and were studied using the homebuilt

systems as plug-flow reactors. In the case of nanoparticles deposited on silicon wafers, the same systems were operated as batch reactors.

The NE Pt nanoparticles of controlled size were used to study particle size dependent reactivity for hydrogenation reactions. The influence of particle size on selectivity was examined with crotonaldehyde hydrogenation. For the hydrogenation of crotonaldehyde at temperatures near 373 K and pressures of 200 Torr H_2 and 8 Torr crotonaldehyde, the selectivity towards crotyl alcohol (selective hydrogenation of the aldehyde functionality) increases as particle size increases. This observation is consistent with theoretical studies that the carbonyl group has more interaction with the close-packed (111) face of Pt than the more open (100) surface. The affect of reduction temperature was also studied over 1.7 and 7.1 nm Pt nanoparticles. At reduction temperatures of 673 – 723 K, the turnover frequency and selectivity to crotyl alcohol both reach a maximum. TEM analysis indicates that there is no sintering of Pt nanoparticles and it is known that there is no metal support interaction between Pt and SiO_2. Thus, the dependence on reduction temperature is attributed to an interaction between crotonaldehyde and residual carbon from PVP decomposition on the Pt nanoparticle surface.

Furthermore, simultaneous hydrogenation and dehydrogenation of cyclohexene in excess H_2 was examined over the same size range of Pt nanoparticles between 273 and 650 K and at 10 Torr cyclohexene in 200 – 600 Torr H_2. The conversion of cyclohexene in the presence of excess H_2 is characterized by three regimes: hydrogenation of cyclohexene to cyclohexane at low temperature (< 423 K), an intermediate temperature range in which both hydrogenation and dehydrogenation occur; and a high temperature

regime in which the dehydrogenation of cyclohexene dominates (> 573 K). The rate of both reactions demonstrated maxima with temperature, regardless of Pt particle size. Hydrogenation is structure *insensitive* at low temperatures, and apparently structure *sensitive* in the non-Arrhenius regime; the origin of the particle-size dependent reactivity with temperature is attributed to a change in the coverage of reactive hydrogen. Small particles were more active for dehydrogenation and consistently had lower apparent activation energies than large particles. The selectivity can be controlled by changing the particle size, which is attributed to the structure sensitivity of *both* reactions in the temperature regime where hydrogenation and dehydrogenation are catalyzed simultaneously.

Shape control of Pt nanoparticles was achieved through the addition of Ag^{+} ions during polyol reduction of Pt^{x+} ions. Changing the ratio of Ag^{+} ions to Pt^{x+} ions in solution led to the selective growth of Pt cubes, cuboctahedra, or octahedra, obtaining shape selectivity ≥80% in all cases. The cubes are terminated by (100) faces, the octahedra by (111) faces, and the cuboctahedra by both. These nanoparticles were encapsulated in mesoporous silica by NE and tested for ethylene hydrogenation; the TOF for ethylene hydrogenation decreased with increasing Ag remaining in the catalysts. In order to study the influence of particle shape on catalyst selectivity, a nitric acid etching procedure was developed that effectively removes the Ag from the catalysts and increases the rate of ethylene hydrogenation by up to 3 orders of magnitude. Nitric acid etching of Ag from the Pt nanoparticles is > 90% effective when [HNO_3] is greater than 7 M, but is ineffective below this concentration. This process was monitored with elemental analysis and ethylene hydrogenation. HRTEM and CTEM confirmed that the Pt nanoparticles

themselves do not etch and the shapes of the particles are preserved throughout the etching procedure.

Rh nanoparticles in the size range of 2 – 14 nm (relative standard deviation in size ~ 10%) were deposited onto silicon wafers by LB and onto SBA-15 by NE, and investigated for the hydrogenation of ethylene and the oxidation of CO by O_2. Ethylene hydrogenation rates were independent of Rh particle size, consistent with the structure insensitivity of ethylene hydrogenation. CO oxidation rates for the LB samples increased by an order of magnitude as the particle size decreased from 14 nm to 2.5 nm. In order to help explain this particle size dependence, synchrotron based X-ray photoelectron spectroscopy was performed during CO oxidation. Under these conditions, smaller (1.9 nm) Rh nanoparticles exhibited 0.6 of a monolayer of oxidized Rh at 423 K and a full monolayer of oxidized Rh at 473 K. Larger (7.1 nm) Rh nanoparticles contained only 0.2 and 0.6 of a monolayer at 423 K and 473 K, respectively. The deeper oxidation of smaller particles coincides with an increase in the reaction rate. A simple thermodynamic model for the oxidation of metal nanoparticles was also developed, which demonstrates that smaller nanoparticles oxidize more easily than larger nanoparticles.

A series of Rh nanoparticles between 1.9 and 11.3 nm was also supported on mesoporous silica SBA-15 for a continued study of the size dependence of CO oxidation as well as a study of the role of PVP in gas phase catalysis. The deposition of the particles on SBA-15 allows for the ability to treat the nanoparticles at high temperatures in O_2 and/or H_2 without sintering of the particles, which occurs easily on the silicon wafers. PVP stabilized Rh NP catalysts were studied for CO oxidation before and after calcination in O_2 at ~ 673 K. Uncalcined PVP stabilized Rh NP catalysts exhibit a higher

turnover frequency for CO oxidation than calcined catalysts. Additionally, the turnover frequency for CO oxidation increases with decreasing particle size from 11 to 2 nm for uncalcined catalysts, but is particle size independent for calcined catalysts. CO adsorbs at bridge sites before the catalysts are calcined, but on atop sites after calcination, with or without reduction in H_2 as monitored by infrared spectroscopy. By comparing infrared studies to turnover frequency measurements for CO oxidation, we propose that PVP affects how CO binds to Rh and thus affects the turnover frequency for CO oxidation.

This dissertation has focused on the synthesis, characterization, and reaction studies of model noble metal heterogeneous catalysts. Careful control of particle size and shape has been accomplished though solution phase synthesis of Pt and Rh nanoparticles in order to elucidate further structure-reactivity relationships in noble metal catalysis.

Dedicated to my wife, Becky

Table of Contents

List of Figures and Tables

Acknowledgements

There are many people who have supported me throughout my work at the University of California, Berkeley. Foremost, I would like to thank my advisor, Professor Gabor A. Somorjai. Professor Somorjai has been a caring advisor who is always available to talk about science or life. Without him, none of this would be possible and I am greatly indebted to his generosity.

I owe a great deal over the past four years to my wife Becky. She has been a great support for me while working towards my doctorate, especially at times when I was frustrated or depressed. We have built a home and a life together over the past three years of marriage, and I look forward to many more to come.

While at Berkeley, I have had the pleasure of working with many amazing people, including professors, staff scientists, postdoctoral scientists, graduate students, and undergraduates. Professor Robert M. Rioux was a senior graduate student when I joined the group and he taught me a great deal about catalysis and careful experimental techniques that I have used throughout my time here. I owe Rob a great deal and it has been a pleasure to continue to collaborate with him after his graduation. Professor James Hoefelmeyer and Dr. Kristian Niesz were also members of the lab when I joined and they taught the synthesis of mesoporous materials and metal nanoparticles. All three are also good friends and helped me get started in my graduate research.

Dr. Simon Humphrey worked with me in a study of Rh nanoparticles for crotonaldehyde hydrogenation and was also a good gym partner and got me outside to kick around the soccer ball. Professor Yawen Zhang was the main designer of the Rh synthesis presented in this dissertation and he has been a pleasure to work with on

catalytic studies of noble metal nanoparticles. He is very talented at nanoparticle synthesis. I have spent many hours with Derek Butcher, Dr. Feng Tao, Dr. Katie Bratlie, Dr. Jeong Park, Russ Renzas, Dr. Matthias Koebel, Dr. B. Simon Mun, and Dr. Zhi Liu at the ALS working on ambient pressure XPS. I would especially like to thank Derek for many long conversations about XPS, research in general, and life in even more generality. Simon and Zhi have also been invaluable resource in these projects and have been kind enough to let me work with them next year at the ALS. Dr. Susan Habas performed all of the HRTEM in this dissertation and has been a pleasure to work with over the past few years. Hopefully we can continue to collaborate during our postdoctoral work. Special thanks is also due to Prof Peidong Yang, who has been a second advisor for much of my time in graduate school.

Two undergraduates who worked in the lab were very talented and hard working. I owe a great deal of thanks to Chelsea Teall and Yao Yue.

I would also like to acknowledge Dr. Yimin Li, Dr. Sang Hoon Joo, Dr. John Kuhn, Dr. Chia-Kuang (Frank) Tsung, Dr. Wenyu Huang, Dr. Hyunjoo Lee, Dr. Yusuke Yamada, Tianfu Zhang, George Holinga, Chris Kliewer, Dr. Yuri Borodko, Dr. Sasha Kweskin, Dr. Max Montano, Dr. Anthony Contreras, Antione Hervier, Dr. Hyun Sook Lee, Miki Kunitake, Prof Heinz Frei, and Prof Miquel Salmeron for helpful discussions, fruitful collaborations, or just a good time.

Additionally, I would like to thank those who have provided me with the ability to get to where I am now. My undergraduate advisor, Prof Fred Grieman taught me a great deal about chemistry and research at Pomona College and has been a great help in the last four years as well. Prof Dan O'Leary also deserves a great deal of thanks, as his

excellent teaching and interest in my well being led me to major in chemistry eight years ago.

My family has been a great inspiration and support for me leading up to and throughout graduate school. My parents, Gene and Carol, have been supported of everything I have done and have never put any expectations on me except to excel and be the best person I can be. My mother and father-in-law, Robin and Terry Prechter, have also been very supported with their time and encouragement. Paul, Anna, Peggy, Paul, and Sarah are the best siblings and siblings-in-law that anyone could ask for.

There are numerous more friends, family, and colleagues who have inspired me, helped me out in hard times, or provided valuable conversations. I thank everyone who has helped me in this journey.

Lastly, I would like to acknowledge the funding source for this project. This work was supported by the Director, Office of Science, Office of Advanced Scientific Computing Research, Office of Basic Energy Sciences, Chemical Sciences, Geosciences, and Biosciences Division, of the U.S. Department of Energy under Contract No. DE-AC02-05CH11231.

Chapter 1: Introduction

The activity and selectivity of a heterogeneous catalyst can be affected by many parameters, including reaction temperature, pressure, and flow rates, catalyst loading and morphology, and addition of promoters or poisons. One question that has been raised in the heterogeneous catalysis community since the 1930s is how the morphology of small metal crystallites influences catalytic performance. In the 1950s, Borsekov and coworkers perfected the measurement of active metal surface area on catalysts by using selective hydrogen adsorption (chemisorption), which allowed them to study the affects of platinum particle size in the oxidation of sulfur dioxide and hydrogen.[1,2]

Beginning in the 1960s, Boudart made many advancements in the understanding of the dependence of particle size on both the activity and selectivity for supported catalysts.[3,4] Boudart made a distinction between reactions for which particle size, or metal dispersion, changed the rate or selectivity for the reaction dramatically and those reactions for which particle size did not greatly affect the reaction. He called the former reactions structure sensitive and the latter he termed structure insensitive. While in reality, most reactions fall somewhere along a continuum between completely structure insensitive and extremely structure sensitive, this has proved to be a useful distinction through the years. When single crystals became a standard of model heterogeneous catalysts, the definition of structure sensitivity was expanded to cover changes in reaction rate or selectivity over different crystal faces.[5]

Many reactions have been investigated over the past half century and have been classified as either structure sensitive or structure insensitive. For example, ethylene hydrogenation over Pt is structure insensitive[6] and has been used as such as a benchmark

reaction in many studies of heterogeneous catalysis.[7-9] Ethane hydrogenolysis over Pt, however, is structure sensitive[10] and has also been studied in many systems as a model recaction.[11,12] For certain reactions, however, the distinction between structure sensitive and insensitive appears to be inextricably linked to reaction temperature, pressure, and "catalyst history." CO oxidation by O_2 is one such reaction, for which some reports on this reaction catalyzed by Rh have emphatically stated its structure insensitivity[13-15] while others claim that it is structure sensitive.[16,17]

This study is concerned with the structure sensitivity of the hydrogenation of ethylene to ethane, crotonaldehyde to crotyl alcohol and butyraldehyde, cyclohexene to benzene and cyclohexene, and oxidation of CO by O_2 to CO_2 over a relatively new class of catalysts: polymer stabilized noble metal nanoparticles.[18] One of the advantages of this method of catalyst preparation that is often cited is the control of particle size that can be achieved using this method. Colloidal routes to the formation of nanoparticles for supported catalysts give rise to a much narrower particle size distribution (PSD) than for nanoparticles formed by traditional catalyst preparation methods, such as wetness impregnation or ion exchange. Using this technique for the synthesis of Pt and Rh nanoparticles, we have investigated the structure sensitivity of these reactions over Pt and Rh, and also investigated the role that the stabilizing polymer plays in gas phase catalysis.

Building on previous work in this group,[12,19,20] we synthesized Pt and Rh NPs stabilized by poly(vinylpyrrolidone) (PVP) between 1.5 and 15 nm and supported them on mesoporous silicon dioxide SBA-15 for the investigation of gas phase catalysis. In Chapter 2, the synthesis of these materials is described in detail along with many of the characterization techniques used, which range from gas sorption to synchrotron based

photoelectron spectroscopy. Chapter 3 is concerned with the hydrogenation of crotonaldehyde over a series of Pt NPs between 1.7 and 7.1 nm supported on SBA-15; the role of particle size and interactions of PVP with the Pt surface and crotonaldehyde are both discussed. We also studied a similar series of Pt NPs supported on SBA-15 for cyclohexene hydrogenation-dehydrogenation and found this reaction to be very structure sensitive in the temperature range where both products are formed simultaneously (400 K $\leq$ T $\leq$ 550 K).

The synthesis of shape controlled Pt nanoparticles is discussed in Chapter 5. Cubes, cuboctahedra, and octahedra were synthesized in the presence of Ag^{+} ions and the removal of Ag was necessary to achieve high activity for ethylene hydrogenation. The removal of Ag was monitored by elemental analysis and ethylene hydrogenation while the structure of the Pt nanoparticles was monitored with transmission electron microscopy (TEM) and X-ray diffraction (XRD).

Chapters 6, 7, and 8 are all focused on the catalytic properties of PVP stabilized Rh NPs. The synthesis of particles between 5 and 15 nm, formation of 2-dimensional films, and reactivity for ethylene hydrogenation is discussed in Chapter 6. The nanoparticles are terminated by (111) faces and all exhibit a low PSD.

The role of particle size and PVP in the oxidation of CO by O_2 is discussed in chapters 7 and 8. The synthesis of Rh nanoparticles of controlled size was extended to 1.9 nm and characterized with TEM. The rate of reaction between CO and O_2 increases by an order of magnitude with decreasing particle size from 11 nm to 2 nm and this rate increase is correlated with an increase in the amount of surface Rh in a higher oxidation state, as monitored by ambient pressure X-ray photoelectron spectroscopy. The effect of

PVP on the activity and particle size dependence was investigated by employing different pretreatments of the Rh catalysts and analyzing the resulting surface with infrared spectroscopy. Although the data is not completely understood, it appears that PVP plays an important role in directing the catalytic properties of the Rh nanoparticles.

References

(1) Boreskov, G. K.; Slinko, M. G.; Chesalova, V. S. *Zh. Fiz. Khim.* **1956**, *30*, 2787.

(2) Chesalova, V. S.; Boreskov, G. K. *Zh. Fiz. Khim.* **1956**, *30*, 2560.

(3) Boudart, M.; Aldag, A.; Benson, J. E.; Doughart.Na; Harkins, C. G. *J. Catal.* **1966**, *6*, 92.

(4) Boudart, M.; Aldag, A. W.; Ptak, L. D.; Benson, J. E. *J. Catal.* **1968**, *11*, 35.

(5) Somorjai, G. A.; Carazza, J. *Ind. Eng. Chem. Fundam.* **1986**, *25*, 63.

(6) Zaera, F.; Somorjai, G. A. *J. Am. Chem. Soc.* **1984**, *106*, 2288.

(7) Grunes, J.; Zhu, J.; Yang, M. C.; Somorjai, G. A. *Catal. Lett.* **2003**, *86*, 157.

(8) Zaera, F. *Langmuir* **1996**, *12*, 88.

(9) Zaera, F.; Janssens, T. V. W.; Ofner, H. *Surf. Sci.* **1996**, *368*, 371.

(10) Guczi, L.; Gudkov, B. S. *React. Kinet. Catal. Lett.* **1978**, *9*, 343.

(11) Bond, G. C.; Paal, Z. *Appl. Catal. A: Gen.* **1992**, *86*, 1.

(12) Rioux, R. M.; Song, H.; Hoefelmeyer, J. D.; Yang, P.; Somorjai, G. A. *J. Phys. Chem. B* **2005**, *109*, 2192.

(13) Oh, S. H.; Eickel, C. C. *J. Catal.* **1991**, *128*, 526.

(14) Peden, C. H. F.; Goodman, D. W.; Blair, D. S.; Berlowitz, P. J.; Fisher, G. B.; Oh, S. H. *J. Phys. Chem.* **1988**, *92*, 1563.

(15) Santra, A. K.; Goodman, D. W. *Electrochim. Acta* **2002**, *47*, 3595.

(16) Hopstaken, M. J. P.; Niemantsverdriet, J. W. *J. Chem. Phys.* **2000**, *113*, 5457.

(17) Nehasil, V.; Stara, I.; Matolin, V. *Surf. Sci.* **1996**, *352*, 305.

(18) Aiken, J. D.; Finke, R. G. *J. Mol. Catal. A: Chem.* **1999**, *145*, 1.

(19) Rioux, R. M.; Song, H.; Grass, M.; Habas, S.; Niesz, K.; Hoefelmeyer, J. D.; Yang, P.; Somorjai, G. A. *Top. Catal.* **2006**, *39*, 167.

(20) Song, H.; Rioux, R. M.; Hoefelmeyer, J. D.; Komor, R.; Niesz, K.; Grass, M.; Yang, P. D.; Somorjai, G. A. *J. Am. Chem. Soc.* **2006**, *128*, 3027.

Chapter 2: Experimental Techniques

2.1 Synthetic Techniques

2.1.1 Alcohol/Polyol Synthesis of Noble Metal Nanoparticles

The use of noble metal nanoparticles (NPs) or colloids dates back to Roman times and colloidal gold and silver have been used in many ancient works of art. The first scientific paper on the subject was by Michael Faraday in 1857.[1] Reduction of metal precursors by alcohols to form metal NPs stabilized by organic ligands began in 1978 with the work of Hirai, *et al*.[2] The formation of monodisperse NPs can by obtained by this route, usually employing a reducing agent (the alcohol or polyol), a metal precursor (salt, acid, or organometallic molecule), and a stabilizing (or capping) agent which keeps the NPs from aggregating in solution. In Hirai's initial work, Rh colloids were formed by reduction of $RhCl_3$ by methanol in the presence of poly(vinyl alcohol) (PVA) and he later extended this method to formation the of Pd, Os, Ir, and Pt NPs stabilized by PVA, poly(vinylpyrrolidone) (PVP), gelatin, and other polymers.[3] There are two stages to the NP synthesis – nucleation and growth – which can each be controlled in order to tailor the size and shape of the resulting NPs. Additionally, these two stages can be separated (temporally or spatially) by the "seeded growth" method whereby small NP "seeds" are first synthesized, followed by a separate growth step when additional metal precursors are added.[4] Two recent reviews have been written regarding the synthesis of metal nanoparticles.[5,6]

One of the most studied systems and the basis for many of the synthetic procedures in this thesis is the formation of noble metal nanoparticles using PVP as a stabilizing agent. In this work, two different molecular weights of PVP have been

employed (29K, ~290 monomer units and 55K, ~550 monomer units). PVP stabilizes the metal NPs by binding to the surface of the growing nanoparticles and sterically hindering them from contacting each other. PVP can bind to a metal surface either through the carbonyl or the tertiary amine of the pyrrolidone ring via covalent interactions at the surface (Figure 2.1). It is also believed that PVP complexes with the metal ions in solution and thus is important even in the nucleation stage of NP synthesis, not simply acting as a stabilizing agent.

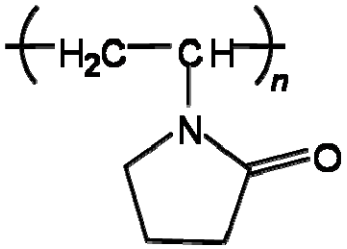

Figure 2.1. Structure of PVP

In a typical synthesis, a designated amount of metal precursor and PVP (usually in a ratio of ~ 10:1 PVP monomers to metal ions) are dissolved in methanol, ethanol, ethylene glycol, or 1,4-butanediol and heated to the desired reaction temperature (80 – 230 °C) for 1-3 h. The initial reduction is visible by eye as the solution changes color from that of the coordinated metal ions to a dark brown (in the case of Pt and Rh) indicative of metal NP formation. This color change usually occurs within 1 – 30 min of heating and the remainder of the reaction time involves the final stages of NP growth and Ostwald ripening.

2.1.2 Synthesis of Mesoporous Silica SBA-15

Mesoporous oxides such as MCM-41[7] and SBA-15[8] have been developed for applications such as catalysis and provide well-defined pores of 2-50 nm. SBA-15 was developed by Zhao, *et al.*[9] and characterized in depth by Kruk and Jaroniec[10]; it is

mesoporous silica with a pores size of ~ 10 nm and pore walls ~ 3 nm thick. An organic surfactant is used as a template for the formation of a porous oxide. In the case of SBA-15, a poly(ethylene oxide)-poly(propylene oxide)-poly(ethylene oxide) triblock copolymer, P123 ($(EO)_{20}(PO)_{70}(EO)_{20}$) forms rod micelles in aqueous solution above the critical micelle concentration (CMC) and hydrolysis of the silica precursor, tetramethyl orthosilicate (TMOS) is catalyzed by hydrochloric acid (HCl) on the periphery of the micelles. The templating material is removed with an ethanol wash and high temperature calcination (Figure 2.2).

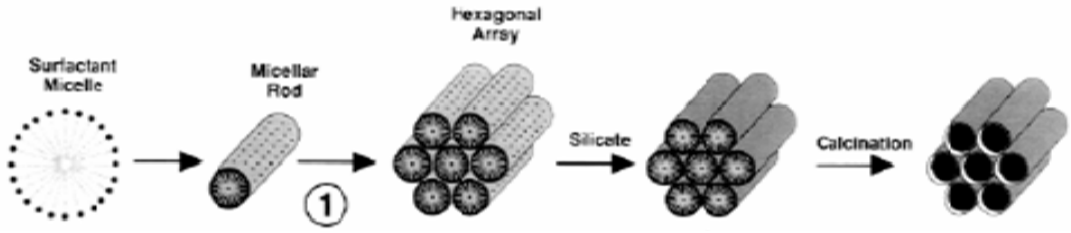

Figure 2.2. Cartoon of mesoporous oxide synthesis.[8]

2.1.3 Synthesis of Noble Metal/SBA-15 Catalysts

Two methods have been developed for incorporation of the preformed noble metal NPs into SBA-15. Capillary inclusion (CI) involves loading the NPs into SBA-15 by capillary action by combining NPs and SBA-15 in a 50/50 mixture of ethanol and water and submitting this solution to low power ultrasonication followed by drying in air.[11] The second method, termed nanoparticle encapsulation (NE), involves a neutral condition synthesis of SBA-15 (MSU-3[12]) in the presence of the NPs using NaF as the catalyst for TMOS hydrolysis to avoid highly acidic conditions that can degrade the Pt/PVP NPs.[13]

2.1.4 Langmuir Blodgett Formation of 2-D Film Catalysts

The Langmuir-Blodgett (LB) technique is one of a number of approaches to produce monolayer films of nanoparticles on solid substrates.[14] In a typical LB experiment, the metal NPs are deposited onto water in a Teflon coated LB trough from a non-aqueous solution (preferably a non-miscible fast evaporated solvent such as $CHCl_3$), resulting in a loose film of NPs on the surface of the water. A mobile Teflon barrier is moved to controllably compress this film to form a monolayer of a desired density while monitoring the surface pressure using a Wilhelmy plate (Figure 2.3). The plate can be made of glass, platinum, or a rectangular piece of filter paper. The force on the plate due to wetting is measured used to calculate the surface tension at the air-water interface:

$$\sigma = \frac{F}{l\cos\theta} \tag{2.1}$$

F is the force on the plate, σ the surface tension, l the wetted length of the Wilhelmy plate, and θ the contact angle of the water and the plate. A series of films transferred to TEM grids at varying surface tensions can then be used to calibrate film density versus surface tension for a given sample.[15] A schematic of this procedure is sketched in Figure 2.2.

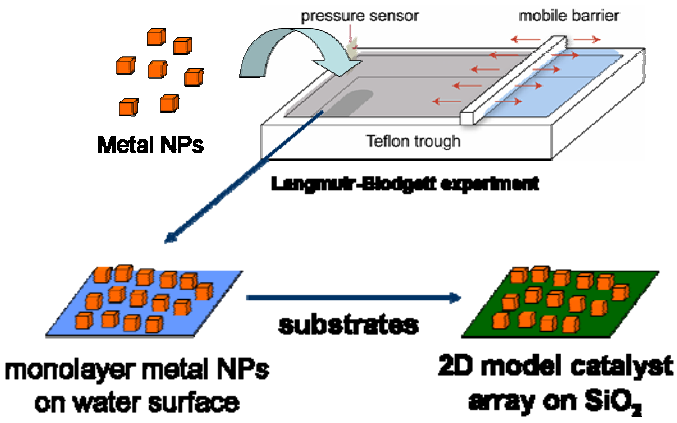

Figure 2.3. Schematic of Langmuir-Blodgett technique for the formation.

2.2 Catalytic Reactions

2.2.1 Reactor Systems

Four home-built reactor systems have been used for this work. Three of these systems are nearly identical and are composed of a set of mass flow controllers (MFC; Porter or MKS), permanent plumbing of either ⅛" stainless steel or ¼" glass tubing with Swagelok connections and valves (SS) or Kontes valves (glass), respectively. Each system is equipped with a recirculation pump for the option of batch operation and an HP 5890 Series II gas chromatograph with flame ionization (FID) and thermal conductivity (TCD) detectors for online gas analysis. A syringe pump or saturator was placed in line with the He gas flow when utilizing liquid reactants (Figure 2.4). The reactor cell is a quartz or pyrex U-tube reactor with a quartz frit. A stainless steel reactor cell was designed for the 2D samples with an external heater. While with cell has better gas flow across the sample, the Kapton heaters used have a maximum temperature of ~150 °C and temperatures below room temperature are not easily accessed (Figure 2.5).

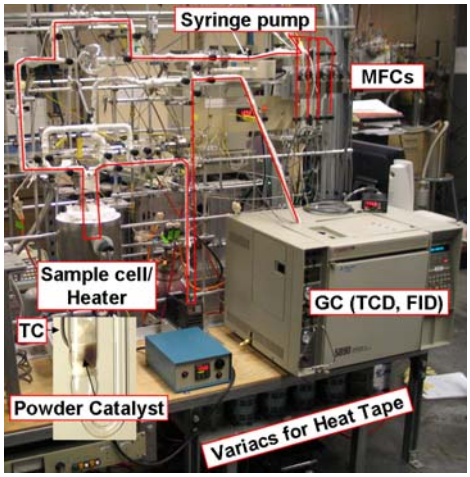

Figure 2.4. Reactor setup with red lines indicating gas flow for a flow reaction

The heaters for the reaction cells were built by Therm-X and are controlled with Watlow 96 temperature controllers. The temperature can now be operated via PC

through a homemade LabView program on two of the systems. On two systems, the MFCs are also run through LabView. The mass flow controller flow rates are calibrated using a bubble meter twice a year. For the PC operated MFCs, this calibration factor is set directly in the program. For the other system, the correction factors are entered into an excel file that can be used to determine the appropriate set point for the control box.

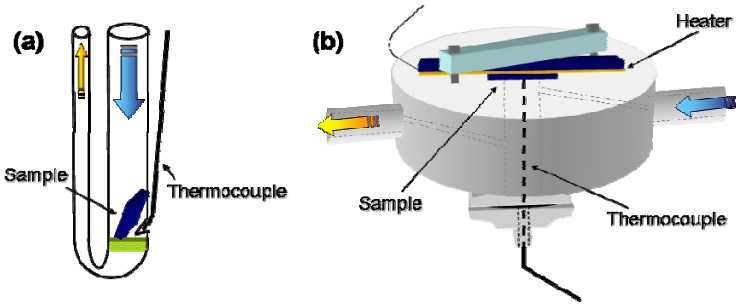

Figure 2.5. (a) U-tube (quartz) and (b) stainless steel reactor cells for 2D catalysts

2.2.2 Flow Reactions

For reactions involving the 3D catalysts (noble metal/SBA-15), a tubular reactor design referred to as a plug-flow reactor (PFR) was used. The assumption for a PFR is that the gas flow is highly turbulent and there is no radial variation in concentration.[16] In the axial direction (along the length of the reactor), the concentration changes as reactant molecules are consumed and product molecules created by catalyst present upstream of the section considered. The overall mole balance for a PFR is thus given by Equation 2.2.

$$F_{j0} - F_j + \int^V r_j dV = \frac{dN_j}{dt} \tag{2.2}$$

F_{j0} is the flow rate of molecule j into the system, F_j is the flow rate of j at a given recactor position, and r_j is the rate of formation of j as a function of position in the reactor. When the reactor is operated at steady state, we obtain an equation for finding the reaction rate:

$$\frac{dF_j}{dV} = r_j \tag{2.3}$$

In order to simplify reactor design and data analysis, the PFR is operated under differential conditions. In a differential reactor, a small amount of catalyst is used and low conversion is maintained (in practice, this typically means < 10% conversion) so that the concentration of gases across the length of the catalyst bed can be approximated to be equal. The temperature is also assumed to be constant; in other words, the reactor is gradientless. Under these conditions and again assuming steady state conditions, a simple expression for the rate of reaction can be given as:

$$r_A = \frac{F_{Ae} - F_{A0}}{W} \tag{2.4}$$

F_{A0} and F_{Ae} are the flow rate into and out of the reactor, respectively, and W is the weight of the catalyst. W can be replaced by active metal surface area, total metal atoms, or any other appropriate measure of the amount of catalyst.

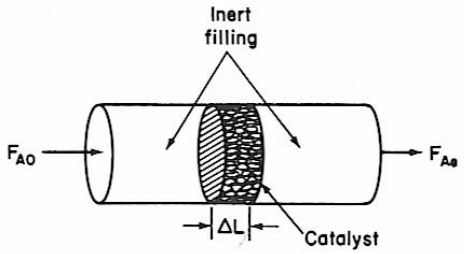

Figure 2.6. Differential plug flow reactor.[16]

2.2.3 Batch Reactions

In a batch reactor, products generally accumulate over time and the concentration of reactants decreases. At any given time t, the moles of some species A inside the reactor, N_A, is:

$$N_A = N_{A0} - N_{A0}X \tag{2.5}$$

N_{A0} is the moles of A at time $t = 0$ and X is the conversion of A. The rate of reaction can easily be obtained as:

$$N_{A0}\frac{dX}{dt} = -r_A V \tag{2.6}$$

There are many methods for calculating the rate of reaction. One of the most versatile methods and the one used for the majority of the batch reactor work in this thesis is to extrapolate the rate to time $t = 0$.

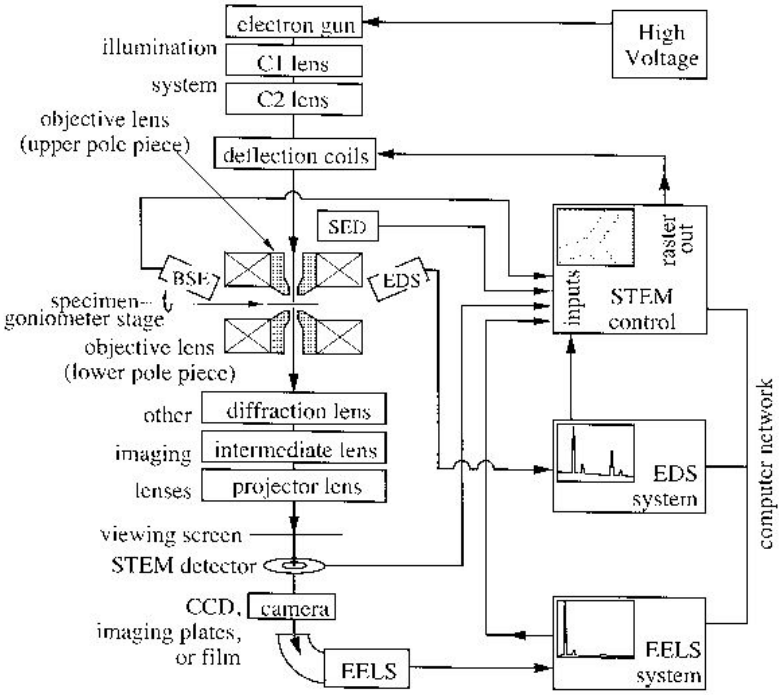

Figure 2.7. Schematic of a transmission electron microscope.[17]

2.3 Transmission Electron Microscopy

Transmission electron microscopy (TEM) has been the analytical workhorse of nanostructured materials for the past three decades. Many crucial parameters of metal nanoparticles can be elucidated using TEM, including the particle size distribution (PSD) and particle shape. High resolution TEM (HRTEM) can be used to determine particle size, shape, and surface structure more precisely. The interface between metal nanoparticles and a support can also be studied with TEM and HRTEM.

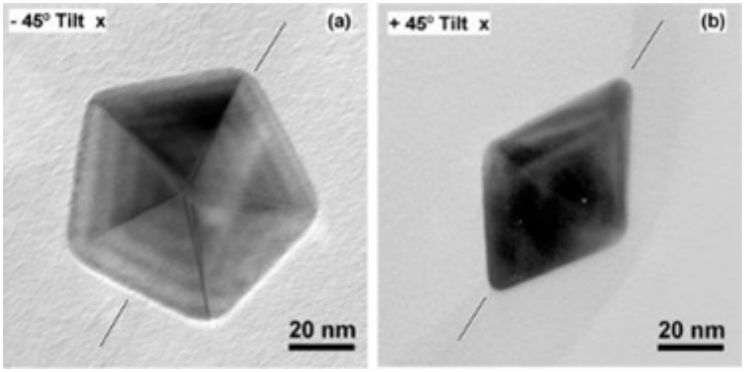

Figure 2.8. TEM image of icosahedral Au NP at two orientations demonstrates difficulty in determining shape and size by TEM.

A schematic of the essential features of a TEM is shown in Figure 2.7. The high voltage is typically set between 100 and 300 kV, generating 100 – 300 keV electrons, although this can be as high as 1000 kV. A TEM can be operated in many different modes and can combine many analytical techniques, making it a very versatile tool for the composition and structure of nanoscale materials. A conventional TEM (CTEM) works analogously to a light microscope, wherein all transmitted and diffracted beams combine to form an image at the viewing screen, but this results in weak contrast. If an aperture is placed in the back focal plane, better contrast in obtained. If the aperture is placed to allow only the transmitted (un-diffracted) electrons, a bright-field (BF) image is formed. If the aperture is placed to allow only a set of diffracted electrons, a dark-field (DF) image is formed. In a BF image, areas which are thick and/or made of a high-Z material will appear darkest. In a DF image, the areas which have caused diffraction in the selected direction will appear brightest; this can be very useful when determining the orientation of crystallites and defects. In HRTEM, the transmitted (forward scattered) beam and at least one diffracted beam are collected. These beams result in an interference pattern, which must be translated into an image, giving rise to the other name for HRTEM, phase contrast imaging.[17] It is important to note that HRTEM does not

"image" individual atoms, but rather gives interference patterns generated by columns of atoms.TEM is the most common tool for determination of PSD, despite other tools (size exclusion chromatography, X-ray scattering, light scattering) and reports that particles of different sizes can segregate on a TEM grid, hindering a true PSD analysis by TEM.[6] Another concern for determining PSD by TEM is in determining the size of non-spherical NPs. In addition to the obvious confusion regarding how to define the size of a faceted particle, two identical particles that are oriented differently on a TEM grid will appear to be of different sizes, thus giving an apparent distribution of sizes even for identical particles. Orientation must be carefully considered, particularly when determining the shape of NPs, as illustrated in Figure 2.8.

2.4 Scanning Electron Microscopy

Similar to TEM, scanning electron microscopy (SEM) involves impinging high energy electrons on a sample and detecting resultant electrons. SEM typically utilizes 1 – 15 keV electrons and detects either backscattered (composition resolution, ~1-15 keV) or secondary electrons (relief resolution, ~1-50 eV). The electron beam is scanned in a raster pattern across the surface and the resulting electrons (backscattered or secondary) are detected. Secondary electrons are generated from inelastic interactions between the incident electron beam and the valence electrons of the sample. The advantage of SEM is that it allows for the analysis of thick samples that do not transmit electrons, but the resolution is much lower than for TEM.

2.5 Powder X-ray Diffraction

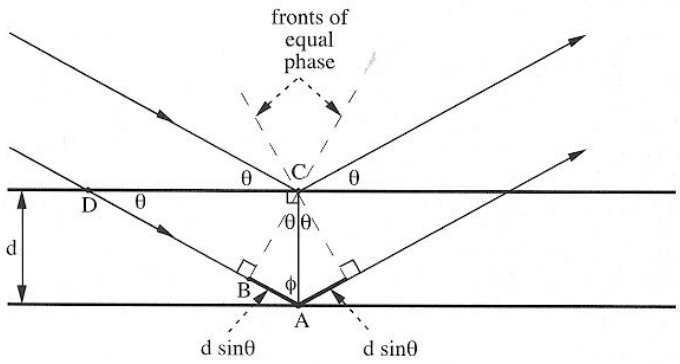

Figure 2.9. Requirement for satisfying the Bragg conditions for diffraction.

X-ray diffraction (XRD) analysis is based on interference between X-ray waves scattered from multiple planes in a certain crystallographic orientation (Figure 2.9). Constructive interference, which gives rise to peaks in the diffractogram, arise when the path length of the top and bottom rays is equal to an integer number of wavelengths, λ:

$$2d\sin\theta = n\lambda \tag{2.7}$$

For a particular set of crystallographic planes in a cubic crystal with lattice parameter a_0 and Miller index (*hkl*), the angles at which diffraction peaks occur (except those not allowed by the structure factor of the crystal) are:

$$2\theta_{hkl} = 2\arcsin\left(\frac{\lambda\sqrt{h^2+k^2+l^2}}{2a_0}\right) \tag{2.8}$$

Lattice constants can be determined by XRD and can be useful in the determination of the structure and composition of bimetallic nanoparticles. For very small nanoparticles, the lattice constant increases slightly. If NPs are single crystalline, their size can be inferred from the broadening of the diffraction peaks. For an infinite crystal, diffraction intensity only occurs exactly at the Bragg angle, θ_B, but as the number

of crystallographic planes decreases, this constraint loosens and partial constructive interference gives rise to a broadening of the diffraction peaks. The full-width at half maximum (FWHM), $\Delta\theta$, for diffraction from N planes is given by:

$$\frac{\Delta\theta}{\theta_B} \simeq \frac{0.9}{N} \tag{2.9}$$

For nanoparticles, the diameter of the particle (or crystallite size if the particles are not single crystalline), d, is approximately given by:

$$d = \frac{0.89\lambda}{\Delta(2\theta)\cos\theta} \tag{2.10}$$

Nanoparticles of different shapes can give rise to changes in the relative intensity of different diffraction peaks (e.g. 111 vs. 100), but one must be careful with such an analysis, as particles can also preferentially orient on a substrate in a particular lattice direction, especially for magnetic NPs.

2.6 Small Angle X-ray Scattering

X-ray scattering at small angles (SAXS) is extremely useful for characterization of both mesoporous materials[18] and nanoparticles.[19] Because mesoporous materials such as SBA-15 have an ordered structure (SBA-15 has hexagonally packed pores) with lattice spacing on the order of a few nanometers, the resulting scattering vector, q, and thus the scattering angle, θ_B, is small and not accessible to conventional XRD equipment. For the analysis of nanoparticles in a surrounding medium, particle size, shape, and PSD can be determined by analyzing scattering at very small angles. Scattering at small angles results from a difference in electron density between the particles and the surrounding medium and the SAXS pattern therefore contains information about the radius of gyration, which is the root mean square distance of all of the electrons from their center of

gravity.[20] Porod's Law relates the scattering intensity to the interfacial area for a colloidal system:

$$I(q) = 2\pi I_e \rho^2 S q^{-4} \tag{2.11}$$

S is the interfacial area between the colloids and surrounding medium and can thus be used to determine particle size. I_e is a constant, ρ the electron density difference between colloid particle and surrounding medium, and q is the scattering vector,

$$q = \frac{4\pi \sin\theta}{\lambda} \tag{2.12}$$

2.7 Physisorption: Surface Area and Pore Size Determination

Physisorption and chemisorption measurements involve isothermal adsorption of gases onto a surface. Physisorption is characterized by weak Van der Waals forces between adsorbate and substrate (< 10 kcal/mol) and is reversible and non-activated (i.e. there is no activation energy for adsorption). Adsorption is non-specific and multilayers form following monolayer coverage. The basic model for adsorption is the Langmuir model. The most basic derivation of this model requires many assumptions such as a planar surface, monolayer coverage, non-activated adsorption, and no adsorbate-adsorbate interactions, but has been extended to much less demanding assumptions. When treating this model, one starts by considering the system to be at equilibrium between surface sites (*S*), adsorbate molecules (*A*), and molecules adsorbed to a surface site (*SA*) with equilibrium constant:

$$K = \frac{[SA]}{[S][A]} = \frac{\theta}{p(1-\theta)} \tag{2.13}$$

In Equation 2.13, p is the external pressure and θ is the fractional coverage of the surface. A statistical mechanical treatment of this system results in a simple relationship between pressure and coverage:

$$\frac{p}{p_0} = \frac{\theta}{(1-\theta)q_i} \tag{2.14}$$

where p_0 is the pressure at which the chemical potential of the adsorbate molecules in the gas phase is zero (i.e. ambient pressure) and q_i is the partition function of the gas.

The Brunauer-Emmet-Teller (BET) method[21] is the most commonly used procedure for determining the surface area of materials. The BET equation (Equation 2.15) is derived by modifying the Langmuir model to allow for multilayer adsorption and setting the heat of adsorption of the layers after the first to be equal to the heat of liquefaction of the adsorbate.

$$\frac{p/p_0}{V\left(1-p/p_0\right)} = \frac{1}{V_m c} + \frac{c-1}{V_m c}\left(p/p_0\right) \tag{2.15}$$

A linear plot of $\frac{p/p_0}{V\left(1-p/p_0\right)}$ versus p/p_0 over the pressure range at which at which the BET assumptions hold (usually p/p_0 = 0.05 to 0.35) , one can obtain the monolayer volume, V_m, which directly corresponds to the surface area after accounting for the volume of the adsorbate. The BET constant, c, is related to the heat of adsorption of the first layer and thus the strength of adsorbate-adsorbate interactions.

Physisorption can also be used to determine the volume, pore size distribution, and shape of the pores of materials (either intraparticle or interparticle porosity). The

nomenclature used for classifying the size of pores is somewhat misleading: pores larger than 50 nm in diameter are termed "macropores," while those less than 2 nm are "micropores." Pores of intermediate size are called "mesopores." Isotherms obtained over the pressure range $p/p_0 = 0$ to ~0.99 are classified according to the Brunauer-Deming-Deming-Teller (DMMT) classification system[22] (Figure 2.10) and each isotherm is indicative of certain types of pores. Type IV isotherms arise from mesoporous solids with cylindrical pores including SBA-15. Many techniques exist for calculated the pore volume and pore size distribution of micropores and mesopores from such isotherms. For mesopores, the most common method is the BJH (Barrett-Joyner-Halenda) method, which is based on the Kelvin equation.[23]

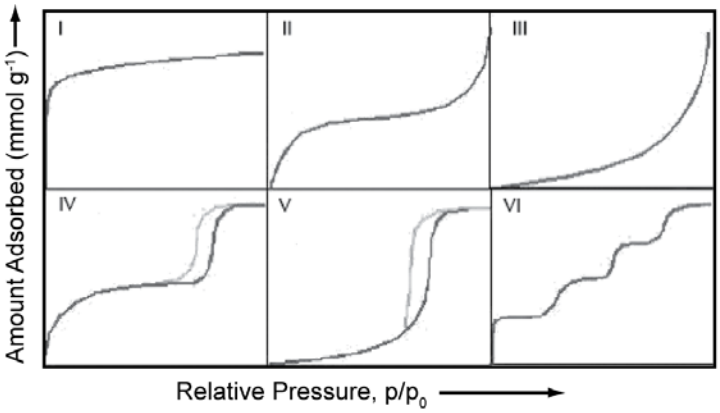

Figure 2.10. Isotherm classifications according to structure.

2.8 Chemisorption: Active Metal Surface Area Determination

Chemisorption, or selective gas adsorption, involves strong (> 20 kcal/mol), irreversible binding of adsorbate molecules to a substrate. Chemisorption is typically an activated process wherein a small barrier exists between the physisorbed state and the chemisorbed state. Because adsorption is specific (only occurs on surfaces that can form strong bonds with the adsorbate), it is used to determine the active surface area of metal

catalysts. Gases such as O_2, H_2, or CO selectively adsorb to metal surfaces but not to an inert support such as SiO_2. In a typical chemisorption experiment, a supported catalyst is activated, typically with a high temperature H_2 reduction then evacuated. An isotherm is recorded (typically near room temperature) by dosing in gas in steps. To account for any non-specific adsorption, the sample is re-evacuated and the isotherm is recorded a second time. By subtracting these isotherms and extrapolating to P = 0, a monolayer chemisorbed volume is obtained. If the stoichiometry is known (e.g. H_2 adsorbs dissociatively on Pt and one H_2 molecule titrates two Pt sites), the total number of active surface sites can be calculated.

2.9 Diffuse Reflectance Infrared Fourier Transform Spectroscopy

Infrared spectroscopy of powders and rough surfaces typically results in weak signals due to scattering of the incident infrared beam. In diffuse reflectance infrared Fourier transform spectroscopy (DRIFTS), this limitation is overcome with the use of a spherical mirror (Figure 2.11) that focuses the scattered light onto the detector. For powder catalysts, this means that infrared spectroscopy can be performed without preparing pellets with KBr to from a window for transmission Fourier transform infrared

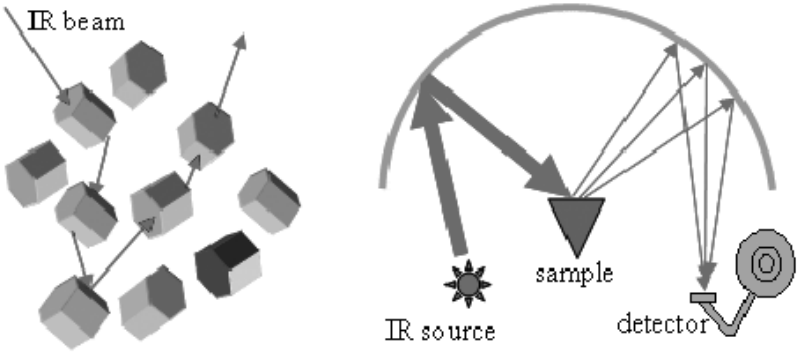

Figure 2.11. Concept and setup for DRIFTS.

spectroscopy (FTIR). This has the advantage of both limiting sample preparation and avoiding destruction of the sample by use of high pressures and the introduction of an added material.

A common characterization method for metal catalysts is infrared spectroscopy of CO adsorbed on the surface. CO adsorbs strongly on many transition metals and the strength of the C-O bond (directly probed by IR spectroscopy) is sensitive to coordination, oxidation state, and d-band structure of the metal where it is adsorbed. Blyholder developed a framework for understanding the stretching frequency of chemisorbed CO on transition metal surfaces based on Hückel molecular orbital theory.[24] For CO, there is a lone pair of electrons in the O 2s orbital and in a C sp_z-hybridized orbital, which form a σ bond with a surface metal atom and place a large formal negative charge onto the metal. Because of this negative charge, it is usually stated that there is backbonding of electrons into a π^* antibonding orbital of CO. Blyholder clarifies this statement: three π molecular orbitals are formed from a d-orbital of the metal, a p-orbital from C and a p-orbital from O. The lowest energy π -molecular orbital (MO) formed has no nodes and thus adds to the strength of the C-O and C-M bonds (M = metal). The second π -MO, which is lower in energy than the metal d-orbital, has a node between C and O and is partially filled. Thus, a metal atom that has more d-orbital electron density available for bonding with chemisorbed CO will donate these electrons into the partially filled π-MO and weaken the C-O bond, causing a red-shift in the IR frequency. For example, edge and corner atoms of nanoparticles are coordinated to fewer metal atoms and therefore have more d-orbital electron density for donation into the second π-MO.

2.10 Thermogravimetric/Differential Thermal Analysis

In a combined thermogravimetric/differential thermal analysis (TG/DTA) instrument, the mass and temperature of a sample (5 – 20 mg) and an inert reference are measured while applying a temperature program (typically heating at a set rate) in a controlled atmosphere. The mass change as a function of temperature can provide information on the composition of a sample. For the metal/SBA-15 catalysts, TGA provides information on how much adsorbed water, volatile organics, and organic surfactant is present in the as-synthesized materials. The DTA provides information on the exothermicity/endothermicity of each weight loss event.

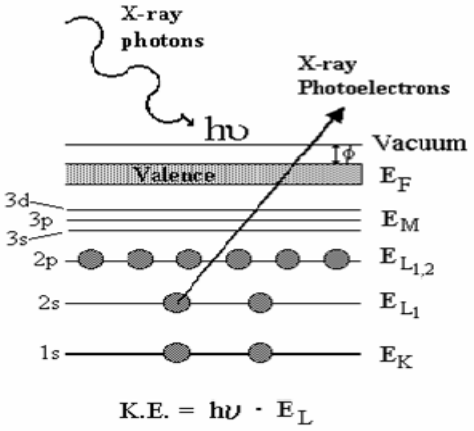

Figure 2.12. Core level X-ray photoelectron spectroscopy.

2.11 X-ray Photoelectron Spectroscopy

X-ray based spectroscopy includes X-ray absorbance (XAS), X-ray fluorescence (XAF), and X-ray photoelectron spectroscopy (XPS), among other more specialized techniques. These methods have been greatly enhanced in capability with the development of synchrotron facilities. The main components of a conventional XPS spectrometer are an X-ray source (typically an Mg or Al anode), a sample holder, and an electron detector (cylindrical mirror analyzer (CMA) or hemispherical analyzer) housed

in an ultrahigh vacuum chamber. The sample is irradiated with X-rays (Mg K_α = 1253.6 eV, Al K_α = 1486.6 eV), which results in the ejection of photoelectrons (Figure 2.12), secondary electrons, and Auger electrons, along with X-ray fluorescence and scattering. Photoelectrons can be generated from either core levels or valence levels, although core level photoelectrons are the more commonly investigated for chemical analysis because they have a much higher photionization cross section. The binding energy (BE) of emitted electrons is indicative of the element and chemical state of the atom they are ejected from and can be calculated by:

$$KE = h\nu - BE - \phi_s \tag{2.16}$$

where hν is the photon energy of the incident X-rays, KE is the kinetic energy of the detected photoelectron, and ϕ_s is the work function of the spectrometer. XPS is inherently surface sensitive because, while the penetration depth of the incident photoelectrons is a few microns, the mean free path of the emitted electrons is only a few to tens of angstroms.

Quantitative analysis from XPS is accomplished by comparing the area of peaks of different elements in an XPS spectrum. The number of detected electrons per second from a specific spectral peak depends on the number of atoms of that type (*n*), the photoelectric cross section (σ), the X-ray flux, the efficiency of the detector, the mean free path of electrons in the material, the angle between the sample and detector, and the area of the sample and instrument aperture. All of these factors should change equally for all elements from sample to sample and system to system except for *n* and σ. Thus, with the use of standard, atomic sensitivity factors can be determined for all of the

spectral lines of every element at different photon energies and have been tabulated.[25] The relative concentration of two elements in a sample is given simply by:

$$\frac{n_1}{n_2} = \frac{I_1 / S_1}{I_2 / S_2} \tag{2.17}$$

where I_i and S_i are the area and sensitivity factors for a given spectral line of element i.

2.12 High Pressure X-ray Photoelectron Spectroscopy

The development of synchrotron-based X-ray sources has led to significant advances in the techniques and resolution that are now possible. Synchrotron X-rays are much more intense and have a wide energy range. With a monochromater and X-ray optics, the X-ray energy can be tuned and focused to a small spot size. These advances have led to XPS with resolution < 0.1 eV and much shorter acquisition times. These capabilities allowed for the development of ambient pressure XPS (APXPS), now available at the Advance Light Source at Lawrence Berkeley National Lab and also at BESSY in Germany.[26-28] APXPS takes advantage of the fact that the mean free path of electrons in a few mTorr of gas is on the order of millimeters. Thus, by moving the aperture for electron detection close to the sample and combining differential pumping with electrostatic lenses (Figure 2.13), one can obtain XPS spectra at gas-solid interfaces.

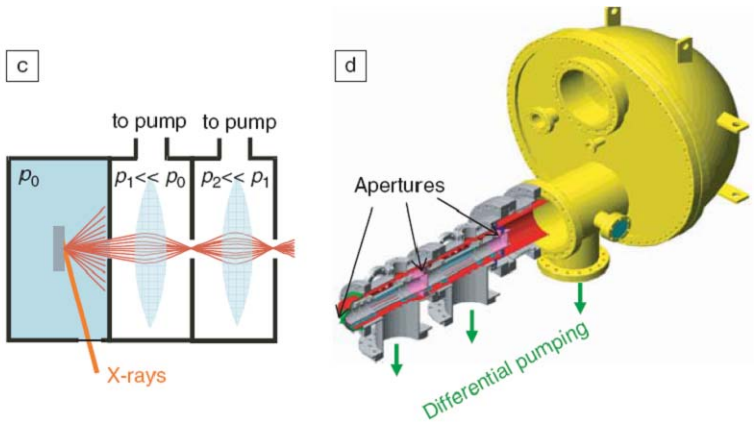

Figure 2.13. Schematic of electron collection for APXPS.

2.13 References

(1) Faraday, M. *Philosophical Transactions of the Royal Society of London* **1857**, *147*, 145.

(2) Hirai, H.; Nakao, Y.; Toshima, N. *Journal of Macromolecular Science, Part A* **1978**, *12*, 1117

(3) Hirai, H.; Nakao, Y.; Toshima, N. *Journal of Macromolecular Science-Chemistry* **1979**, *A13*, 727.

(4) Humphrey, S. M.; Grass, M. E.; Habas, S. E.; Niesz, K.; Somorjai, G. A.; Tilley, T. D. *Nano Lett.* **2007**, *7*, 785.

(5) Aiken, J. D.; Finke, R. G. *J. Mol. Catal. A: Chem.* **1999**, *145*, 1.

(6) Wilcoxon, J. P.; Abrams, B. L. *Chemical Society Reviews* **2006**, *35*, 1162.

(7) Beck, J. S.; Vartuli, J. C.; Roth, W. J.; Leonowicz, M. E.; Kresge, C. T.; Schmitt, K. D.; Chu, C. T. W.; Olson, D. H.; Sheppard, E. W.; McCullen, S. B.; Higgins, J. B.; Schlenker, J. L. *J. Am. Chem. Soc.* **1992**, *114*, 10834.

(8) Zhao, D.; Feng, J.; Huo, Q.; Melosh, N.; Fredrickson, G. H.; Chmelka, B. F.; Stucky, G. D. *Science* **1998**, *279*, 548.

(9) Zhao, D. Y.; Huo, Q. S.; Feng, J. L.; Chmelka, B. F.; Stucky, G. D. *J. Am. Chem. Soc.* **1998**, *120*, 6024.

(10) Kruk, M.; Jaroniec, M.; Ko, C. H.; Ryoo, R. *Chem. Mater.* **2000**, *12*, 1961.

(11) Rioux, R. M.; Song, H.; Hoefelmeyer, J. D.; Yang, P.; Somorjai, G. A. *J. Phys. Chem. B* **2005**, *109*, 2192.

(12) Bagshaw, S. A.; Prouzet, E.; Pinnavaia, T. J. *Science* **1995**, *269*, 1242.

(13) Song, H.; Rioux, R. M.; Hoefelmeyer, J. D.; Komor, R.; Niesz, K.; Grass, M.; Yang, P. D.; Somorjai, G. A. *J. Am. Chem. Soc.* **2006**, *128*, 3027.

(14) Gaines, G. L. *Thin Solid Films* **1983**, *99*, 243.

(15) Song, H.; Kim, F.; Connor, S.; Somorjai, G. A.; Yang, P. D. *J. Phys. Chem. B* **2005**, *109*, 188.

(16) Fogler, H. S. *Elements of Chemical Reaction Engineering*, 2nd ed.; Prentice-Hall, Inc.: Englewood Cliffs, 1992.

(17) Fultz, B.; Howe, J. M. *Transmission Electron Microscopy and Diffractometry of Materials*, 2nd ed.; Springer: New York, 2002.

(18) Edler, K. J.; Dougherty, J.; Durand, R.; Iton, L.; Kirton, G.; Lockhart, G.; Wang, Z.; Withers, R.; White, J. W. *Colloids Surf., A* **1995**, *102*, 213.

(19) Neilson, G. F. *J. Appl. Crystallog.* **1973**, *6*, 386.

(20) Glatter, O.; Kratsky, O. *Small Angle X-ray Scattering*; Academic Press: New York, 1982.

(21) Brunauer, S.; Emmett, P. H.; Teller, E. *J. Am. Chem. Soc.* **1938**, *60*, 309.

(22) Brunauer, S.; Deming, L. S.; Deming, W. E.; Teller, E. *J. Am. Chem. Soc.* **1940**, *62*, 1723.

(23) Barrett, E. P.; Joyner, L. G.; Halenda, P. P. *J. Am. Chem. Soc.* **1951**, *73*, 373.

(24) Blyholder, G. *J. Phys. Chem.* **1964**, *68*, 2772.

(25) Wagner, C. D.; Riggs, W. M.; Davis, L. E.; Moulder, J. F.; Mouilenberg, G. E. *Handbook of X-Ray Photoelectron Spectroscopy*; Perkin-Elmer: Eden Prarie, MN, 1979.

(26) Bluhm, H.; Andersson, K.; Araki, T.; Benzerara, K.; Brown, G. E.; Dynes, J. J.; Ghosal, S.; Gilles, M. K.; Hansen, H. C.; Hemminger, J. C.; Hitchcock, A. P.; Ketteler, G.; Kilcoyne, A. L. D.; Kneedler, E.; Lawrence, J. R.; Leppard, G. G.; Majzlam, J.; Mun, B. S.; Myneni, S. C. B.; Nilsson, A.; Ogasawara, H.; Ogletree, D. F.; Pecher, K.; Salmeron, M.; Shuh, D. K.; Tonner, B.; Tyliszczak, T.; Warwick, T.; Yoon, T. H. *J. Electron. Spectrosc. Relat. Phenom.* **2006**, *150*, 86.

(27) Bluhm, H.; Havecker, M.; Knop-Gericke, A.; Kiskinova, M.; Schlogl, R.; Salmeron, M. *MRS Bull.* **2007**, *32*, 1022.

(28) Ogletree, D. F.; Bluhm, H.; Lebedev, G.; Fadley, C. S.; Hussain, Z.; Salmeron, M. *Rev. Sci. Instrum.* **2002**, *73*, 3872.

Chapter 3: Size dependence of gas phase crotonaldehyde hydrogenation by Pt nanoparticles supported on SBA-15

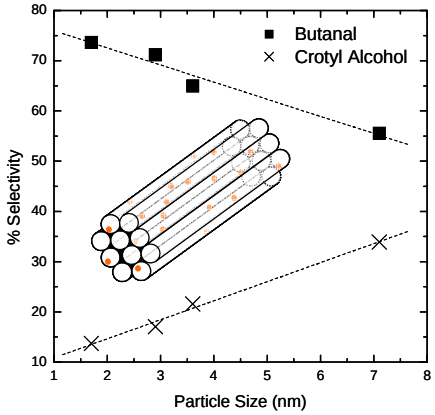

The activity and selectivity for the selective hydrogenation of crotonaldehyde to crotyl alcohol and butyraldehyde was studied over a series of Pt nanoparticles (diameter of 1.7, 2.9, 3.6, and 7.1 nm) synthesized alcohol reduction of a Pt salt in the presence of poly(vinylpyrrolidone) which were supported on mesoporous silica SBA-15. The rate of crotonaldehyde hydrogenation and selectivity towards crotyl alcohol both increase with increasing particle size while the apparent activation energy remains constant with particle size. The turnover frequency increases from 2.1×10^{-2} s^{-1} to 4.8×10^{-2} s^{-1} as the particle size increases from 1.7 nm to 7.1 nm at 353 K, 8 Torr crotonaldehyde, and 160 Torr H_2; the selectivity towards crotyl alcohol increases from 13.7% to 33.9%. The apparent activation energy is between 10.8 and 11.7 kcal/mol for all catalysts. Reduction temperature of 673 – 723 K resulted in increased activity and selectivity relative to reduction at either higher or lower temperature. Sintering of Pt particles due to reduction at high temperatures is discounted and we propose that the dependence of turnover frequency and selectivity on reduction temperature is due to changes in the carbon overlayer from PVP decomposition.

3.1. Introduction

Polymer and surfactant stabilized transition metal nanoparticles (NPs) have been utilized as both homogeneous and heterogeneous catalysts over the past decade.[1] Their catalytic ability has been studied extensively as both as colloidal suspensions[2] and as oxide or carbon supported NPs.[3, 4] Because this polymer mediated method of catalyst preparation can yield transition metal NPs with a much smaller particle size distribution than in traditionally synthesized transition metal catalysts, they have the potential as model systems for the elucidation of particle size effects in catalysis. However, a complication due to the use of catalysts prepared from NPs stabilized with polymers or other organic molecules is the role of the adsorbed organic molecule in affecting catalytic function. In solution, the type of protecting molecule can dramatically change the stability and activity of metal NPs for hydrogenation reactions.[5, 6] For the investigation of gas phase heterogeneous catalysis using stabilized NPs on oxide supports, it has generally been considered necessary to remove the organic molecules by thermal treatment.[7-9]

In our previous work, we developed two strategies for supporting PVP-protected Pt nanoparticles on mesoporous SBA-15 silica and studied the particle size dependence of the single product reactions, ethylene hydrogenation and ethane hydrogenolysis, and the influence of particle size on the poisoning of ethylene hydrogenation by carbon monoxide.[8, 10-13] In this paper, we report the use of Pt(X)/SBA-15 (X = 1.7, 2.9, 3.6, and 7.1 nm) catalysts prepared by the nanoparticle encapsulation (NE)[10] method for the selective hydrogenation of crotonaldehyde to crotyl alcohol and butyraldehyde (butanal). We examined the effect of particle size for both the rate of overall hydrogenation of

crotonaldehyde and the selectivity towards the industrially desired product, crotyl alcohol. We demonstrate NE-synthesized catalysts have similar catalytic activity and selectivity for crotonaldehyde hydrogenation as conventionally-prepared catalysts.[14] We studied the effect of reduction pretreatment to understand how residual PVP affects catalytic activity and selectivity.

The hydrogenation of crotonaldehyde, and other α,β-unsaturated aldehydes is of fundamental scientific interest because two different types of unsaturated chemical bonds (C=C and C=O) are present in the same molecule, serving as a useful probe of heterogeneous chemoselectivity. Gallezot and Richard summarized many of the properties that determine catalytic activity and selectivity for the conversion of α,β-unsaturated aldehydes by heterogeneous catalysis.[14] Factors that influence both activity and selectivity, such as the type of metal, the exposed crystal face, steric hindrance of the C=C bond from bulky groups such as phenyl (cinnamaldehyde) or methyl (crotonaldehyde, 3-methyl-crotonaldehyde), ligands that modify the metal surface, catalyst supports that exhibit strong metal support interactions (SMSI), and promoters such as K, Fe, and Sn which modify (electronically and/or geometrically) the metal surface have been investigated.[14]

For studies examining the effect of particle size, the overall TOF as well as selectivity towards crotyl alcohol generally increase with increasing particle size.[15-18] The role of particle size appears to be three-fold. The first is related to the fraction of close-packed sites resembling (111) faces versus coordinatively unsaturated sites resembling more open faces such as (100) or (110). Crotonaldehyde preferentially adsorbs via a di-σ bond of C=O on the (111) surface of Pt, through a π bond of C=C on

the (110) surface, and lies flat in an η^4 configuration with π bonds through both C=C and C=O on Pt(100).[19] The increase in selective C=O interaction on (111) faces is considered to be the cause of increased selectivity towards the unsaturated aldehyde over close packed surfaces. Because large particles have larger close packed terraces of a close packed surface like (111) than smaller particles, larger particles are more selective for the formation of crotyl alcohol, which involves preferential hydrogenation of C=O.[18] On gold NPs, however, it has been demonstrated that edge and corner atoms are more selective than terrace sites for the formation of allyl alcohol in the hydrogenation of acrolein.[20] The second reason for the structure sensitivity of the reaction is that decarbonylation of crotonaldehyde to CO and hydrocarbons occurs preferentially on the corner and edge sites that are more prevalent on smaller particles.[21] A third factor influencing selectivity is the steric hindrance of the C=C bond of α,β-unsaturated aldehydes such as cinnamaldehyde and to a lesser extent, 3-methyl-crotonaldehyde and crotonaldehyde. These side groups can sterically hinder the unsaturated aldehyde from adsorbing through the C=C moiety, increasing selectivity towards the unsaturated alcohol. This effect is enhanced on larger particles where flat planes can not accommodate these bulky side groups as well as smaller particles, thus shifting selectivity towards the unsaturated alcohol with increasing particle size. A notable exception to this rule appears to be gold supported on TiO_2 for the selective hydrogenation of crotonaldehyde to crotyl alcohol.[22]

3.2. Experimental

3.2.1 Synthesis of Pt Nanoparticles

Dihydrogen hexachloroplatinate ($H_2PtCl_6 \cdot 6H_2O$, 99.9%, metals basis) was purchased from Alfa Aesar. Poly(vinylpyrrolidone) (PVP, M_w = 29,000 and 55,000) was obtained from Sigma-Aldrich. Methanol, ethanol, and ethylene glycol were of analytical grade and used without further purification.

Pt particles were synthesized according to literature methods.[8, 23, 24] 1.7 nm Pt particles were made by adding NaOH solution (12.5 mL, 0.5 M) in ethylene glycol to a solution of $H_2PtCl_6 \cdot 6H_2O$ (250 mg) in 12.5 mL of ethylene glycol. The mixture was heated at 433 K for 3 h with N_2 bubbling. After reaction, particles were precipitated by adding 1 mL of 2 M HCl per 4 mL of Pt sol, and dispersed in ethanol containing 12.2 mg of PVP (M_w = 29,000). 2.9 nm Pt particles were synthesized by heating a mixture of PVP (26.6 mg) and $H_2PtCl_6 \cdot 6H_2O$ (124.3 mg) in water (40 mL)/methanol (360 mL) solution for 3 h at reflux. After the solution cooled, rotary evaporation was used to remove the solvent and the particles were then dispersed in ethanol. 3.6 nm Pt particles were formed by mixing the 2.9 nm Pt colloidal solution (100 mL) in a water/methanol (1:9) mixture with 10 mL of 6.0 mM $H_2PtCl_6 \cdot 6H_2O$ aqueous solution and 90 mL of methanol. The mixture was heated for 3 h at reflux and purified in the same way as the 2.9 nm Pt particles. 7.1 nm Pt particles were synthesized by adding a total 3 mL of 0.375 M PVP (M_w = 55,000) and 1.5 mL of 0.0625 M $H_2PtCl_6 \cdot 6H_2O$ solutions to 2.5 mL refluxing ethylene glycol in aliquots every 30 s for 16 min. The mixture was refluxed for an additional 5 min, and then quenched by rapid cooling. The resulting Pt particles were precipitated from solution using an excess of acetone and then centrifuged at 5000 rpm and redispersed in ethanol.

All Pt colloidal solutions were then purified by sequential precipitation/redispersion with hexanes (precipitation) and ethanol (redispersion), and eventually dispersed in an appropriate amount of deionized water necessary for a 3×10^{-3} M solution based on Pt salt concentration. The particle sizes were measured by transmission electron microscopy (TEM, Philips/FEI Tecnai 12 microscope operated at 100 kV) and X-ray diffraction (XRD, Bruker D8 GADDS diffractometer with Co K_α radiation (λ = 1.79 Å)). Estimated particle sizes were 1.73±0.26 (1.7), 2.80±0.21 (2.9), 3.39±0.26 (3.6), and 7.16±0.37 (7.1) nm by TEM (XRD) respectively, indicating high uniformity and monodispersity of each particle less than $\sigma \sim 8\%$

3.2.2 Synthesis of Pt Nanoparticle Catalysts

Preparation of the Pt nanoparticles (NPs) used in this study and their anchoring in mesoporous silica SBA-15 by nanoparticle encapsulation (NE) has been reported previously.[8, 10] For this study, a series of Pt(*X*)/SBA (*X* = 1.7 – 7.1 nm) were synthesized with nominal loadings of 1 – 3%. A higher loading was used for the larger NPs to account for the decrease in surface area of larger NPs.

The nanoparticles were incorporated into SBA-15 by synthesizing the mesoporous oxide in neutral conditions in the presence of the NPs.[10] The catalysts were then washed in ethanol, dried in air at 100 °C and then calcined in flowing O_2 at 450 °C for 12 h (Pt(2.9 nm)/SBA-15 and Pt(3.6 nm)/SBA-15), at 350 °C for 12 h (Pt(1.7 nm)/SBA-15), or at 450 °C for 24 h (Pt(7.1 nm)/SBA-15). The catalysts were characterized by XRD, TEM, chemisorption and physisorption (Quatachrome Autosorb 1), and inductively coupled plasma – optical emission spectroscopy (ICP-OES, Galbraith

Laboratories). For chemisorption, samples were reduced at 400 °C for 2 h, then evacuated at 350 °C for 1 h prior to analysis

3.2.3 Catalytic Studies

Catalytic reactions were carried out in a stainless steel (⅛") reactor system equipped with mass flow controllers (MKS Instruments) for He, H_2, and O_2 (UHP, Praxair, used as-received) and an inline saturator composed of Pyrex for the introduction of crotonaldehyde (Sigma-Aldrich, 99.9%, predominately *trans*). The catalyst was reduced *in situ* at the desired temperature (typically 673 K) for 2 h with a H_2 (160 Torr)/He mixture which bypassed the saturator and into the reactor. The reaction was initiated by introducing a flow of a H_2/He mixture (70 ml min^{-1}) through the saturator containing crotonaldehyde held at 273 K. The inlet conditions prior to contact with the catalyst bed was 8 Torr crotonaldehyde, 160 Torr H_2 and balance He.

The catalyst was placed on top of a quartz frit in a ¼" O. D. Pyrex U-tube reactor. For a typical experiment, ~ 15 mg catalyst was diluted with ~ 50 mg acid-washed and calcined low surface area quartz (Sigma Aldrich) and loaded into the reactor between beds of the same acid-washed and calcined quartz. The effluent stream was analyzed every 9 min. by gas chromatography (HP 5890 Series II) using a flame ionization detector (FID) for analysis of organics and a thermal conductivity detector (TCD) for H_2 detection. The reaction was started at 353 K until a stable activity was measured (i.e. until initial deactivation was almost complete and a steady-state activity was reached). For most catalyst samples, this took ~ 2.5 h. The reaction temperature was then changed (and left for 1.5 h before changing temperature) to 373, 393, 383, 373, 363, and finally back to 353 K. Unless stated otherwise, data reported in this paper is the steady-state rate

at the final 353 K temperature. The activation energy for all samples was determined using the rates obtained while cooling from 393 to 353 K, averaging the rate calculated from ten GC injections at each temperature.

3.3. Results and Discussion

3.3.1 Catalyst Properties

Table 3.1: Physiochemical properties and summary of catalytic results for Pt(*X*)/SBA-15 catalysts

Catalyst	Pt Loading[a] (% Pt)	TEM Size (nm)	H/Pt[b]	TOF ($100 \times s^{-1}$)[c]	$S_{crotyl\ alcohol}$[d]	E_a (kcal mol^{-1})[e]
Pt(1.7 nm)/SBA-15	0.58	1.7	0.33	2.1	13.7	10.8
Pt(2.9 nm)/SBA-15	1.28	2.9	0.18	2.9	17.0	11.2
Pt(3.6 nm)/SBA-15	1.61	3.6	0.15	4.3	21.6	10.8
Pt(7.1 nm)/SBA-15	2.43	7.1	0.08	4.8	33.9	11.7

[a] Loading determined by ICP-OES.
[b] Irreversible H_2 chemisorption at 303 K, extrapolated to P = 0.
[c] Overall crotonaldehyde hydrogenation rate per surface site at 8 Torr C_6H_4O, 160 Torr H_2 and 353 K.
[d] Determined at 8 Torr crotonaldehyde, and 160 Torr H_2 and 353 K.
[e] Determined at 8 Torr crotonaldehyde, 160 Torr H_2, and 353 – 393 K.

The resulting SBA-15 and Pt(*X*)/SBA-15 catalysts (*X* = 1.7, 2.9, 3.6, and 7.1 nm) were characterized by elemental analysis, XRD, and SAXS. Catalysts were prepared with a nominal weight loading of 1-3%; actual metal loadings determined by elemental analysis were between 0.6 and 2.4 wt. % (Table 3.1). TEM characterization clearly indicates the presence of Pt nanoparticles supported within the mesoporous structure of SBA-15 (Figure 3.1). Three characteristic peaks for Pt appear in the XRD spectra (Figure 3.2) at 2θ = 45.9 °, 54.0°, and 80.1° corresponding to (111), (200), and (220) reflections of the Pt fcc lattice, respectively, as well as a broad amorphous SiO_2 signal at

$2\theta = 27.4°$. All three Pt peaks become sharper with an increase of the particle size from 1.7 to 7.1 nm. SAXS data (Figure 3.2) exhibit three peaks assignable to (100), (110), and (200) of the hexagonal mesostructure with the same *p6mm* symmetry as observed in pristine SBA-15.[25] The lattice spacing for d_{100} are almost constant (~11 nm) with variation in particle size, in contrast to previous results of Somorjai *et al.*,[25, 26] in which the lattice parameter of Au/SBA-15 increased with the incorporation of larger Au nanoparticles into the mesoporous structure.

Particle size measurements by TEM and XRD verified that particle size was not perturbed during the nanoparticle encapsulation synthesis. However, particle sizes obtained from these measurements are not a good measure of the catalytically relevant particle size. Selective adsorption of probe gases represents the most appropriate probe for determining Pt particle size and is used to normalize measured reaction rates to the exposed metal surface area.[27] Chemisorption is sensitive to the polymer presence on the nanoparticle surface and any changes in particle size during pretreatment. Dispersion, which is related to particle size, was measured by selective H_2 adsorption. Adsorption uptakes and dispersion are calculated assuming hemispherical particle geometry, which is listed in Table 3.1. The three independent techniques are in relatively good agreement and variance in particle size determined by the different adsorption techniques may be a consequence of changes in adsorbate stoichiometry with particle size or the influence of residual PVP on the nanoparticle surface.

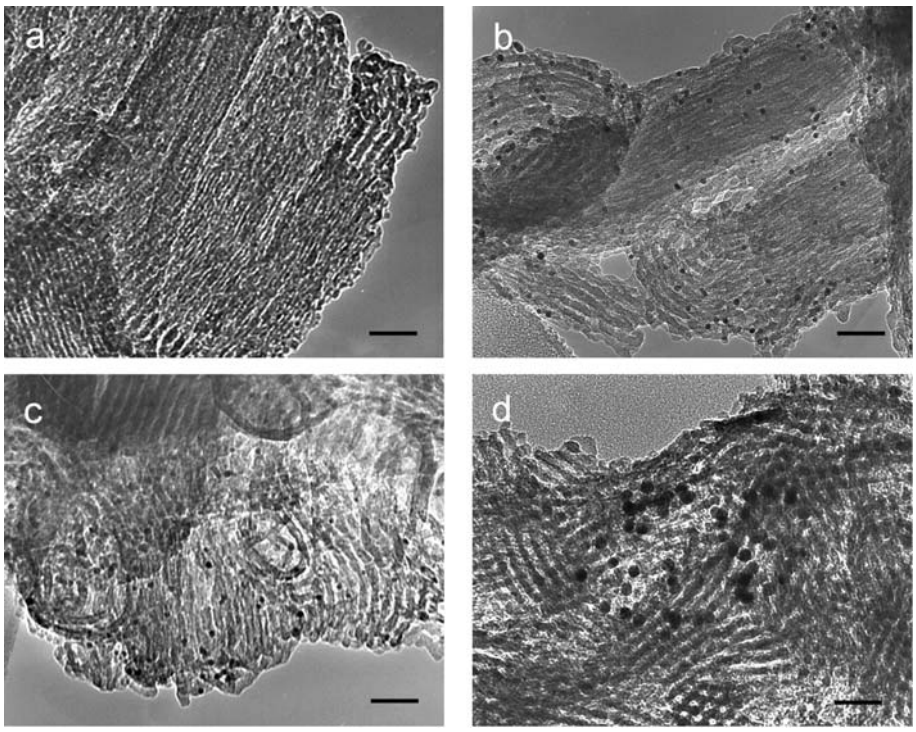

Figure 3.1: TEM images of calcined (a) Pt(1.7 nm)/SBA-15, (b) Pt(2.9 nm)/SBA-15, (c) Pt(3.6 nm)/SBA-15, and (d) Pt(7.1 nm)/SBA-15. Scale bars are 40 nm.

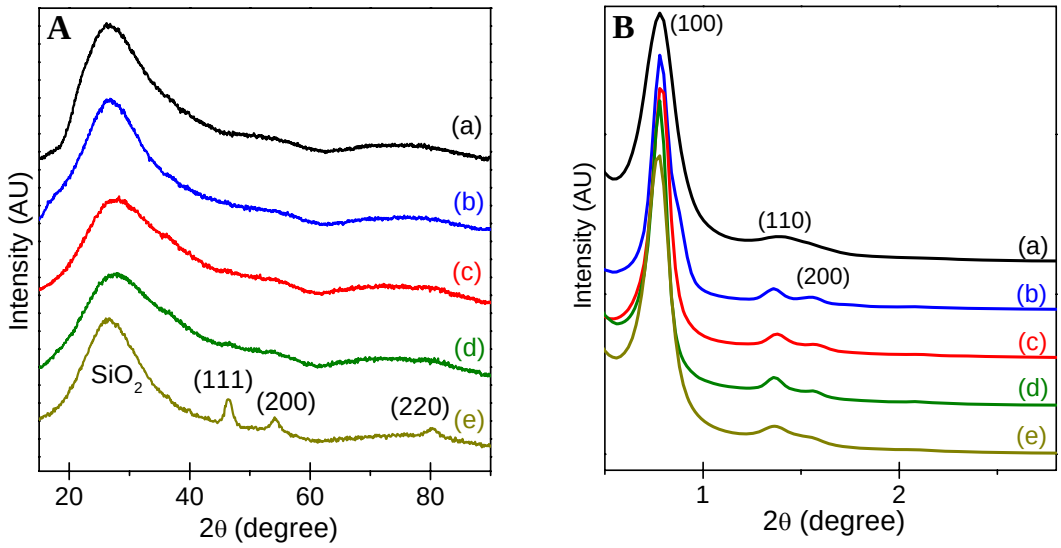

Figure 3.2: (A) Wide angle X-ray diffractograms and (B) small angle X-ray scattering for (a) SBA-15, (b) Pt(1.7 nm)/SBA-15, (c) Pt(2.9 nm)/SBA-15, (d) Pt(3.6 nm)/SBA-15, and (e) Pt(7.1 nm)/SBA-15.

3.3.2 General Trends for Crotonaldehyde Hydrogenation

The major product for crotonaldehyde hydrogenation for all catalysts and over the entire temperature range (353 – 393 K) is butryaldehyde, which forms by selective C=C hydrogenation. The minor products are crotyl alcohol (the second most abundant product) formed by selective C=O hydrogenation, butanol (complete hydrogenation of C=C and C=O), and propylene and propane (C_3 hydrocarbons) (decarbonylation).

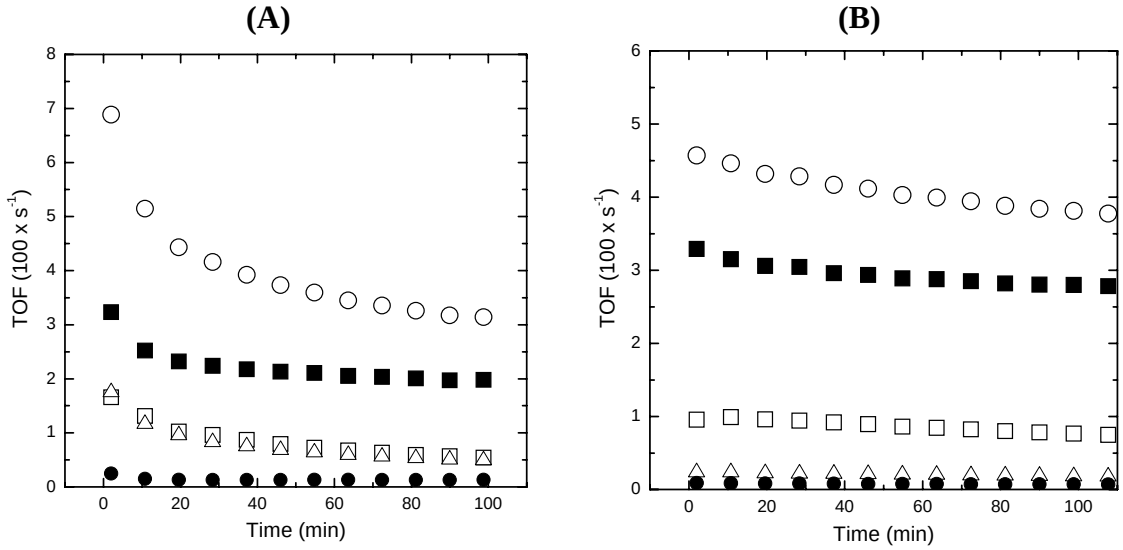

Figure 3.3. The initial deactivation of (A) Pt(1.7 nm)/SBA-15 and (B) Pt(7.1 nm)/SBA-15 with time-on-stream at 353 K. The initial total turnover frequency is greater for the 1.7 nm particles, but they demonstrate a greater degree of deactivation (presumably due to the greater rate of decarbonylation). The disappearance of crotonaldehyde (○) and formation of butyraldehyde (■), crotyl alcohol (□), butanol (Δ), and C_3 hydrocarbons (●) are shown. The pressure of crotonaldehyde and hydrogen was 8 Torr and 160 Torr, respectively (1 atm total pressure).

The initial time on stream data for Pt(1.7 nm)/SBA-15 and Pt(7.1 nm)/SBA-15 shown in Figure 3.3 demonstrate both samples undergo an initial deactivation that lasts about 2.5 h. It is well-documented in the literature that this deactivation is a result of decarbonylation and the subsequent adsorption of CO to the Pt surface, as well as carbon deposition resulting from C-C and C-H bond scission.[28] No CO was detected in the gas

phase but the C_3 hydrocarbons produced from the decarbonylation pathway were detected for all samples and at all temperatures. The initial TOF for decarbonylation is at least 1×10^{-3} s^{-1} for all four catalysts. Assuming all the CO that is formed during decarbonylation remains on surface (which appears to be a good assumption because we observe no CO in the gas-phase, enough CO forms to saturate Pt surface sites within 15-20 minutes of the onset of reaction. Gas phase CO must then be present under steady state reaction conditions, but we did not detect any. The absence of a measurable concentration of CO in the gas phase can be attributed to the lower sensitivity of TCD compared to FID, but should be equal to the amount of propene plus propane formed. The deactivation of heterogeneous catalysts for hydrogenation of α,β-unsaturated aldehydes by CO as a result of decarbonylation has been revealed in surface science studies,[29] by infrared spectroscopy on supported catalysts,[30] and through kinetic studies[31] over a number of metals and using different unsaturated aldehydes.

The temperature dependence for hydrogenation is similar for all catalysts studied. The overall apparent activation energy for the disappearance of crotonaldehyde is particle size independent (Table 3.1). The apparent activation energy for the individual products is not dependent on particle size: 16 – 17 kcal mol^{-1} for C=C hydrogenation to butyraldehyde, 7 – 10 kcal mol^{-1} for C=O hydrogenation to crotyl alcohol, 10 – 15 kcal mol^{-1} for the complete hydrogenation to butanol, and 11 – 12 kcal mol^{-1} for decarbonylation. The temperature dependence for all products on the Pt(1.7 nm)/SBA-15 and Pt(7.1 nm)/SBA-15 is represented in Figure 3.4. Lower temperatures favor the formation of minor products, particularly crotyl alcohol, relative to butyraldehyde. Butyraldehyde is the more thermodynamically-favored product, but it is also the more

kinetically-hindered (higher apparent activation energy). These observations are consistent with general trends of crotonaldehyde hydrogenation over Pt catalysts that have been reported previously.[14]

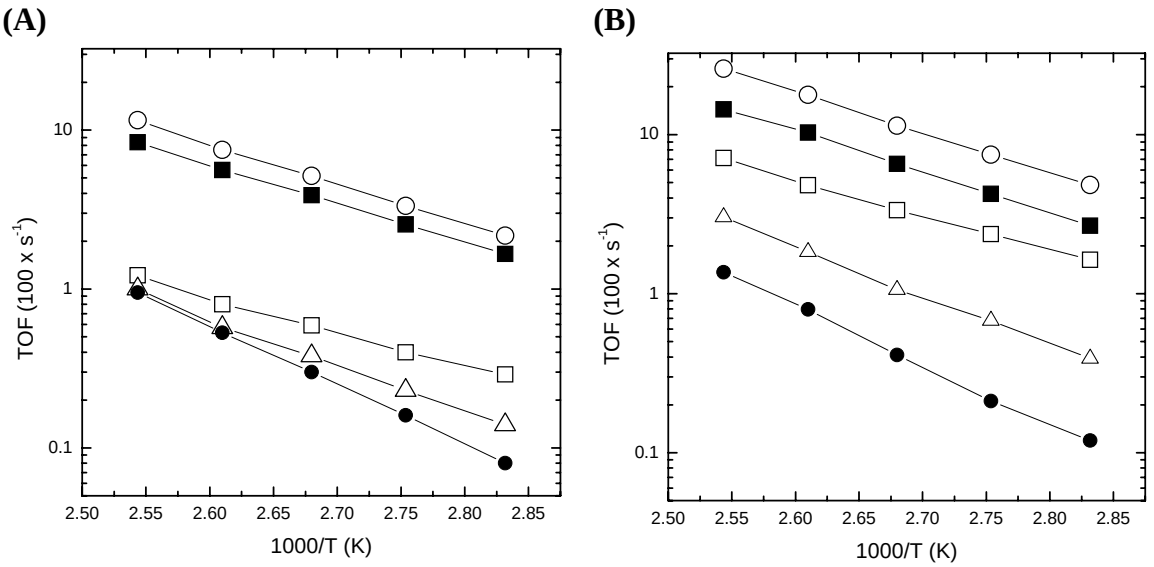

Figure 3.4. Turnover frequency for the disappearance of crotonaldehyde (○) and formation of butyraldehyde (■), crotyl alcohol (□), butanol (Δ), and C_3 hydrocarbons (●) as an Arrhenius plot for (A) Pt(1.7 nm)/SBA-15 and (B) Pt(7.1 nm)/SBA-15. The pressure of crotonaldehyde and hydrogen was 8 Torr and 160 Torr, respectively (1 atm total pressure).

3.3.3 Particle Size Effects on Activity and Selectivity for Crotonaldehyde Hydrogenation

The steady-state TOF and selectivity at 353 K to crotyl alcohol for all catalysts is listed in Table 3.1 and shown in Figures 3.5 and 3.6 for Pt(1.7 nm)/SBA-15 and Pt(7.1 nm)/SBA-15. The overall rate and selectivity to crotyl alcohol increased monotonically with increasing particle size. The steady state rate increased by a factor of 2 (from 2.1×10^{-2} s^{-1} to 4.8×10^{-2} s^{-1}) and the selectivity towards crotyl alcohol varied by a factor of almost 3 (from 13.7 % to 33.9 %) with an increase in particle size from 1.7 nm to 7.1 nm. The increase in selectivity toward crotyl alcohol with particle size has been well

documented.[14] The preferential bonding of C=O through a di-σ interaction on the extended, close packed (111) surface and of C=C through a π bond on the more corrugated Pt(110) surface has been determined both theoretically[19] and experimentally.[32] Additionally, the methyl group of crotonaldehyde sterically hinders adsorption through C=C bonding on the flatter surfaces exposed on larger NPs.

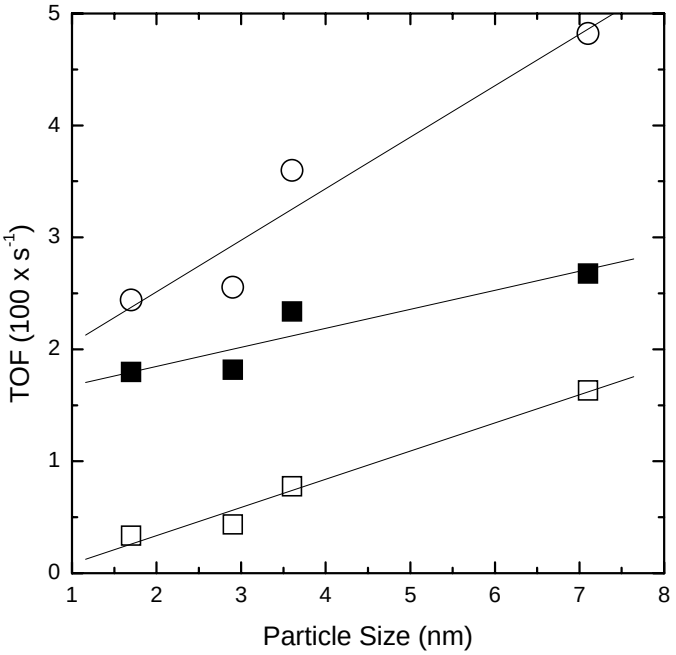

Figure 3.5: Turnover frequency as a function of particle size at 353 K for butyraldehyde (■) and crotyl alcohol (□). The overall TOF (○) increases with particle size, but more strongly for the formation of crotyl alcohol. The pressure of crotonaldehyde and hydrogen was 8 Torr and 160 Torr, respectively (1 atm total pressure).

The initial deactivation is also dependent on particle size. During the first few minutes on stream, Pt(1.7 nm)/SBA-15 is 1.5 times more active than Pt(7.1 nm)/SBA-15 (6.9×10^{-2} s^{-1} versus 4.7×10^{-2} s^{-1}). While both catalysts have the same TOF for butryaldehyde production, the Pt(1.7 nm)/SBA-15 is 1.5 times more active for the formation of crotyl alcohol, seven times more active for complete hydrogenation to butanol, and three times more active for decarbonylation at the onset of reaction (Figure

3.3). The three-fold higher specific activity for decarbonylation explains the larger extent of deactivation over Pt(1.7 nm)/SBA-15 compared to Pt(7.1 nm)/SBA-15. The initial TOF for decarbonylation over the four catalysts is 2.5×10^{-3}, 1.8×10^{-3}, 1.0×10^{-3}, and 1.0×10^{-3} s^{-1} for Pt(1.7 nm)/SBA-15 (3.3-fold decrease in activity from initial to steady state), Pt(2.9 nm)/SBA-15 (2.3 fold decrease), Pt(3.6 nm)/SBA-15 (1.8 fold decrease), and Pt(7.1 nm)/SBA-15 (1.8 fold decrease), respectively. The decarbonylation reaction poisons the catalyst by leaving adsorbed CO on the Pt surface, but the coverage of CO reaches some steady-state coverage because the catalysts are still active, which is not true when CO is intentionally added to the reaction stream during the hydrogenation of 3-methyl-crotonaldehyde over Ru/SiO_2.[30]

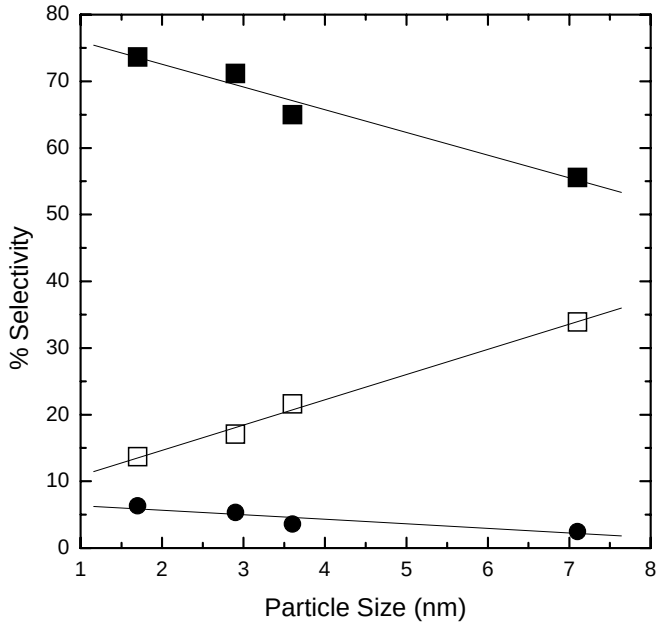

Figure 3.6: Selectivity as a function of particle size at 353 K for butyraldehyde (■), crotyl alcohol (□), and C_3 hydrocarbons (●). The selectivity towards crotyl alcohol increased with increasing particle size, while the butyraldehyde selectivity decreased. The pressure of crotonaldehyde and hydrogen was 8 Torr and 160 Torr, respectively (1 atm total pressure).

3.3.4 Effect of Reduction Temperature

The effect of reduction temperature was studied on both the Pt(1.7 nm)/SBA-15 and Pt(7.1 nm)/SBA-15 catalysts. All samples were calcined in O_2 at high temperature followed by reduction in H_2 (as described previously) in the reactor immediately prior to reactivity studies of crotonaldehyde hydrogenation. Both samples show an optimal reduction temperature of ~ 673 – 723 K with lower and higher reduction temperatures resulting in a lower overall conversion rate of crotonaldehyde as well as a lower selectivity towards crotyl alcohol (Figure 3.7). Particle sintering, which has been observed in many studies of Pt on SiO_2,[33] is ruled out as the cause of these changes based on TEM observations of the catalysts before and after high temperature reduction.

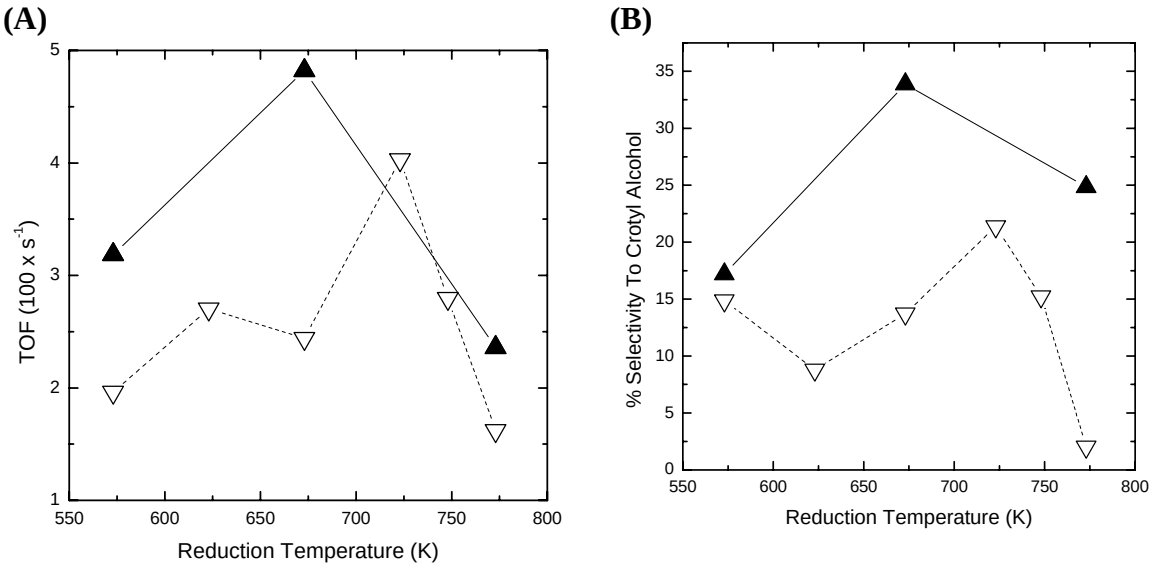

Figure 3.7. (A) Overall turnover frequency and (B) the selectivity to crotyl alcohol as a function of reduction temperature at 353 K for Pt(1.7)/SBA-15 (▽) and Pt(7.1)/SBA-15 (▲). The overall TOF is maximized when the catalysts are reduced at temperatures of 573 – 773 K. The pressure of crotonaldehyde and hydrogen was 8 Torr and 160 Torr, respectively (1 atm total pressure).

The catalytic selectivity and activity of supported Pt catalysts has been shown to be very dependent on reduction temperature for reducible supports, such as titania, niobia, and vanadia. This affect has been demonstrated to be the result of the formation of a partial overlay of the partially reduced support (e.g. TiO_x, $x < 2$) on the Pt metal.[34] This trend is not, however, observed for nonreducible supports such as SiO_2, Al_2O_3, or carbon.[33] The reduction temperature for Pt/SiO_2 apparently does not influence catalytic activity because of SMSI in the case of SiO_2. In the case of carbon, there also appears to be no MSI effect[33] unless the carbon support is initially oxidized.[35] In the case of Pt supported on carbon, pre-oxidizing the carbon by treating it with aqueous H_2O_2 followed by reduction at 623 K increased the selectivity towards crotyl alcohol by as much as 3-fold and also increased the TOF. Reduction at 723 or 773 K increased both selectivity and TOF to an even greater extent.

The fact that a strong dependence on particle size is observed for this series of Pt(*X*)/SBA-15 catalysts suggests that PVP is acting in a fashion similar to the oxidized carbon support studied by Coloma *et al.*[35] Some oxidized carbon likely remains on the Pt nanoparticle surface even after high temperature calcination. In a study of PVP capped Pt nanoparticles, after heating in N_2 at 773 K for 0.5 h, 38.2 % of the original C and 39.9 % of the original O from PVP remained in the sample.[36] In fact, in that study, which employs a similar nanoparticle synthesis, the Pt content of the sample was initially only 10.5 % by weight and increased to only 25.8% after the high temperature treatment in N_2. This suggests that a significant amount of oxidized carbon is likely in contact with the Pt nanoparticles during the reaction studies we have carried out.

The residual oxidized carbon left behind by partial PVP decomposition likely undergoes varying degrees of reduction depending on the temperature of the H_2 pretreatment. In a study by Borodko, *et al*, the carbonyl group of PVP interacts mores strongly with Pt nanoparticles when oxidized in air at 363 K than when reduced in H_2 at 363 K and this process is reversible.[37] The focus of that study was the oxidation state of surface Pt, but reduction at higher temperatures will also induce changes (probably irreversible) to PVP or residual carbon deposits. As the reduction temperature increases, the oxygenated groups of this residual layer will become hydrogenated and interact more favorably with the oxygen of the C=O group of crotonaldehyde. Upon further temperature increase, the carbon overlayer may densify with a complete loss of oxygenated groups, thus deactivating the catalyst. The role of stabilizing molecules is important and has not been adequately studied for use of colloidally prepared NPs in gas phase heterogeneous catalysis. Even after thermal treatment in O_2 at 623 – 723 K, some organic overlayer remains on the Pt surface and is modified by subsequent H_2 treatment.

3.4. Conclusions

Monodisperse Pt nanoparticles (1.7 – 7.1 nm) synthesized by alcohol reduction method in the presence of poly(vinylpyrrolidone) were supported on mesoporous SBA-15 silica for studies of crotonaldehyde hydrogenation. The activity and selectivity towards crotyl alcohol both increased with increasing particle size. The turnover frequency at 353 K and a H_2/crotonaldehyde ratio of 20 increased from 2.1×10^{-2} to 4.8×10^{-2} s^{-1} and the selectivity to crotyl alcohol increases from 14 % to 34 % as the particle size increased from 1.7 to 7.1 nm. The initial rate of decarbonylation is also particle size dependent; the TOF is 2.5×10^{-3} over Pt(1.7 nm)/SBA-15 and only 1.0×10^{-3} over Pt(7.1 nm)/SBA-15.

The apparent activation energy was not influenced by particle size, being ~ 11 kcal/mol for all catalysts. The reduction temperature influences significantly both the activity and selectivity; there is an optimal reduction temperature of ~ 673 – 723 K for both 1.7 and 7.1 nm Pt nanoparticle catalysts. The dependence of catalytic activity and selectivity on reduction temperature is not due to sintering and therefore it is postulated that residual carbonaceous material on or near the Pt NPs is reduced during H_2 reduction and influences adsorption of crotonaldehyde at the Pt surface.

3.5 References

(1) Aiken, J. D.; Finke, R. G., *J. Mol. Catal. A: Chem.* **1999,** 145, 1.

(2) Roucoux, A.; Schulz, J.; Patin, H., *Chem. Rev.* **2002,** 102, 3757.

(3) Lang, H. F.; May, R. A.; Iversen, B. L.; Chandler, B. D., *J. Am. Chem. Soc.* **2003,** 125, 14832.

(4) Konya, Z.; Puntes, V. F.; Kiricsi, I.; Zhu, J.; Ager, J. W.; Ko, M. K.; Frei, H.; Alivisatos, P.; Somorjai, G. A., *Chem. Mater.* **2003,** 15, 1242.

(5) Stowell, C. A.; Korgel, B. A., *Nano Lett.* **2005,** 5, 1203.

(6) Li, Y.; El-Sayed, M. A., *J. Phys. Chem. B* **2001,** 105, 8938.

(7) Venezia, A. M.; Liotta, L. F.; Pantaleo, G.; La Parola, V.; Deganello, G.; Beck, A.; Koppany, Z.; Frey, K.; Horvath, D.; Guczi, L., *Appl. Catal. A: Gen.* **2003,** 251, 359.

(8) Rioux, R. M.; Song, H.; Hoefelmeyer, J. D.; Yang, P.; Somorjai, G. A., *J. Phys. Chem. B* **2005,** 109, 2192.

(9) Deutsch, D. S.; Siani, A.; Fanson, P. T.; Hirata, H.; Matsumoto, S.; Williams, C. T.; Amiridis, M. D., *J. Phys. Chem. C* **2007,** 111, 4246.

(10) Song, H.; Rioux, R. M.; Hoefelmeyer, J. D.; Komor, R.; Niesz, K.; Grass, M.; Yang, P. D.; Somorjai, G. A., *J. Am. Chem. Soc.* **2006,** 128, 3027.

(11) Rioux, R. M.; Hoefelmeyer, J. D.; Grass, M.; Song, H.; Niesz, K.; Yang, P. D.; Somorjai, G. A., *Langmuir* **2008,** 24, 198.

(12) Rioux, R. M.; Komor, R.; Song, H.; Hoefelmeyer, J. D.; Grass, M.; Niesz, K.; Yang, P. D.; Somorjai, G. A., *J. Catal.* **2008,** 254, 1.

(13) Grass, M. E.; Yue, Y.; Habas, S. E.; Rioux, R. M.; Teall, C. I.; Yang, P.; Somorjai, G. A., *J. Phys. Chem. C* **2008,** 112, 4797.

(14) Gallezot, P.; Richard, D., *Cat. Rev. - Sci. Eng.* **1998,** 40, 81.

(15) Richard, D.; Fouilloux, P.; Gallezot, P. In Proceedings of the 9th International Congress on Catalysis, Calgary, Canada, 1988; Pillips, M. J.; Ternan, M., Eds. Calgary, Canada, 1988; p 1074.

(16) Giroir-Fendler, A.; Richard, D.; Gallezot, P., *Catal. Lett.* **1990,** 5, 175.

(17) Santori, G. F.; Casella, M. L.; Siri, G. J.; Aduriz, H. R.; Ferretti, O. A., *React. Kinet. Catal. Lett.* **2002,** 75, 225.

(18) Englisch, M.; Jentys, A.; Lercher, J. A., *J. Catal.* **1997,** 166, 25.

(19) Delbecq, F.; Sautet, P., *J. Catal.* **1995,** 152, 217.

(20) Mohr, C.; Hofmeister, H.; Radnik, J.; Claus, P., *J. Am. Chem. Soc.* **2003,** 125, 1905.

(21) Carter, J. L.; Cusumano, J. A.; Sinfelt, J. H., *J. Phys. Chem.* **1966,** 70, 2257.

(22) Zanella, R.; Louis, C.; Giorgio, S.; Touroude, R., *J. Catal.* **2004,** 223, 328.

(23) Wang, Y.; Ren, J. W.; Deng, K.; Gui, L. L.; Tang, Y. Q., *Chem. Mater.* **2000,** 12, 1622.

(24) Teranishi, T.; Hosoe, M.; Tanaka, T.; Miyake, M., *J. Phys. Chem. B* **1999,** 103, 3818.

(25) Konya, Z.; Puntes, V. F.; Kiricsi, I.; Zhu, J.; Alivisatos, A. P.; Somorjai, G. A., *Nano Lett.* **2002,** 2, 907.

(26) Zhu, J.; Konya, Z.; Puntes, V. F.; Kiricsi, I.; Miao, C. X.; Ager, J. W.; Alivisatos, A. P.; Somorjai, G. A., *Langmuir* **2003,** 19, 4396.

(27) Boudart, M.; Eley, D. D.; Pines, H.; Weisz, P. B., Catalysis by Supported Metals. In *Advances in Catalysis*, Academic Press: 1969; Vol. Volume 20, pp 153.

(28) Birchem, T.; Pradier, C. M.; Berthier, Y.; Cordier, G., *J. Catal.* **1994,** 146, 503.

(29) Shekhar, R.; Barteau, M. A., *Surf. Sci.* **1994,** 319, 298.

(30) Waghray, A.; Blackmond, D. G., *J. Phys. Chem.* **1993,** 97, 6002.

(31) Singh, U. K.; Vannice, M. A., *J. Catal.* **2000,** 191, 165.

(32) Beccat, P.; Bertolini, J. C.; Gauthier, Y.; Massardier, J.; Ruiz, P., *J. Catal.* **1990,** 126, 451.

(33) Baker, R. T. K.; Prestridge, E. B.; Garten, R. L., *J. Catal.* **1979,** 56, 390.

(34) Tauster, S. J., *Acc. Chem. Res.* **1987,** 20, 389.

(35) Coloma, F.; Sepulveda-Escribano, A.; Fierro, J. L. G.; Rodriguez-Reinoso, F., *Appl. Catal. A: Gen.* **1997,** 150, 165.

(36) Du, Y. K.; Yang, P.; Mou, Z. G.; Hua, N. P.; Jiang, L., *J. Appl. Poly. Sci.* **2006,** 99, 23.

(37) Borodko, Y.; Humphrey, S. M.; Tilley, T. D.; Frei, H.; Somorjai, G. A., *J. Phys. Chem. C* **2007,** 111, 6288.

Chapter 4: Influence of particle size on reaction selectivity in cyclohexene hydrogenation and dehydrogenation over silica-supported monodisperse Pt particles

The role of particle size during the hydrogenation-dehydrogenation of cyclohexene (10 Torr C_6H_{10}, 200-600 Torr H_2, and 273 – 650 K) was studied over a series of monodisperse Pt/SBA-15 catalysts. The conversion of cyclohexene in the presence of excess H_2 (H_2:C_6H_{10} ratio = 20-60) is characterized by three regimes: hydrogenation of cyclohexene to cyclohexane at low temperature (< 423 K), an intermediate temperature range in which both hydrogenation and dehydrogenation occur; and a high temperature regime in which the dehydrogenation of cyclohexene dominates (> 573 K). The rate of both reactions demonstrated maxima with temperature, regardless of Pt particle size. For the hydrogenation of cyclohexene, a non-Arrhenius temperature dependence (apparent *negative* activation energy) was observed. Hydrogenation is structure *insensitive* at low temperatures, and apparently structure *sensitive* in the non-Arrhenius regime; the origin of the particle-size dependent reactivity with temperature is attributed to a change in the coverage of reactive hydrogen. Small particles were more active for dehydrogenation and consistently had lower apparent activation energies than large particles. The selectivity can be controlled by changing the particle size, which is attributed to the structure sensitivity of *both* reactions in the temperature regime where hydrogenation and dehydrogenation are catalyzed simultaneously.

4.1 Introduction

Considerable work has been conducted to demonstrate the effect of particle size on reaction activity.[1] Reactions whose rate varies with particle size are referred to as structure sensitive and those independent of particle size are termed structure insensitive.[2] The effect is often seen in the particle size range of 1 – 5 nm, the region over which the fraction of surface sites with different coordination changes most drastically. At particle sizes above 5 nm, bulk crystal habits have developed and changes in particle size lead to little change in the average coordination number. Experimentally, the apparent sensitivity of a reaction to the structure of a catalyst is determined by measuring the rate of reaction over a series of catalysts with varying particle size (ideally with catalysts who particle size is monodisperse.[3] Here we utilize a similar set of monodisperse Pt supported SBA-15 catalysts as in the previous chapter to correlate the *influence of particle size on selectivity* during the hydrogenation-dehydrogenation of cyclohexene.

The hydrogenation of cyclohexene to cyclohexane at high pressure on supported nanoparticle catalysts at near ambient temperatures[4] is structure insensitive,[5] similar to benzene hydrogenation on supported Pt catalysts.[6] The measurement of the rate of cyclohexene hydrogenation on Pt single crystals under high pressure conditions and near *ambient* temperatures confirms the structure insensitivity of the reaction.[7,8]

The dehydrogenation of cyclohexene to benzene is structure sensitive on close-packed Pt single crystal surfaces; dehydrogenation proceeds more rapidly on the Pt(100) crystal surface than on the Pt(111) crystal surface.[7,8] Two reaction intermediates have been observed spectroscopically on both single crystal surfaces. On Pt(100), 1,3-cyclohexadiene (CHD) is observed, whereas on Pt(111), both the 1,3- and 1,4-CHD

species dehydrogenate to form benzene. The structure sensitivity of cyclohexene dehydrogenation is explained by noting that there is both a fast and slow reaction pathway on Pt(111); the slow 1,4-CHD pathway effectively eliminates surface sites for the faster 1,3-CHD pathway to turnover. The only pathway present on Pt(100) is through 1,3-CHD, where all active sites on Pt(100) participate in the fast reaction pathway.[8]

Both hydrogenation and dehydrogenation products (cyclohexane and benzene) are thermodynamically-allowed and formed over Pt catalysts at intermediate temperatures ($400 \leq T \leq 600$ K). Previous work on silica-supported Pt catalysts demonstrated cyclohexene and benzene are not formed with thermodynamic selectivity.[9] There has been little examination of the influence of surface structure (or particle size) on the *selectivity* of cyclohexene conversion over experimental conditions where the formation of both cyclohexane and benzene is thermodynamically permissible[9] because most experimental studies have focused on conditions where only hydrogenation occurs (low temperature) or conditions where only dehydrogenation (in excess hydrogen)[5,10] occurs (high temperature).[11,12]

Here we examine the effect of particle size on reaction selectivity for the conversion of cyclohexene in excess hydrogen. We demonstrate that in a regime where both cyclohexene and benzene form, the surface is depleted in hydrogen and the particle size influences reaction selectivity through a particle size dependent reactive hydrogen coverage.[13] The hydrogenation of cyclohexene is structure insensitive under conditions of reversible hydrogen adsorption (low temperature) and becomes structure sensitive with an apparent dependence on hydrogen pressure which is much greater than unity. We compare our results with kinetic measurements on platinum single crystals, which

confirm the structure sensitivity of *selectivity* in cyclohexene hydrogenation-dehydrogenation in excess hydrogen.[8]

4.2 Experimental

A series of ~0.6 % Pt/SBA-15 catalysts were used in these experiments. A detailed description of their synthesis and characterization was discussed in chapter 3. Pt nanoparticles between 1.7 and 7.1 nm protected by polyvinylpyrrolidone (PVP) are synthesized by modified alcohol reduction methods to yield nearly monodisperse Pt nanoparticles. After synthesis of the nanoparticles, we encapsulated them in a SBA-15-like structure by direct participation in the hydrothermal process for mesoporous silica formation. The synthesis of SBA-15 is conducted at neutral pH using NaF as a catalyst for hydrolysis of the silica precursor [14], conditions which differ from the original description of SBA-15 synthesis.[3] Catalysts are activated *ex-situ* prior to catalysis by calcination in 20 % O_2/He (or pure O_2) and reduced *in-situ* directly before reaction in order to remove the PVP and adsorbed oxygen from the surface of the particle.[3] A 3.2 % Pt/SiO_2 catalyst prepared by ion-exchange of $Pt(NH_3)_4(OH)_2 \bullet xH_2O$ at pH 9 [15] was used as a standard sample for reaction studies. We reduced this catalyst (herein referred to as Pt(1 nm)/SiO_2) by an identical *in-situ* procedure used for the SBA-15 catalysts.

The particle size determined by selective chemisorption (H_2-O_2 titration) differed from the as-synthesized size measured for the unsupported clusters by x-ray diffraction and transmission electron microscopy[3], which we believe is primarily due to the influence of residual PVP on the surface of the nanoparticle.

Kinetic measurements were conducted in a plug-flow reactor (PFR) operating under differential conditions (conversion varied between 1-20 %). Calcined Pt/SBA-15

catalysts (2-5 mg) diluted in acid-washed low surface area quartz (10-25 mg) were reduced *in-situ* (directly in the PFR) prior to reaction. Helium and H_2 were delivered to the reactor with mass flow controllers (Unit Instruments Corporation, Model UFC 1200) while cyclohexene was pumped (typical volumetric flow rates were 1-10 mL h^{-1}) into the He/H_2 flow by a syringe pump (Cole Parmer). All lines before and after the quartz U-tube reactor were heated to 393 K to prevent condensation of organic compounds. After allowing the catalyst to reach a steady-state activity at 273 or 298 K, the catalyst bed was heated in ascending order and cooled back down to room-temperature. There was no hysteresis in the temperature-dependent activity data suggesting that permanent deactivation at high temperature was minimal. Reactant and product concentrations were measured during the ascending and descending temperature sequence with a gas chromatograph (Hewlett Packard 5890 Series II) equipped with a 10 way-sampling valve allowing simultaneous monitoring of organics with a flame ionization detector (FID) and thermal conductivity detector (TCD) for detection of hydrogen. The mass activity (μmol g^{-1} s^{-1}) for both cyclohexane and benzene were calculated from the measured chromatograph peak area using response factors[16] and assuming a rate equation for a differential reactor. The turnover frequency for both products was calculated by normalizing the mass activity (μmol g^{-1}_{cat} s^{-1}) to the number of surface Pt atoms (Pt_s) determined by H_2-O_2 titration.[3]

Table 4.1. The turnover frequency (TOF) and selectivity for cyclohexene hydrogenation-dehydrogenation and the apparent activation energy (in the linear regime).

Catalyst[a]	Particle size by chemisorption (nm)[b]	Hydrogenation activity[c] (μmol g^{-1} s^{-1})	Hydrogenation TOF[d] (s^{-1})	Hydrogenation E_a[e] (kcal mol^{-1})	Dehydrogenation activity[c] (μmol g^{-1} s^{-1})	Dehydrogenation TOF[d] (s^{-1})	Dehydrogenation E_a[f] (kcal mol^{-1})
3.2% Pt/SiO_2	1	590	3.6	9.6	1427	8.7	16.0
0.6% Pt(1.7 nm)/SBA-15	2.7	41	3.2	8.7	71	5.5	17.1
0.77% Pt(2.9 nm)/SBA-15	3.1	56	3.9	9.1	49	3.4	19.1
0.6% Pt(3.6 nm)/SBA-15	4.2	31	3.7	9.4	15	1.8	20.9
0.62% Pt(7.1 nm)/SBA-15	9.4	19	4.9	9.8	6	1.6	24.2
Pt(111)[g]	--	--	14.6[h]	8.6	--	15.8[h]	17.9
Pt(100)[g]	--	--	1.3[h]	18.8	--	8.6[h]	22.4
Pt(223)[i]	--	--	7.9[j]	5.0	--	0.4	>8

[a] Particle size determined by counting > 200 particles from TEM micrographs.
[b] Determined from the total H_2 uptake after O_2 chemisorption (H_2-O_2 titration) and d(nm) = 1.13/*D*, where *D* is the dispersion.
[c] Standard conditions are 10 Torr C_6H_{10}, 200 Torr H_2, and **313 K** (hydrogenation) or **423 K** (dehydrogenation).
[d] Normalized by the total number of surface atoms measured by H_2-O_2 titration.
[e] Standard conditions were 10 Torr C_6H_{10}, 200 Torr H_2, and 273-323 K for the supported catalysts.
[f] Standard conditions were 10 Torr C_6H_{10}, 200 Torr H_2, and 398-443 K for the supported catalysts.
[g] From reference.[8]
[h] The original reaction conditions were 10 Torr C_6H_{10}, 100 Torr H_2, balance He and temperatures specified in (c). The rates were corrected to standard conditions assuming 0.75 order H_2 dependence for hydrogenation[5] and 0.2 reaction order for dehydrogenation (this work).
[I] From reference.[7]
[j] The original reaction conditions were 7 Torr C_6H_{10}, 70 Torr H_2, balance He. The rates were corrected to standard conditions assuming 0.75 order H_2 dependence for hydrogenation[5] and 0.2 reaction order for dehydrogenation (this work).

4.3 Results and Discussion

4.3.1 Influence of temperature on cyclohexene hydrogenation-dehydrogenation

The temperature dependence of cyclohexene hydrogenation-dehydrogenation can be divided into three regimes (hydrogenation only, hydrogenation + dehydrogenation, and predominantly dehydrogenation).[17] Hydrogenation is the only reaction at low temperatures (≤ 400 K), while simultaneous hydrogenation and dehydrogenation occurs from ~400 to 600 K at standard conditions (10 Torr C_6H_{10}, 200 Torr H_2, balance He). Dehydrogenation is the dominant reaction path at temperatures ≥ 600 K. Figure 4.1 demonstrates that within the three regimes, the hydrogenation rate goes through a well-defined maximum and then decreases with increasing temperature. The third regime is commonly referred to as 'non-Arrhenius or 'bend-over' behavior[18] and has been reported during the hydrogenation of benzene on carbon-supported Fe and Pt catalysts[19,20] the reforming of hexane in excess hydrogen on Pt catalysts[18,21,22], alkane hydrogenolysis[18] and cyclohexene hydrogenation on a Pt(111) and Pt(100) single crystal surfaces.[8,23,24] In the third regime (T > 600 K), the production of cyclohexane has decreased considerably (with turnover rates (~3 s^{-1}) comparable to those measured at 300 K). The rate of dehydrogenation begins to decrease which is probably related to a decrease in cyclohexene coverage and/or an increase in the coverage of carbonaceous deposits.

This non-Arrhenius behavior for the hydrogenation of cyclohexene leads to a negative *apparent* activation energy and is commonly associated with unfavorable adsorption thermodynamics leading to a low coverage of either C_6H_{10} or H_2, respectively. Yoon and Vannice noted a maximum turnover frequency at 473 K for C_6H_6 pressures of 20 – 100 Torr, which decreased to 453 K at lower pressures (< 3 Torr) for C_6H_6

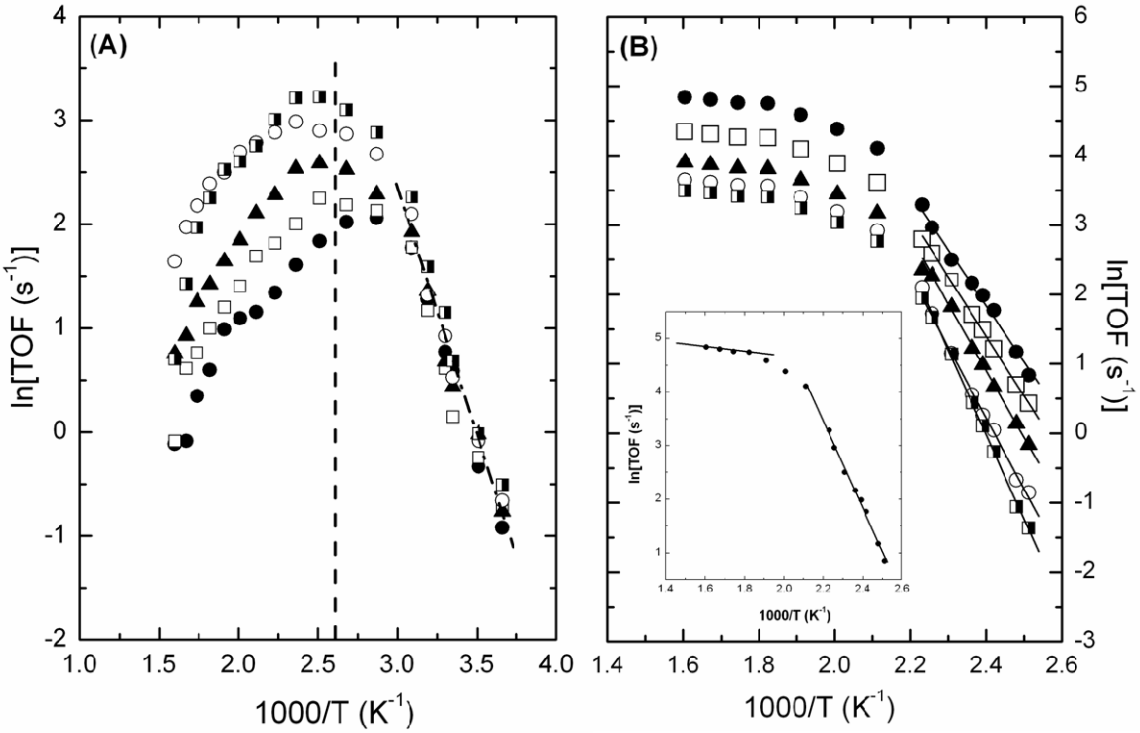

Figure 4.1. Arrhenius plots for cyclohexene (A) hydrogenation and (B) dehydrogenation on (●) 3.2 % Pt(1 nm)/SiO_2; (□) 0.6 % Pt(1.7 nm)/SBA-15; (▲) 0.77 % Pt/(2.9 nm)/SBA-15; (○) 0.6 % Pt(3.6 nm)/SBA-15; and (◨) 0.62 % Pt(7.1 nm)/SBA-15. The Arrhenius plots for hydrogenation undergo a change in the sign of the slope (non-Arrhenius behavior) at a temperature of ~ 350 K for all particle sizes. The Arrhenius plot for dehydrogenation demonstrates the rate begins to level off at a temperature of ~550 K. The inset of (B) shows that the slope at high temperature corresponds to an apparent activation energy (E_{app}) of ~2 kcal mol^{-1}, while the low temperature E_{app} is an order of magnitude larger for the 3.2 % Pt(1 nm)/SiO_2 catalyst. The rates were measured at 10 Torr C_6H_{10}, 200 Torr H_2 and balance He. The dashed vertical line in (A) represents the temperature at which dehydrogenation activity is measured initially.

hydrogenation over a supported-Fe catalyst; the increased benzene partial pressure affords a larger coverage of benzene. Yang and co-workers suggested recently that the 'bend-over' Arrhenius behavior for cyclohexene hydrogenation on Pt(111) was due to low cyclohexene coverage.[23] Low hydrogen coverage has been proposed by others as the cause for non-Arrhenius behavior. Paál measured a maximum rate for hydrocarbon reforming reactions, and demonstrated it is related to a hydrogen coverage effect.[18] As the reaction temperature increases at constant hydrogen pressure, the hydrogen coverage

and the rate of hydrocarbon reforming decreases. Paál suggested that measuring the rate maxima (where the dependence on H_2 is zero order) as function of reaction temperature should yield a 'normal' apparent activation energy.[18] We examine the influence of hydrogen partial pressure on the non-Arrhenius behavior in section 4.3.4.

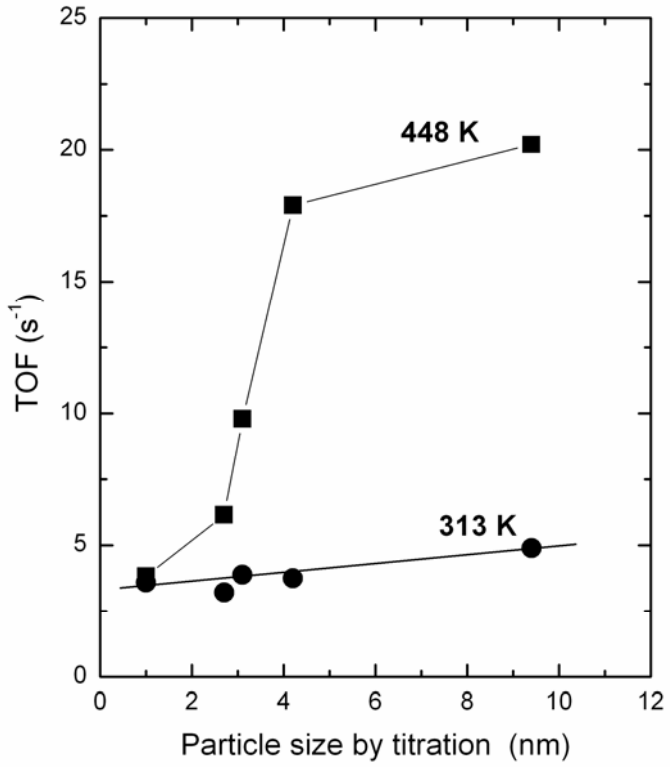

Figure 4.2. The influence of particle size on the turnover rate (normalized to the number of surface atoms determined by H_2-O_2 titration) for cyclohexene hydrogenation at two different temperatures (313 and 448 K). The reaction is structure insensitive at low temperatures, and apparently structure sensitive at high temperatures. This difference in reactivity as a function of temperature and particle size is attributed to change in the coverage of reactive hydrogen.

4.3.2 Temperature dependent structure sensitivity of cyclohexene hydrogenation-dehydrogenation

The activity, turnover frequency (TOF), and apparent activation energy for both the hydrogenation and dehydrogenation of cyclohexene are compiled in Table 4.1. The rates

for both reactions measured on a Pt(111) and Pt(100) single crystal are included.[8] The hydrogenation TOF at 313 K is structure insensitive, the rates are ~3.5 s^{-1} and the apparent activation energy is ~9 kcal mol^{-1}.

Cyclohexene hydrogenation becomes structure-sensitive at low temperature, but as the temperature is increased into the 'non-Arrhenius' regime, the reaction is structure sensitive. Figure 4.2 demonstrates at 448 K, the TOF on Pt(7.1 nm)/SBA-15 is a factor of four greater than the TOF on Pt(1.7 nm)/SBA-15. This difference is proposed to be due to a particle-size dependence on the total H_2 coverage (i.e. a bare surface) or a decreased coverage of a particular population (subspecies) of adsorbed hydrogen (weak, moderately or strongly adsorbed hydrogen). We explore both of these scenarios by examination of published data on the measured differential heat of hydrogen adsorption ($\Delta H_{ads}(\theta = 0)$ dependence) and temperature-programmed desorption (TPD) behavior of silica-supported Pt catalysts. Vannice and co-workers demonstrated there is no dependence of the initial heat of adsorption of H_2 on SiO_2-supported Pt particle size; even though the heat of adsorption of hydrogen on single crystal surfaces is facet-dependent.[25,26] Based on the significant scatter in reported values for the integral (and differential) heats of adsorption for the adsorption of H_2 on silica-supported Pt catalysts and their measurement near room temperature, we propose that the heat of adsorption of a particular population of adsorbed hydrogen is particle-size dependent. TPD of hydrogen demonstrate that there can be up to three different populations of adsorbed hydrogen with desorption temperatures centered at ~370 K, ~600 K and ~740 K.[27] The maximum temperature of desorption for the second desorption state (denoted as β_2) ranges from 410-440 K for small (~1 nm) and 580-600 K for large (5-15 nm) particles

and represents the most relevant hydrogen species present and active on the surface on high temperature side of the rate maxima for the hydrogenation of cyclohexene. The percentage of total hydrogen desorbed as a β_2 species from a series of silica-supported Pt catalysts (in general) increased with increasing particle size. Therefore, the increased activity of the Pt(7.1 nm)/SBA-15 for the hydrogenation of cyclohexene at the higher temperatures is supported by fact that the temperature for hydrogen desorption increases with particle size, while maximum hydrogen desorption from small particles (<3 nm) occurs at much lower temperatures. The particle-size dependent behavior of hydrogen desorption is adequate to explain the particle size dependence of cyclohexene hydrogenation at 448 K: the surface of large particles is covered with adsorbed hydrogen atoms, while 448 K is greater than the maximum desorption temperature of hydrogen for the small particles (~425 K), resulting in a surface with decreased hydrogen coverage relative to the larger particles (~590 K).

The kinetic measurements for the dehydrogenation of cyclohexene at 423 K are reported in Table 4.1. The rate of dehydrogenation is more sensitive to particle size than hydrogenation. Over the 'normal' regime of Arrhenius behavior, the apparent activation energy varies from 16-24 kcal mol^{-1} (Figure 4.1B). At higher temperatures (> 550 K), the rate of dehydrogenation leveled off for all particle sizes. In this regime, very small apparent activation energies (~2-3 kcal mol^{-1}) were measured and the decrease in rate is attributed to decrease in cyclohexene coverage.[19,23] The dependence of the rate on the pressure of hydrogen is minor, and doesn't increase significantly with temperature (H_2 reaction order of 0.2 at 413 K compared with 0.3 at 598 K) (see section 4.3.4).

Table 4.1 also includes the rates measured for cyclohexene hydrogenation and dehydrogenation at high pressures on Pt single crystals. It is apparent from Table 4.1 that the rate of hydrogenation on the single crystal surfaces are on the same order as the Pt/SBA-15 catalyst series, but the rates on the Pt(111) and Pt(223) are significantly higher than the Pt(100) surface. The rates of dehydrogenation are again higher on the Pt(111) surface than the Pt(100) or Pt(223). The noticeable difference is the rate of dehydrogenation measured on the Pt(223). It is an order of magnitude lower than the Pt(1 nm)/SiO_2 catalyst, which presumably have similar surface structures. An explanation for the structure sensitivity on Pt single crystals has been suggested by McCrea and Somorjai based on characterization of the surface under reaction conditions by sum frequency generation surface vibrational spectroscopy.[8] As the temperature is increased to favor dehydrogenation, the (100) surface is more active. A dehydrogenated intermediate, 1,3-cyclohexadiene has been identified on the Pt(100) surface, while two intermediates (1,3 and 1,4-cyclohexadienes) have been identified on the (111) surface by SFG. It is suggested that the 1,3-cyclohexadiene is the involved in a "fast" reaction pathway for benzene formation and the 1,4 species present only on the (111) surface turnovers over to benzene but at a much lower rate because the 1,4-CHD must isomerize to 1,3-CHD before being dehydrogenated to benzene. There is no spectroscopic evidence of either species on the surface of nanoparticles and therefore inappropriate to suggest the presence of one or both species on the nanoparticle surface during turnover explains the apparent structure sensitivity for benzene hydrogenation.

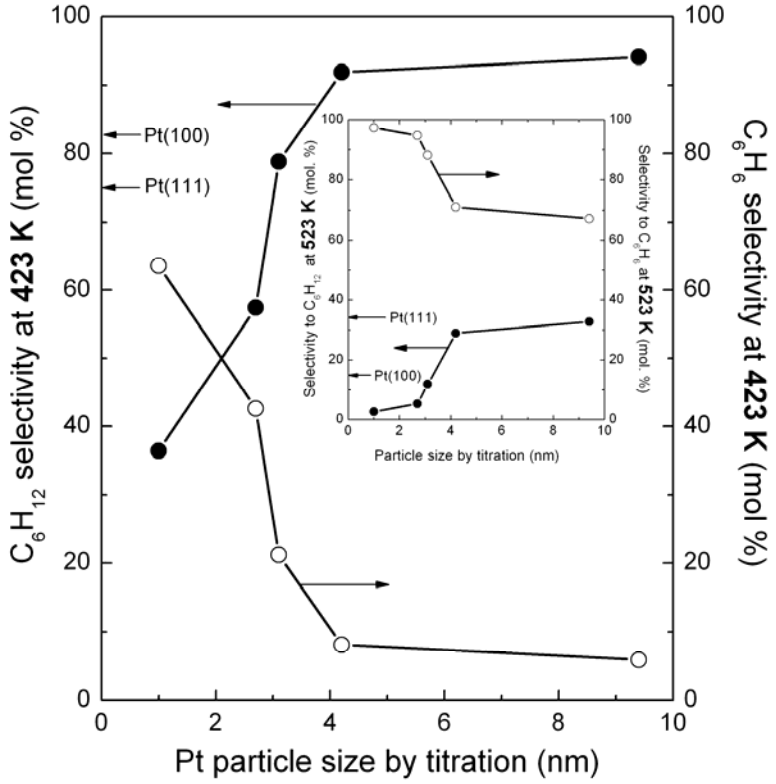

Figure 4.3. The influence of particle size on reaction selectivity during the hydrogenation-dehydrogenation of cyclohexene over the entire series of Pt/SBA-15 catalysts. The reaction conditions are 10 Torr C_6H_{10}, 200 Torr H_2, and 423 K. The inset is the selectivity at 523 K and the same pressure conditions. At 423 K, the particle size dictates selectivity; Pt(1.7 nm) is more selective for the formation of benzene than catalysts with the larger particle size. At higher temperatures, where dehydrogenation dominates, the particle size has a smaller influence on the selectivity to the minor product, cyclohexane. The hydrogenation selectivity is marked on the *ordinate* of the figure (and inset) for Pt(111) and Pt(100) single crystals.[8]

4.3.3 Role of particle size in cyclohexene hydrogenation-dehydrogenation selectivity

The dehydrogenation of cyclohexene is more facile on the smaller particles, while hydrogenation is influenced by particle size in a temperature dependent manner. Figure 4.3 demonstrates the influence of particle size on the selectivity at 10 Torr C_6H_{10}, 200 Torr H_2 and 423 K. The selectivity to benzene is highest (>60 %) on the 1 nm particles and subsequently decreases to less than 10 % on large (7.1 nm) particles. This is a unique demonstration of the influence of particle size on reaction selectivity, and these

conditions in particular demonstrate that the major product can be changed by a change in particle size. The inset demonstrates that the ability of a particle to change the major product is applicable only under certain experimental conditions. At 523 K, the selectivity to benzene is >50 % for all particle sizes, although the selectivity to cyclohexane increases with particle size. The increase in selectivity to cyclohexane at larger particle size is rather significant and related to an increase in hydrogen coverage (see section 4.3.4).

The selectivity to hydrogenation-dehydrogenation products during cyclohexene conversion over a wide temperature range is also facet-dependent, as demonstrated by Somorjai and co-workers.[8,23,24] On Pt(100) at 423 K, the selectivity to cyclohexene (10 Torr C_6H_{10}, 100 Torr H_2) is 82 %, while the corresponding selectivity is 75 % on Pt(111), while at 523 K, the higher selectivity to the hydrogenation product is now measured on the (111) surface (~34 %), while the hydrogenation selectivity on Pt(100) is only ~14 %. Figure 4.3 demonstrates that the selectivity for both single crystal matches that of the 3 nm diameter particle, while the selectivity at the higher temperature (523 K) demonstrate the (111) single crystal behaves more like the largest Pt particle, and the Pt(100) continues to behave more like a 3 nm particle.

4.3.4 Influence of hydrogen pressure on cyclohexene hydrogenation-dehydrogenation activity and selectivity

The influence of hydrogen partial pressure is shown in Figure 4.4 and 4.5 for the Pt(1 nm)/SiO_2 sample which we believe has the lowest coverage of hydrogen under reaction conditions.[28] As the pressure of hydrogen increases from 200 to 600 Torr, the

dependence of the rate of the hydrogenation reaction changed considerable over a 400 K temperature interval. At low temperatures (near ambient), the reaction order in H_2 was

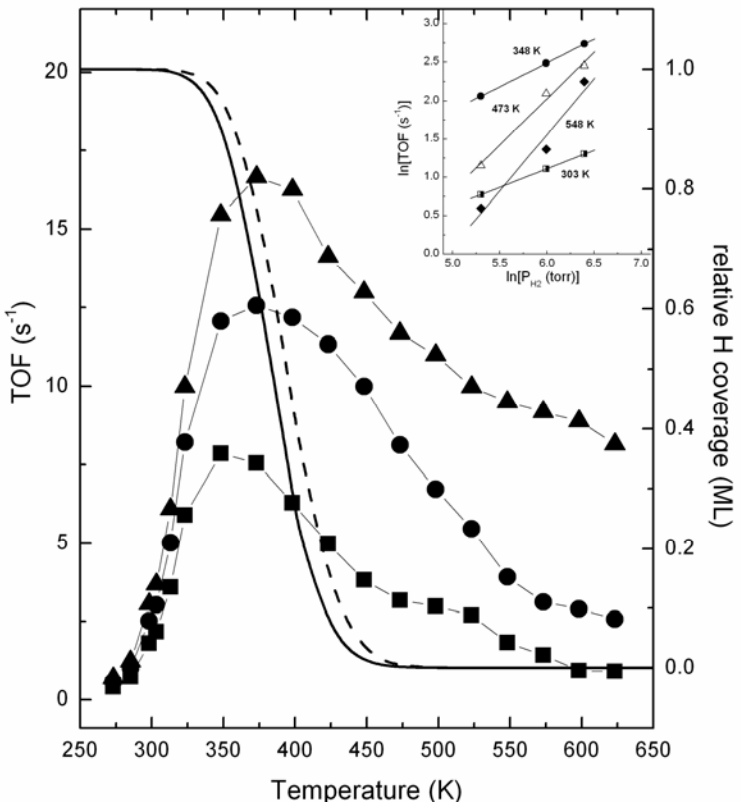

Figure 4.4. The influence of H_2 pressure ((■) 200 Torr; (●) 400 Torr; and (▲) 600 Torr) on the rate of cyclohexene hydrogenation on 3.2 % Pt(1 nm)/SiO_2 over the entire temperature range (i.e. normal and non-Arrhenius region). The solid and dashed lines represent the calculation of hydrogen coverage using the initial and monolayer heat of adsorption values[29] in the Temkin isotherm for gas-phase hydrogen pressures of 200 and 600 Torr H_2, respectively. The inset demonstrates the change in H_2 reaction order with temperature. At low temperatures (~303 K), the ~½ order dependence of the reaction rate on the pressure of hydrogen is apparent. The reaction order in H_2 increases as the reaction temperature increases: 0.48 (303 K); 0.61 (348 K); 1.2 (473 K); and 1.47 (548 K).

0.48 (see inset of Figure 4.5), which is in good agreement with previous measurements on supported Pt catalysts[10] and a Pt powder[5]. As the temperature increased, the reaction order became more positive, and approached values greater than unity. At 548 K, the reaction order in H_2 was ~1.5. A first-order dependence on hydrogen can be derived

easily if the addition of a second hydrogen to the half-hydrogenated cyclohexyl (C_6H_{11}) species is rate-determining, but there is no straightforward way based on Langmuir-Hinshelwood kinetic schemes to arrive at a 3/2 order dependence on hydrogen. As the H_2 pressure was doubled from 200 to 400 Torr, there was an increase in the temperature of maximum rate (from ~348 to 373 K). The increase in rate over the entire temperature range suggests that the hydrogen content on the surface increases. Figure 4.5 demonstrates that the influence of increased hydrogen pressure is less dramatic for the dehydrogenation pathway. At low temperatures (413 K), the pressure dependence on H_2 is 0.2 (inset of Figure 4.5). At a temperature of 598 K, the dependence on H_2 does not changed substantially. This result is anticipated due to the fact that dehydrogenation only needs hydrogen to remove carbonaceous residues from the surface[18] and the weak dependence on hydrogen may suggest that most of the deposited carbon is initially mobile enough to migrate to the support without deactivating the catalyst.[30]

The increase in H_2 pressure increased the selectivity to cyclohexane over the entire temperature range, but it is most apparent at high temperatures (non-Arrhenius behavior regime) where the steady-state coverage of hydrogen is affected to the greatest extent allowing for higher hydrogenation activity. Vannice and co-workers reported the integral heat of adsorption was invariant with particle size for a series of SiO_2-supported Pt catalysts synthesized by standard impregnation methods.[29] An initial heat of adsorption measured on Pt/SiO_2 catalyst with an average particle size of 2 nm was 26.3 kcal mol^{-1} while the integral heat of adsorption at full monolayer coverage was 24.5 kcal mol^{-1} (these values were used for the Temkin isotherms calculated in Figure 4.4 as a function of

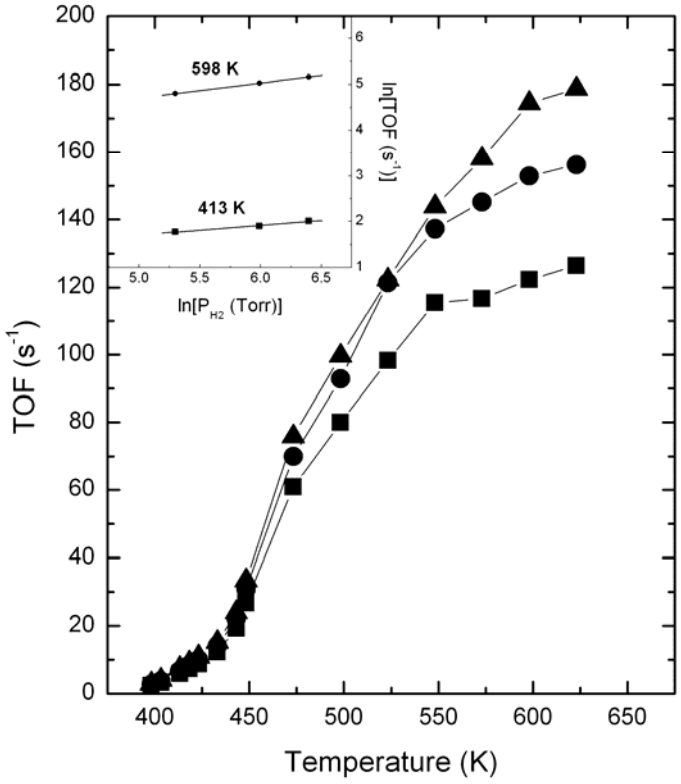

Figure 4.5. The influence of H_2 pressure ((■) 200 Torr; (●) 400 Torr; and (▲) 600 Torr) on the rate of cyclohexene dehydrogenation on 3.2 % Pt(1 nm)/SiO_2 over the entire temperature range. The inset demonstrates the change in H_2 reaction order with temperature. At 413 K, the dependence on H_2 is positive but low (~0.2), and as the temperature increases the dependence on hydrogen increases only slightly (reaction order at 598 K is 0.3).

H_2 partial pressure). These differential heats of adsorption were measured at room temperature and temperature-programmed desorption (TPD) studies by Sermon[27] on supported Pt catalysts demonstrate hydrogen requires a range of (higher) temperatures to fully desorb (apparent desorption energy, $E_d \geq \Delta H_{ads}$) due to the adsorption of different hydrogen populations on energetically non-equivalent sites, suggesting that the two reactions segregate on the surface.[9] Although the coverage determined by the Temkin plot calculates zero coverage at temperatures > 450 K (Figure 4.4), TPD studies demonstrate that hydrogen desorbs at temperatures > 600 K, with the larger particles

demonstrating more high-temperature hydrogen desorption.[27] We believe that this high-temperature population of adsorbed hydrogen increases with increasing hydrogen pressure (in a particle-size dependent manner) and these hydrogen species are responsible for the increased hydrogenation activity with particle size at higher temperatures (Figure 4.4).

4.4. Conclusions

The role of Pt particle size (1.7 – 7.1 nm) on the *selectivity* to hydrogenation and dehydrogenation products during the conversion of cyclohexene in excess H_2 was examined. The temperature dependence of the reaction is characterized by three regimes: hydrogenation only at low temperature (≤400 K); simultaneous hydrogenation and dehydrogenation at intermediate temperatures ($400 \leq T \leq 550$ K), and predominantly dehydrogenation at high temperatures (> 550 K). During simultaneous hydrogenation-dehydrogenation, the rate of hydrogenation decreases with increasing temperature (non-Arrhenius behavior), while benzene formation behaves in a normal Arrhenius manner. At high temperatures, where dehydrogenation dominates, the apparent activation energy remains positive but decreases substantially. The rate of dehydrogenation of cyclohexene to benzene decreases monotonically over the experimental particle size and the apparent activation increases linearly as the metallic dispersion increases. The hydrogenation of cyclohexene to cyclohexane is structure-insensitive under conditions of reversible H_2 adsorption at low temperatures, but becomes structure sensitive at high temperatures due to a particle size dependence on reactive hydrogen coverage. The selectivity was particle size dependent in the pressure regime studied here (H_2:C_6H_{10} = 20-60) due to a particle-size reactive hydrogen coverage dependence that causes the hydrogenation pathway to

become structure sensitive at temperatures where the dehydrogenation of cyclohexene to benzene is structure sensitive. This work demonstrates that under a particular set of reaction conditions, the selectivity during the conversion of cyclohexene can be influenced by particle size.

4.5. References

(1) Che, M.; Bennett, C. O. *Adv. Catal.* **1989**, *36*, 55.

(2) Boudart, M. *Adv. Catal.* **1969**, *20*, 153.

(3) Rioux, R. M.; Song, H.; Hoefelmeyer, J. D.; Yang, P.; Somorjai, G. A. *J. Phys. Chem. B* **2005**, *109*, 2192.

(4) Song, H.; Rioux, R. M.; Hoefelmeyer, J.D.; Komor, R.; Niesz, K.; Grass, M.; Yang, P.; Somorjari, G. A. *J. Am. Chem. Soc.* **2006**, *128*, 3027

(5) Segal, E.; Madon, R. J.; Boudart, M. *J. Catal.* **1978**, *52*, 45.

(6) Dorling, T. A.; Moss, R. L. *J. Catal.* **1966**, *5*, 111.

(7) Davis, S. M.; Somorjai, G. A. *J. Catal.* **1980**, *65*, 78.

(8) McCrea, K. R.; Somorjai, G. A. *J. Mol. Catal. A: Chem.* **2000**, *163*, 43.

(9) Sermon, P. A.; Georgiades, G.; Martin-Luengo, M. M. A.; N., P. *Proc. R. Soc. London, A* **1987**, *410*, 353.

(10) O'Rear, D. J.; Löffler, D. G.; Boudart, M. *J. Catal.* **1985**, *94*, 225.

(11) Cogen, J. M.; Ezaz-Nikpay, K.; Fleming, R. H.; Baumann, S. M.; Maier, W. F. *Angew. Chem. Int. Ed. Engl.* **1987**, *26*, 1182.

(12) Molnár, É.; Tasi, G.; Kónya, Z.; Kiricsi, I. *Catal. Lett.* **2005**, *101*, 159.

(13) Zaera, F. *J. Phys. Chem. B* **2002**, *106*, 4043.

(14) Kim, J. M.; Han, Y. J.; Chmelka, B. F.; Stucky, G. D. *Chem. Commun.* **2000**, 2437.

(15) Singh, U. K.; Vannice, M. A. *J. Catal.* **2000**, *191*, 165.

(16) Deitz, W. A. *J. Gas Chromatogr.* **1967**, *5*, 68.

(17) Fási, A.; Pálinkó, I.; Katona, T.; Bartók, M. *J. Catal.* **1997**, *167*, 215.

(18) Bond, G. C.; Paal, Z. *Appl. Catal. A: Gen.* **1992**, *86*, 1.

(19) Yoon, K. J.; Vannice, M. A. *J. Catal.* **1983**, *82*, 457.

(20) Orozco, J. M.; Webb, G. *Appl. Catal.* **1983**, *6*, 67.

(21) Wootsch, A.; Paál, Z. *J. Catal.* **1999**, *185*, 192.

(22) Wootsch, A.; Paál, Z. *J. Catal.* **2002**, *205*, 86.

(23) Yang, M.; Rioux, R. M.; Somorjai, G. A. *J. Catal.* **2006**, *237*, 255.

(24) Bratlie, K. M.; Flores, L. D.; Somorjai, G. A. *Surf. Sci.* **2005**, *599*, 93.

(25) McCabe, R. W.; Schmidt, L. D. *Surf. Sci.* **1976**, *60*, 85.

(26) McCabe, R. W.; Schmidt, L. D. *Surf. Sci.* **1977**, *65*, 189.

(27) Vong, M. S. W.; Sermon, P. A. *J. Chem. Soc., Faraday Trans.* **1987**, *83*, 1369.

(28) The entire Pt/SBA-15 series domonstrates increase in rate with increasing hydrogen pressure. The dependence of the rate of hydrogenation was highly sensitive to the partial pressure of hydrogen over the 400 K interval shown in Figure 4.4.

(29) Sen, B.; Vannice, M. A. *J. Catal.* **1991**, *130*, 9.

(30) Parera, J. M.; Figoli, N. S.; Traffano, E. M.; Beltramini, J. N.; Martinelli, E. E. *Appl. Catal.* **1983**, *5*, 33.

Chapter 5: Silver ion mediated shape control of platinum nanoparticles: Removal of silver by selective etching leads to increased catalytic activity

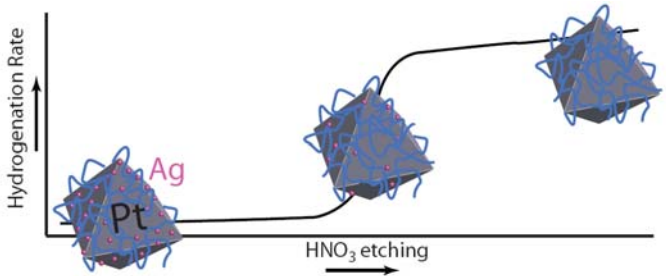

A procedure has been developed for the selective etching of silver from platinum nanoparticles of well-defined shape, resulting in the formation of nearly elementally pure Pt cubes, cuboctahedra, or octahedra, with a largest vertex-to-vertex distance of ~ 9.5 nm from Ag-modified Pt nanoparticles. The characterization of mesoporous silica-supported Pt nanoparticles by XRD, TEM, and N_2 adsorption measurements demonstrated that the structure of the nanoparticles and the mesoporous support was conserved after etching in concentrated nitric acid. Both elemental analysis and ethylene hydrogenation indicated that etching of Ag is only effective when $[HNO_3] \geq 7$ M; below this concentration, the removal of Ag is limited to ~ 10 %. The activity for ethylene hydrogenation increased by four orders of magnitude after etching Pt octahedra containing the highest fraction of silver. High-resolution transmission electron microscopy of the unsupported particles after etching demonstrated that etching does not alter the surface structure of the Pt nanoparticles. High nitric acid concentration led to decomposition of the capping agent, polyvinylpyrollidone (PVP).

5.1 Introduction

Nanoparticles (NPs) synthesized by solution-phase methods are of interest for applications in catalysis, either suspended in solution[4] or deposited on a solid support.[3,5,6] One area of recent interest in catalysis is the effect of NP shape on catalytic activity[2,7-11] and selectivity.[12,13] Many routes to shape control of NPs have been explored, including control via ligand interactions,[14-16] pH,[7] temperature,[17] electrochemical methods,[11,18] and the addition of other (sacrificial) metal ions[19-21] or NP seeds.[22] Shape control of NPs for catalysis is important because the shape of the particle determines which crystal faces are exposed[19] and the proportion of surface atoms with various metal coordination environments.[23]

Previously my group used Ag^+ ions to control the shape of Pt NPs[19] in an effort to elucidate how NP shape affects catalytic activity and selectivity.[2,3] Pt cubes, cuboctahedra, or octahedra were synthesized with ≥ 80% selectivity for each shape by adding different concentrations of $AgNO_3$ in a solution-based polyol synthesis and using polyvinylpyrrolidone (PVP) as a stabilizing polymer. Although initial results (X-ray diffraction (XRD) and energy dispersive X-ray spectroscopy (EDX)) indicated Ag was not present in the NPs after removing excess AgCl by centrifugation, it was later determined that residual Ag of up to ~ 20 at % of metal is still present in the NPs. In a subsequent paper, we found that Ag acts as a poison for the hydrogenation of ethylene by Pt and the amount of Ag in the NPs can be directly correlated to the decrease in catalytic activity.

We demonstrate post-synthesis etching of Ag from unsupported and supported Pt NPs synthesized in the presence of $AgNO_3$, and the subsequent use of the etched

supported NPs as hydrogenation catalysts. Nitric acid etching of Ag is a well-studied system because it is the primary method for synthesis of $AgNO_3$ from elemental silver.[24] The dependence of etching on temperature, HNO_3 concentration, and silver particle size (mm-range) is well-documented.[24-27] The reaction proceeds at HNO_3 concentrations between 3.8 and 4.9 M with the overall stoichiometry:

$$4HNO_3(aq) + 3Ag(s) \rightarrow 3AgNO_3(aq) + NO(g) + 2H_2O(l) \quad (5.1)$$

For [HNO_3] of 4.9 – 7.1 M, the stoichiometry is

$$2HNO_3(aq) + Ag(s) \rightarrow AgNO_3(aq) + NO_2(g) + H_2O(l) \quad (5.2)$$

Platinum is resistant to etching by nitric acid, usually being dissolved with aqua regia (70 % concentrated hydrochloric acid and 30 % concentrated nitric acid).[28] The difference in reactivity of Pt and Ag towards nitric acid enabled us to modify the Pt-Ag NPs post-synthesis to produce Pt NPs of well-defined shapes with reduced Ag content.

Post-synthetic chemical modification of nanoparticles has previously been used to synthesize nanostructures with a variety of properties. For example, Chen *et al.* synthesized Pd-Ag and Pt-Ag nanoboxes using galvanic replacement of Ag from Ag nanocubes with Na_2PdCl_4 or Na_2PtCl_6.[21] Similarly, Au nanoboxes and nanoframes were formed by dealloying Au/Ag nanoboxes using an aqueous etchant.[29] Post-synthesis etching of bimetallic nanostructures is a novel approach to synthesize new nanostructures.

5.2 Experimental

5.2.1 Nanoparticle Synthesis

A detailed description of the synthesis of the NPs has been published elsewhere[19] and only a brief description is given here. The synthesis of Pt cubes began with the

introduction of 0.5 mL of 2 mM silver nitrate ($AgNO_3$, 99+%, Sigma-Aldrich) solution in ethylene glycol (EG, min. 98%, EMD) to boiling EG (2.5 mL), followed by the immediate introduction of 3 mL poly(vinylpyrrolidone) (PVP, MW = 55 K, Sigma-Aldrich, 375 mM) and 1.5 mL hexachloroplatinic acid ($H_2PtCl_6 \cdot 6H_2O$, 99.9%, metals basis, Alfa-Aesar, 62.5 mM) EG solutions over 16 minutes by the injection of small aliquots every 30 s. The resulting mixture was heated at reflux for an additional five minutes, cooled, and precipitated with acetone. The solid was collected by centrifugation and redispersed in ethanol. Insoluble AgCl in the ethanol was removed (confirmed by UV-Vis spectroscopy[19] and XRD) by centrifugation and the supernatant was precipitated with hexanes and again dispersed in ethanol. Increasing the molarity of the $AgNO_3$ solution to 20 mM and 60 mM led to the selective formation of cuboctahedral and octahedral particles, respectively. Pt NPs without Ag (denoted as Pt(no Ag)) were synthesized by following the same procedure outlined above without the addition of $AgNO_3$.

5.2.2 Catalyst Synthesis

A detailed procedure for the synthesis of catalysts by NP encapsulation (NE) in high surface-area mesoporous silica (SBA-15) can be found elsewhere.[3] After a second precipitation with hexanes, the NPs were dispersed in 23.7 mL of an aqueous triblock co-polymer solution (Pluronic P123, $EO_{20}PO_{70}EO_{20}$, EO = ethylene oxide, PO = propylene oxide, BASF, 750 mg) and stirred for 1 h at 313 K, followed by the quick addition of an aqueous solution (114 μl) of 0.5 M sodium fluoride (NaF, 99.99%, Aldrich) and 1.2 mL tetramethyl orthosilicate (TMOS, 98%, Aldrich) to the reaction mixture, and stirred for one day at 313 K. The resulting slurry was aged for an additional day at 373 K in a

closed vessel. After filtering and washing the brown precipitate with water and ethanol, the catalyst was dried in a convection oven overnight at 373 K. The resulting material, consisting of Pt-Ag bimetallic nanoparticles supported on a SBA-15 like mesoporous material are referred to as Pt(shape)/SBA-15 where "shape" is either octahedra, cuboctahedra, or cubes depending on the amount of silver used in the synthesis of the NPs. Platinum and silver loadings were determined by inductively coupled plasma optical emission spectroscopy (ICP-OES) at Galbraith Laboratories (Knoxville, TN). A Pt/SiO_2 catalyst without PVP, prepared by strong electrostatic adsorption, with a particle size of ~ 9 nm was used for comparison.[30]

5.2.3 Etching of Pt(shape)/SBA-15 Catalysts

Silver was etched from the supported Pt(shape)/SBA-15 catalysts in aqueous nitric acid solutions (EMD Nitric Acid, 15.7 M) at 333 ± 2 K for 0.5 h with stirring. After etching, the catalysts were filtered with a large excess of water, rinsed with ethanol and dried overnight at 373 K. A note of caution with this etching procedure: NO_2 forms during the etching process and concentrated HNO_3 is very corrosive.

5.2.4 Etching of Unsupported Pt Nanoparticles

The etching of unsupported Pt NPs was similar to the supported catalyst samples. A sample of Pt NPs (~1 mg Pt) was dispersed in water, and 15.7 M HNO_3 was added to obtain the desired [HNO_3]. After stirring at 333 K for 0.5 h, the particles were precipitated with acetone, centrifuged, and redispersed in ethanol. Prior to infrared (IR) spectroscopy measurements (discussed below), the Pt NP sols were precipitated with hexanes and redispersed in ethanol four times to remove excess PVP. A note of caution

with this etching procedure: NO_2 forms during the etching process and concentrated HNO_3 is very corrosive.

5.2.5 Physical and Chemical Characterization of Pt Nanoparticles and Pt/SBA-15 Catalysts

Transmission electron microscopy (TEM) experiments were carried out on a Philips/FEI Tecnai 12 microscope operated at 100 kV at the Robert D. Ogg Electron Microscope Laboratory at the University of California, Berkeley. Catalysts were subjected to ultrasonication in acetone for 10 s, dropped on continuous carbon film coated copper grids (Ted Pella), and dried in air. The unsupported NPs diluted in ethanol were treated similarly, but without ultrasonication. High-resolution TEM (HRTEM) experiments were carried out on a Phillips CM200/FEG operated at 200 kV at the National Center for Electron Microscopy (NCEM) at the Lawrence Berkeley National Laboratory (LBNL). XRD patterns were measured on a Bruker D8 GADDS diffractometer using Co K_α radiation (λ = 1.79 Å).

5.2.6 Diffuse Reflectance Infrared Study of CO Adsorption on Pt(shape)/SBA-15 Catalysts

In-situ diffuse-reflectance infrared Fourier transform spectroscopy (DRIFTS) was used to study the adsorption of CO on Pt(octahedra)/SBA-15 catalysts. Experiments were conducted with a Nicolet Nexus 670 spectrometer equipped with a Thermo Spectra-Tech controlled atmosphere-diffuse reflection cell. Samples (~10 mg) of unetched and etched catalysts were calcined in flowing O_2 at 673 K *ex-situ* for 12 h, followed by an *in-situ* reduction in 10 % H_2/He at 30 cm^3 min^{-1} at 573 K. A single-beam spectrum (2 cm^{-1} resolution, 128 scans) of the freshly reduced catalyst was obtained at 300 K in 30 cm^3

min^{-1} He and used as the background for spectra of the same catalyst after exposure to gas-phase CO at 300 K. Samples were exposed to a 30 cm^3 min^{-1} mixture of 10 % CO/He for 0.5 h at 300 K, followed by purging in 30 cm^3 min^{-1} He at 300 K. The spectra of adsorbed CO were recorded after purging the catalyst sample with He for 0.5 h (no changes in the spectra were observed after this time).

5.2.7 Attenuated Total Reflection Infrared Spectroscopy of Unsupported Pt NPs

After etching and four wash-precipitation cycles, the NPs were dispersed in 200 μl ethanol to obtain a concentrated NP sol. Attenuated total reflection Fourier transform infrared (ATR-FTIR) (Nicolete Avatar 360) spectra were taken after placing five drops (~50 μl each) of the Pt NP sol onto a ZnSe ATR crystal drop by drop. All spectra were obtained by averaging 8 scans at 2 cm^{-1} resolution.

5.2.8 Ethylene Hydrogenation by Unetched and Etched Pt(shape)/SBA-15

Catalytic reactions were carried out in a Pyrex U-tube plug-flow reactor. The specific details of the reactor system have been previously reported.[5] Reaction rate measurements were conducted at differential conditions (all conversions were < 10%). The catalyst (1 – 40 mg) was diluted with low-surface area, acid-washed quartz in a 1:5 w/w ratio (catalyst:quartz). The turnover frequency (TOF) was estimated by normalizing reaction data to the geometrically calculated number of surface atoms (based on TEM measurements and assuming an average Pt surface density of 1.25 x 10^{19} atoms m^{-2}),[31] and the Pt loading measured by ICP-OES.

5.3 Results and Discussion

5.3.1 Summary of Previous Results from this System and Motivation for Current Study

In the initial work, we synthesized Pt NPs of well-defined shape with a largest vertex-to-vertex distance < 10 nm by the addition of $AgNO_3$ into the reaction mixture.[19] As the $AgNO_3$ concentration used in the synthesis was increased, Pt cubes, cuboctahedra, and octahedra were formed, each with > 80% selectivity. It was concluded that Ag was removed from the NPs after washing them repeatedly in ethanol/hexanes, based on the absence of a Ag peak in the EDX spectrum for washed Pt(octahedra) as well as the absence of Ag X-ray diffraction peaks or any shift in the position of the Pt diffraction peaks.[19] High-resolution (synchrotron-based) XRD confirmed that there was no formation of a Pt-Ag alloy in the Pt(octahedra) nor were separate Ag peaks detected.[32] Single particle EDX studies indicated that up to ~ 15 at % Ag remained in the Pt(octahedra) sample after washing (data not shown).

In an effort to study the effect of NP faceting on catalysis, the three NP shapes were loaded onto SBA-15 and their activity for the hydrogenation of ethylene was measured[2]. In this previous study, ICP-OES indicated that Pt(cubes), Pt(cuboctahedra), and Pt(octahedra) supported on SBA-15 had Ag contents of 1.4 %, 9.5 %, and 11.5 % of the total metal (Ag/(Pt + Ag)×100%), respectively. The catalytic activity decreased with increasing Ag in the catalysts; the turnover frequencies (TOF) (in s^{-1}) for Pt(cubes), Pt(cuboctahedra), and Pt(octahedra) supported on SBA-15 were 8.6, 0.4, and 0.02, respectively. In contrast, the TOF on Pt(111) and Pt(100) single crystals is 4 – 9 s^{-1} for at same reaction conditions[33]. It was concluded that the Ag content, and not the NP faceting, was responsible for the change in activity.

The results of these two studies motivated us to develop a method for the removal of Ag from the Pt(cubes), Pt(cuboctahedra), and Pt(octahedra) NPs. In this study, we

demonstrate that Ag can be removed from the NPs without loss of shape and that after Ag removal, the TOF for ethylene hydrogenation is comparable to the TOF for a Pt(no Ag)/SBA-15 catalyst prepared without $AgNO_3$.

5.3.2 Nanoparticle Synthesis

The slow addition of separate PVP and $H_2PtCl_6 \cdot 6H_2O$ solutions to boiling EG caused the color of the solution to change from yellow to dark brown, indicating the fast reduction of Pt(IV) to Pt(0). If Ag^+ ions were not added prior to the introduction of the Pt salt, a distribution of Pt particle shapes were obtained, dominated by cubes with rounded corners.[19] The addition of varying concentrations of $AgNO_3$ effectively modifies the growth rates along the <111> and <100> directions, providing shape control of the Pt NPs. At a $AgNO_3$ concentration of 1.1 mol % (relative to Pt salt concentration), cubes formed with ~ 80 % selectivity, while at 11 % and 32 mol % $AgNO_3$, cuboctahedra and octahedra formed with ~ 100 % and 80 % selectivity, respectively. In the case of the cubes and octahedra syntheses, the minor shape is tetrahedral. For all NPs, the largest vertex-to-vertex distance is ~ 9.5 nm regardless of shape with size dispersion of ~ 7 % (percent standard deviation). Cubes and octahedra are terminated entirely by (100) and (111) surfaces, respectively, while cuboctahedra are terminated by six (100) and eight (111) surfaces. UV–Vis absorption spectroscopy indicated the presence of reduced Ag_4^{2+} species during the early stages of synthesis, with the formation of AgCl particles at longer synthesis times in the case of the octahedra.[19] It is believed that the mechanism for Pt NP growth involves enhanced growth along the <100> and/or suppressed growth along <111> directions due to the introduction of Ag^+ ions with strong adsorption on {100} terminated Pt surfaces. AgCl can be removed from Pt octahedra by repetitive

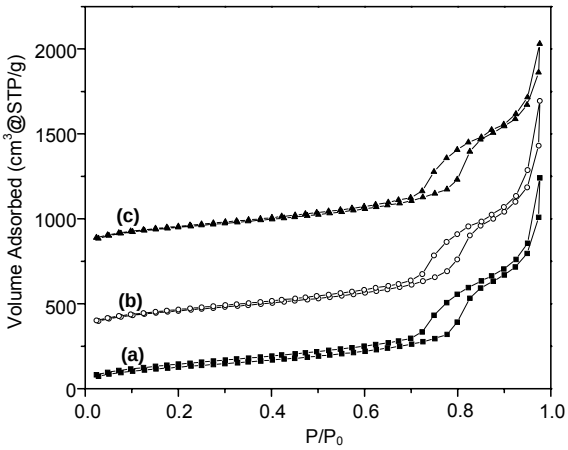

Figure 5.1: N_2 adsorption/desorption isotherms for Pt(octahedra)/SBA-15 (a) as synthesized, and after etching with [HNO_3] of (b) 4 M and (c) 15 M. Isotherms are offset for clarity.

centrifugation and redispersion after Pt particle formation as determined by UV–Vis spectroscopy[19] and elemental analysis (Table 5.1 – Pt(octahedra) are synthesized with 32 mol % Ag). However, ICP-OES elemental analysis performed in this study suggests that little, if any, silver is removed from Pt cubes or cuboctahedra by centrifugation (Table 5.1 – Pt(cuboctahedra) and Pt(cubes) are synthesized with 10.7 and 1.1 mol % Ag respectively).

5.3.3 Catalyst Synthesis

After purification of the Pt NPs, they were introduced into an aqueous solution of triblock co-polymer at 313 K and stirred for 1 h to ensure complete mixing of Pt particles and Pluronic. Brown precipitates formed within five min of the addition of 0.5 M NaF and TMOS. The supernatant was colorless and transparent, indicating the Pt colloids incorporated into or on the surface of the silica matrix. The NPs (~ 9 nm) are larger than the pores (~ 8 nm) (Figure 5.1) of the support, suggesting that a majority of the NPs are located on the exterior of the SBA-15 particles; this is consistent with TEM observations. The particles are often grouped together, but do not appear to be in contact with each

other (Figure 5.2). Particle sizes determined by XRD before and after encapsulation are in good agreement.[3]

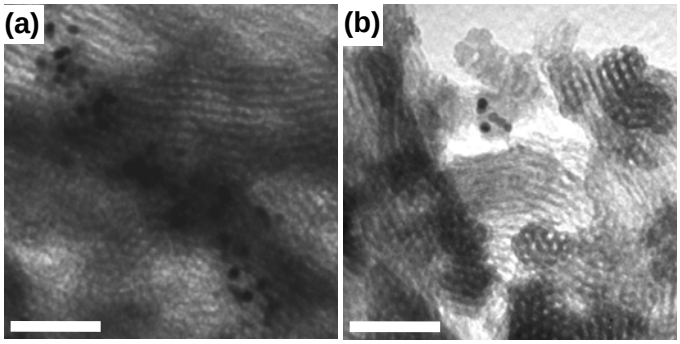

Figure 5.2. TEM images of Pt(octahedra)/SBA-15 (a) before etching and (b) after 10 M HNO_3 etching. The micrographs demonstrate both the nanoparticles and support are visually unchanged by the etching procedure. The nanoparticles tend to cluster in groups, but do not aggregate after treatment – in oxygen or hydrogen – at temperatures between 373 and 573 K. Scale bars are 100 nm.

Table 5.1: Elemental analysis and catalytic properties of Pt(shape)/SBA-15

sample	$[HNO_3]$ (M)[a]	% Pt[b]	ppm Ag[b]	Ag/(Pt+Ag)×10^2 [c]	% Ag remaining	$TOF_{initial}$ (s^{-1})[d]
Pt(No Ag)/SBA-15[e]	0	0.67	< 56	< 1.4	--	34
	10	0.65	--	--	--	33
Pt(cube)/SBA-15	0	0.83	< 53	< 1.1	--	6.3
	10	0.82	< 27	< 0.59	--	34
Pt(cuboctahedra)/SBA-15	0	0.65	544	15.1	--	0.009
	10	0.66	< 42	< 1.1	< 7.3	9.1
Pt(octahedra)/SBA-15[f]	0	0.76	500	11.5	--	0.1
	1	0.85	489	10.3	89.6	0.3
	6	0.86	466	9.7	84.3	0.7
	8	0.84	82	< 1.8	< 15.7	26
	10	0.86	< 76	< 1.6	< 13.9	28
Pt(octahedra)/SBA-15 #2[f]	0	0.85	748	15.8	--	0.009
	10	0.82	< 62	< 1.4	< 8.9	8.3
Pt/SiO_2[g]	--	1.02	--	--	--	8.0

[a] Catalyst etching performed at 333 K with stirring for 0.5 h in an aqueous solution of nitric acid at the indicated concentrations.
[b] Determined by ICP-OES.
[c] Represents the mole percent of total metal that is Ag.
[d] Reaction conditions for ethylene hydrogenation are 10 Torr C_2H_4, 200 Torr H_2 in He (1 atm total) at 300 K.
[e] Sample prepared without silver. The Pt precursor is 99.9% pure. The Ag content of this sample is assumed to be the detection limit.
[f] Samples were prepared by the same method.
[g] Catalyst synthesized by electrostatic adsorption.[29]

5.3.4 Etching of Pt(shape)/SBA-15 Catalysts

Pt(shape)/SBA-15 catalysts were synthesized and used to study the effect of HNO_3 etching on the particles. The majority of the data presented here involves Pt(octahedra)/SBA-15 catalysts with an as-prepared Ag content of 12 – 16 at % based on total metal (Table 5.1). For the Pt(cubes)/SBA-15 and Pt(cuboctahedra)/SBA-15, the Ag content is < 1 and 15 at %, respectively. The amount of platinum and silver remaining in the Pt(octahedra)/SBA-15 catalyst after etching with 0, 1, 6, 8, and 10 M HNO_3 is listed in Table 5.1, along with the amount of platinum and silver found in the Pt(cubes)/SBA-15 and Pt(cuboctahedra)/SBA-15 before and after etching with 10 M HNO_3. A Pt(no Ag)/SBA-15 and a second Pt(octahedra)/SBA-15 catalyst are included for comparison. The mol % Ag remaining in the Pt(octahedra)/SBA-15 catalysts decreased by 10 % relative to the unetched sample after a 1 M etch and 16 % after etching in 6 M HNO_3. After etching the catalyst in 8 M HNO_3, > 84 % of the Ag was removed and an increase in [HNO_3] had no apparent effect. A small amount of the silver is etched at [HNO_3] < 6 M, but significant etching of silver occurs [HNO_3] > 7 M.

There are many possibilities for the 7 M threshold for significant Ag etching. One possibility is that most of the Ag only reacts with HNO_3 through the high [HNO_3] mechanism (Equation 5.2) when bound to Pt and/or PVP. Another explanation is that HNO_3 first reacts with Pt to form a reactive species for Ag etching. In a study by Balbaud *et al.*, the reduction of HNO_3 at a Pt electrode produced NO, but not NO_2 in 4 M HNO_3, while for 8 M and 12 M HNO_3, they observed the formation of NO_2.[34] The formation of NO_2 in this study is inferred from the evolution of a yellow-orange gas during etching at high nitric acid concentrations (> 6 M), in agreement with the electrochemical studies by Balbaud. This change in the Pt-HNO_3 interaction may produce intermediates that enhance Ag etching in this system.

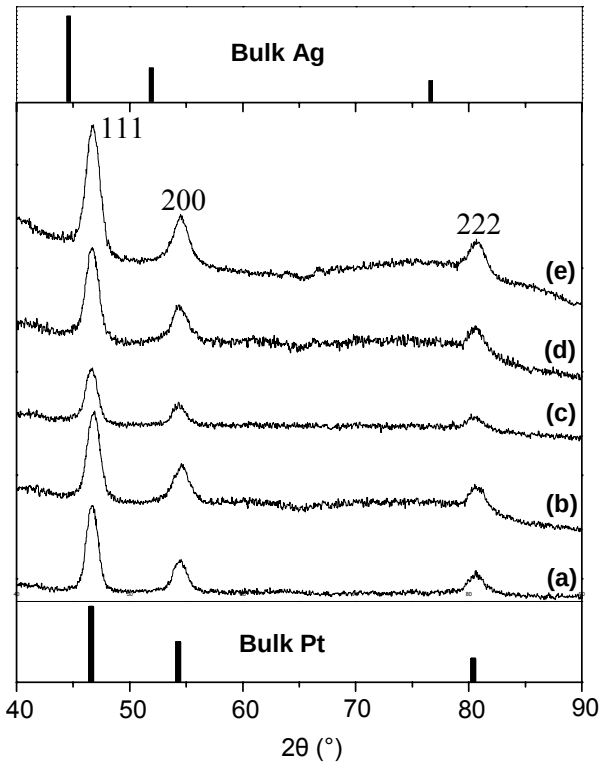

Figure 5.3. XRD patterns of Pt(octahedra)/SBA-15 (a) as-synthesized, and after etching with [HNO_3] of (b) 1 M, (c) 4 M, (d) 7 M, and (e) 15 M. The crystallite size is measured from the full width at half maximum (FWHM) of the 111 peak, which broadens slightly with increasing HNO_3 concentration.

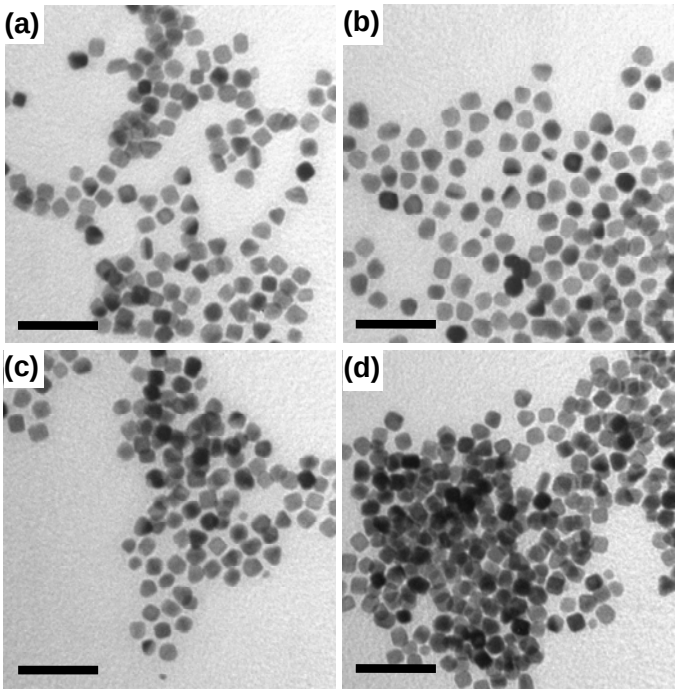

Figure 5.4. TEM images of Pt(octahedra) (a) as-synthesized, and after etching with [HNO_3] of (b) 1 M, (c) 7 M, and (d) 13 M. The etching of the nanoparticles in HNO_3 of increasing concentration led to the decomposition of the PVP-protecting layer on the surface of the nanoparticles, resulting in nanoparticle aggregation. At a concentration of 13 M, the particles completely precipitate out of solution leaving a clear supernatant.

Etching in nitric acid does not result in aggregation of the NPs supported on SBA-15 or the destruction of the SBA-15 structure (Figures 5.1 and 5.2). The Pt crystallite size decreases by ~ 20 % after etching with 15 M HNO_3 (Figure 5.3), although loss of Pt is ruled out from ICP-OES analysis (Table 5.1). The XRD particle size (calculated using the Scherrer equation) for the unetched Pt(octahedra)/SBA-15 catalyst was 9.3 nm which decreased to 9.0 nm, 8.5 nm, 8.6 nm, and 8.1 nm after etching with 1 M, 4 M, 7 M, and 15 M nitric acid, respectively. The largest change in crystallite size (1.2 nm) corresponds to a ~ 6 Å shell, or ~ 3 atomic layers. XRD provides no insight into the origin of the crystallite size decrease, but possibilities include surface Ag etching or the formation of a shell of Pt carbonyls, Pt cyanates (section 3.7), or Pt oxide. The formation of a Pt

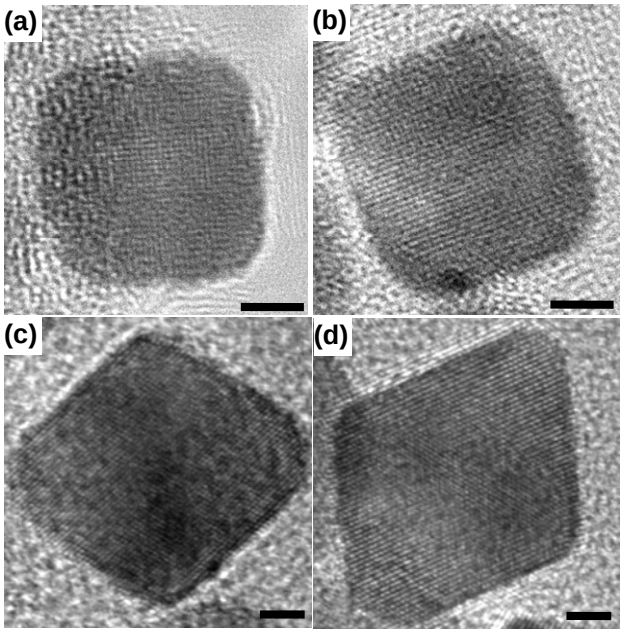

Figure 5.5. HRTEM images of Pt(cubes) (a) before etching and (b) after a 10 M etch and Pt(octahedra) (c) before etching and (d) after a 10 M etch. Scale bars are 2 nm.

compound on the surface of the NPs would not affect the total Pt content (confirmed by ICP-OES), but would decrease the effective crystallite size for diffraction.

5.3.5 Etching of Unsupported Pt Nanoparticles

A similar etching procedure was conducted on unsupported Pt NPs. The NPs, after thorough washing in ethanol and precipitation in hexanes, were dispersed in water and the appropriate amount of concentrated nitric acid was added. During etching, orange discoloration of the cap and sides of the scintillation vial was observed for $[HNO_3] > 6$ M, indicating the formation of NO_2 during the etching procedure.

TEM indicated no change in particle shape or size, but the NPs aggregrated (Figure 5.4). Aggregation was also apparent by eye: for samples etched with $[HNO_3] \leq 4$ M, the NP sol remained homogeneous in color, while a dark brown precipitate formed after a 10 M etch, and etching with 13 M HNO_3 caused complete precipitation. This aggregation probably results from degradation of PVP, which prevents particle

agglomeration.[35] Figure 5.5 shows HRTEM images of the as-synthesized platinum cubes and octahedra, and after etching with 10 M nitric acid. There does not appear to be any significant structural change of the cubic or octahedral NPs. This post-synthetic etching step provides a method to synthesize Pt NPs with well-defined surface structure from NPs synthesized in the presence of sacrificial metal ions. This method should be suitable for any Pt-metal (M) system, in which an etchant selectively etches M over Pt.

5.3.6 Diffuse Reflectance Infrared Study of CO Adsorption on Pt(shape)/SBA-15 Catalysts

Figure 5.6 shows the spectra recorded for a Pt(octahedra)/SBA-15 catalyst. A peak at 2084 cm^{-1} is present for samples etched in 4 M or 15 M HNO_3, but is absent for

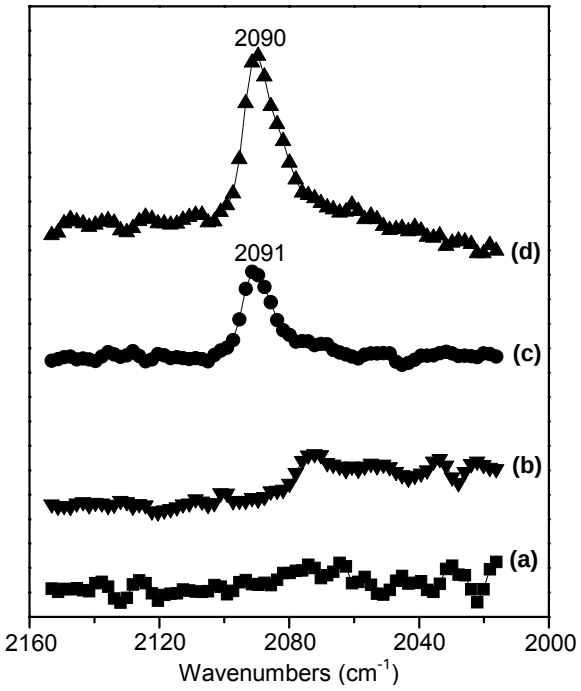

Figure 5.6. DRIFTS spectra of adsorbed CO at 300 K on Pt(octahedra)/SBA-15 (a) as-synthesized, and after etching with [HNO_3] of (b) 1 M, (c) 4 M, and (d) 15 M. CO adsorption on Pt is not observed until [HNO_3] is ~ 4 M, and the intensity of atop-bound CO increases with etching at higher [HNO_3]. A peak position of 2090 cm^{-1} is in good agreement with a Pt(100) single-crystal[1] and a calcined-reduced Pt(no Ag)/SBA-15 catalyst with a particle size of 7.1 nm.[3]

the unetched catalyst and the catalyst etched in 1 M HNO_3. This peak is indicative of atop-bonded CO on platinum[3,36] and was not observed on metal-free SBA-15 or in the samples with high Ag content. Silver appears to block the adsorption of CO either by physical site blocking, altering the electronic structure of the Pt surface, or both.

5.3.7 Attenuated Total Reflection Infrared Spectroscopy of Unsupported Pt NPs

The etching process was investigated using ATR-FTIR of unsupported Pt(No Ag), Pt(cubes), Pt(cuboctahedra), and pure PVP (Figure 5.7). There are five peaks of interest in the infrared spectra. The peak at ~ 1655 cm^{-1} is consistent with the carbonyl stretch of the PVP side chain and is the only C=O type stretch observed in pure PVP (Figure 5.7, IV(a)). A lower energy peak at 1560 – 1600 cm^{-1} grows in with HNO_3 etching both in the case of pure PVP and the PVP-protected Pt particles. This peak has previously been assigned to the C=N stretch of the PVP side chain after exposure to sulfuric acid.[37] Under these conditions, the N is protonated and the carbonyl hydrogenates to the alcohol. The peaks at ~ 2030 cm^{-1}, and ~ 1815 cm^{-1} are consistent with atop- and bridge-bonded CO on Pt, respectively.[1] Both peaks are red-shifted compared to CO bound to a clean platinum surface or to Pt NP electrodes.[38] It is possible that CO is formed as a by-product of partial PVP decomposition and remains adsorbed on the Pt surface under etching conditions. Bands at these stretching frequencies are not observed when pure PVP is treated with nitric acid (Figure 5.7, IV). To confirm that CO binds and remains on the Pt NP surface in solution, CO gas was bubbled through the Pt NP solution (before and after etching) and the adsorption of CO was followed by ATR-FTIR. Peaks were observed at 2020 – 2060 cm^{-1} for all samples, confirming that atop-

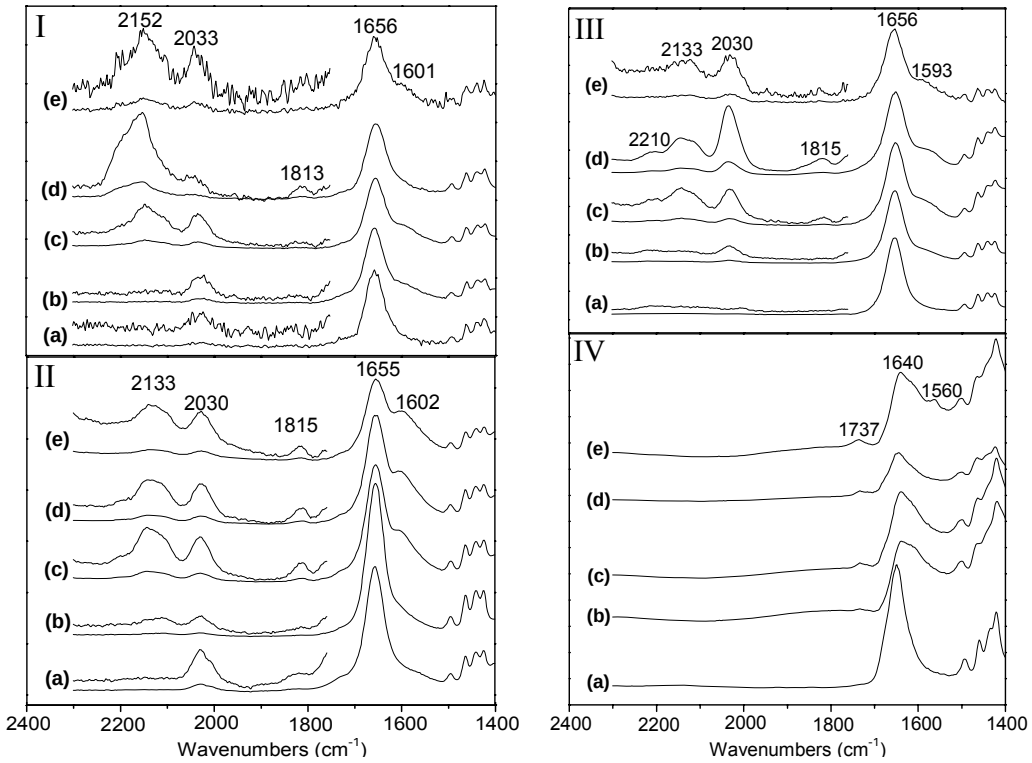

Figure 5.7. ATR-FTIR spectra of (I) Pt(no Ag), (II) Pt(cubes), (III) Pt(cuboctahedra) and (IV) pure PVP (a) as synthesized, and after etching with [HNO_3] of (b) 1 M, (c) 6 M, (d) 7 M, and (e) 15 M. Insets (1700 – 2300 cm^{-1}) are 5× magnification.

bound CO does form on the NPs in solution and is stable enough to remain on the surface throughout the duration of the experiment (Figure 5.8).

The peak observed at ~ 2130 - 2150 cm^{-1} may also be a product of the decomposition of PVP by HNO_3 that subsequently adsorbs to the Pt surface. Previous infrared studies of Pt catalysts indicate possible species: during the reaction between NO and CO on supported Pt catalysts, peaks at 2130 – 2150 cm^{-1} were attributed to surface intermediates.[39] In the case of a Pt/SiO_2 catalyst, a peak at 2142 cm^{-1} was assigned to either a platinum fulminate (Pt-CNO), cyanate (Pt-OCN), or isocyanate (Pt-NCO).[39] In a study by Unland et al. with Pt/Al_2O_3, a peak at 2130 cm^{-1} was attributed to cyanate ions while a peak at 2261 cm^{-1} was assigned to covalently-bound isocyanate.[40] Similarly, in the case of the reaction between NO_2 and propene over Pt/Al_2O_3, strong peaks at 2254

cm^{-1} and 2232 cm^{-1} were assigned to bound isocyanate, consistent with Unland's analysis, while a third resonance at 2141 cm^{-1} was assigned to the C-N stretch of surface cyanide (Pt-CN)[41]. The presence of these peaks suggests the decomposition of PVP occurs with the concurrent formation of surface-bound decomposition products. These peaks do not appear in the spectrum of pure PVP treated with HNO_3, confirming that these peaks originate from species bound to the Pt NP surface.

CO bound to Ag or Ag^+ has been ruled out based on the similarity between ATR-FTIR spectra of NPs synthesized with and without Ag (Figure 5.7). The gas-phase stretching frequency for CO bound to polycrystalline Ag and large Ag_n clusters (n > 280) appears at 2110 cm^{-1}, shifting to lower wavenumbers with decreasing particle size (The

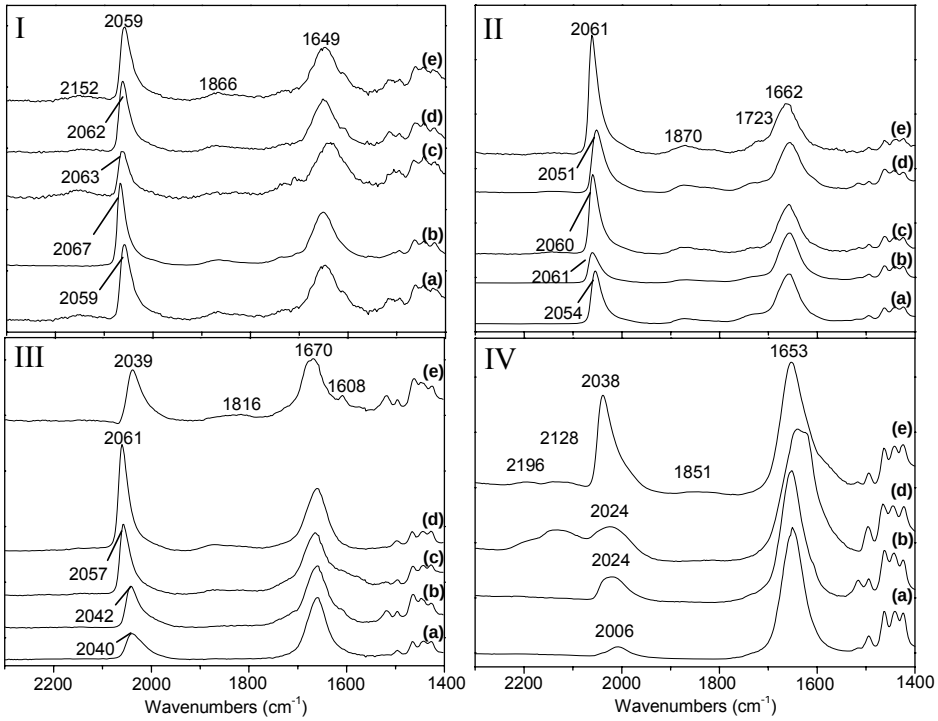

Figure 5.8: Infrared (FTIR-ATR) spectra of (I) Pt(no Ag), (II) Pt(cube), and (III) Pt(cuboctahedra) and (IV) Pt(octahedra) (a) as synthesized, and after etching with [HNO_3] of (b) 1 M, (c) 6 M, (d) 7 M, and (e) 15 M, followed by H_2 flow for 20 min at 323 K and then CO flow for 20 min at 293.

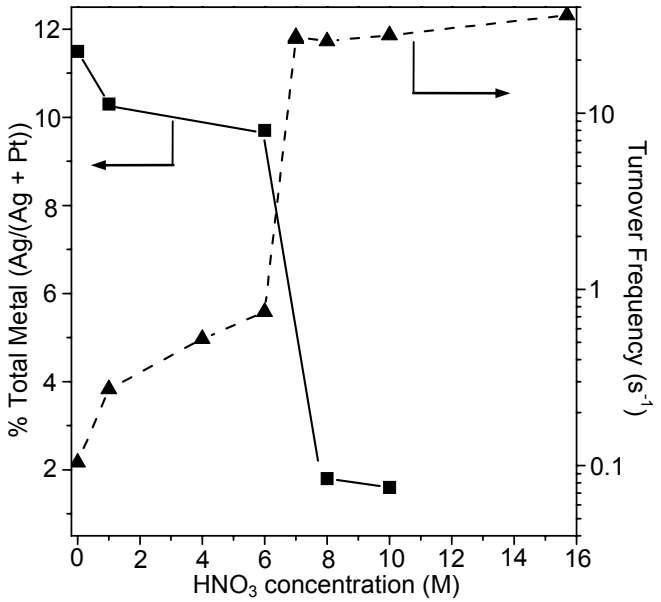

Figure 5.9. TOF for ethylene hydrogenation (10 Torr ethylene and 200 Torr hydrogen in balance He) and silver content for Pt(octahedra)/SBA-15 after various HNO_3 etching treatments. The etching of Ag and the rate of ethylene hydrogenation are enhanced dramatically when [HNO_3] > 7 M.

CO stretching frequency for Ag_{30} clusters is 2080 cm^{-1}).[42] The frequency for CO weakly-bound to Ag^+ cations on SiO_2 is 2169 cm^{-1}, and it desorbs with room temperature evacuation.[43]

5.3.8 Ethylene Hydrogenation of Unetched and Etched Pt(shape)/SBA-15

Under the reaction conditions used in this study (10 Torr C_2H_4, 200 Torr H_2, 300 K), the TOF is ~ 20-30 s^{-1} on supported Pt(no Ag) catalysts, Pt single crystals[33], and other model Pt catalysts,[3,44] but is poisoned by the presence of silver on the surface of the shape-controlled Pt NPs[2]. For this reason, ethylene hydrogenation was used as a probe for Ag etching by HNO_3. In Table 5.1 and Figures 5.9 and 5.10, the TOF is determined by normalizing the reaction rate to the estimated number of surface Pt atoms (assuming a Pt surface density of 1.25 x 10^{19} atoms/m^2) and the particle size determined by counting 100 particles from a TEM image. The size determined by XRD is in good agreement

with mean values from TEM particle size histograms. This TOF, or "rate per surface Pt atom," should be a good measure of the influence of Ag on the surface properties of the Pt NPs. Figure 5.9 shows the TOF (log scale) and Ag content for a Pt(octahedra)/SBA-15 catalyst etched in nitric acid solutions (0-15.7 M). Ag is etched efficiently from the Pt NPs when $[HNO_3] > 7$ M and the rate of ethylene hydrogenation responds favorably to the decrease in Ag content. As $[HNO_3]$ is increased above 7 M, there is very little change in [13] and therefore, little change in the TOF for ethylene hydrogenation, having TOFs similar to that of Pt(No Ag)/SBA-15 even with the presence of residual Ag.

Multiple samples of Pt(octahedra)/SBA-15, Pt(cuboctahedra)/SBA-15, Pt(cubes)/SBA-15, and Pt(no Ag)/SBA-15 were etched in various concentrations of HNO_3 in order to further understand the relationship between the Ag content and the corresponding activity for ethylene hydrogenation. Selected results are summarized in the final column of Table 5.1 and this data is presented in Figure 5.10 together with data from ref. 2 in a plot of TOF/TOF_{MAX} vs. $[Ag]/[Pt_s]$, where TOF_{MAX} (34 s^{-1}) is the TOF measured for a Pt(no Ag)/SBA-15 catalyst and Pt_s is the estimated number of surface atoms from TEM measurements. The TOF depends exponentially on the Ag/Pt_s ratio (Equation 5.3). Ag is inactive for ethylene hydrogenation at these temperatures, and one possibility for the decreased activity is that Ag resides on the surface of the Pt NPs and effectively blocks the Pt sites. In this case, the dependence of the rate on [Ag] should be linear, but instead an exponential dependence is observed:

$$\frac{TOF}{TOF_{MAX}} = 0.88 \exp\left(-6.15 \times \left(\frac{[Ag]}{[Pt_s]}\right)\right) \qquad (5.3)$$

This suggests that an electronic perturbation by Ag is responsible for the decreased activity of Pt for ethylene hydrogenation. This has been observed previously for Pt-Ag

bimetallic catalysts in the hydrogenation of 1-hexene.[45] In that work, however, Pt-Ag alloy particles were shown to form, and the activity for 1-hexene hydrogenation correlated well with the lattice parameter of the alloy.

It is possible that Ag forms a surface alloy with Pt, but a bulk alloy has been ruled out by high-resolution XRD.[32] The bulk phase diagram for Pt-Ag indicates that alloying does not occur at low temperatures (< 1100 K)[46]. Röder *et al.* found that when Ag is deposited on Pt(111) at room temperature, Ag is confined to the surface, but when Ag is deposited at 620 K (or the surface is annealed at 620 K after room temperature deposition), it forms a 2-dimensional alloy,[47] the layer of Pt-Ag mixing is a single atom thick. The near-surface segregation of Ag on Pt(111) has also been demonstrated in a

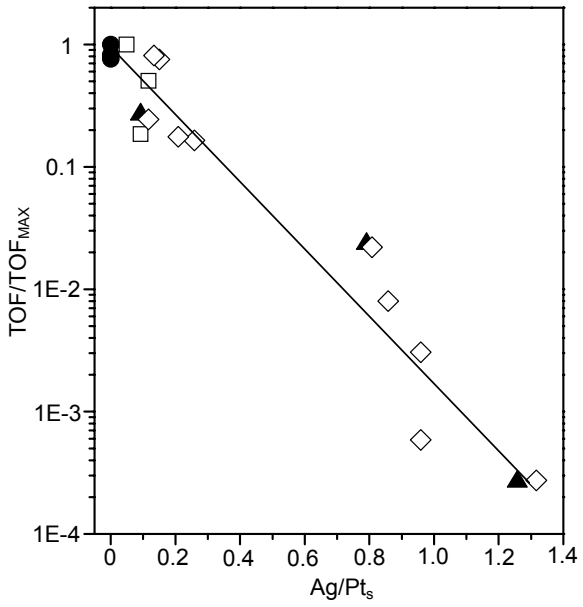

Figure 5.10. Initial TOF for ethylene hydrogenation (10 Torr ethylene, 200 Torr hydrogen in balance He) for Pt(No Ag)/SBA-15 (●), Pt(cubes)/SBA-15 (□), Pt(cuboctahedra)/SBA-15 (▲), and Pt(octahedra)/SBA-15 (◇) as a fraction of the TOF for a Pt(No Ag)/SBA-15 catalyst ($^{TOF}/_{TOF_{MAX}} = {}^{TOF}/_{TOF_{Pt(No\ Ag)/SBA\text{-}15}} = {}^{TOF}/_{34\ s^{-1}}$) before and after HNO_3 etching with [HNO_3]. The TOF ratio is plotted versus the ratio of total Ag atoms to surface Pt atoms (Pt_s). The TOF ratio is plotted versus the ratio of total Ag atoms to surface Pt atoms (Pt_s). Three points in this graph are taken from earlier work.[2]

theoretical study.[48] The picture of alloying between Pt and Ag at the nanoscale is not clear, and studies show that alloying in bimetallic systems can change with particle size.[49] In two separate extended X-ray absorption fine structure (EXAFS) studies, no alloying was observed for a Pt-Ag catalyst for particle sizes down to 2 nm.[50,51] Pt-Ag bimetallic NPs can form as Pt(core)/Ag(shell)[52] or Ag(core)/Pt(shell)[53] as indicated by UV-Vis spectroscopy and modeling with Mie theory. On the other hand, alloying in Pt-Ag bimetallic NPs has been confirmed by XRD[45] and in another study by a combination of XRD, HRTEM, and UV-Vis spectroscopy.[54] In each of these studies, the synthetic conditions were different and thus it is difficult to draw general conclusions about alloying in Pt-Ag nanoscale systems. In this work, we have ruled out a bulk alloy or solid solution[32] and believe Ag is likely isolated to the surface of the NPs as small clusters or isolated atomic species.

Another explanation for the decrease in TOF is decreased electron density in the Pt 5d orbital due to a Pt(5d) → Ag charge transfer. This charge transfer was proposed in the case of Ag overlayers on Pt(111) where no alloying occurred[55]. While this system has not been explicitly studied, the effect of transition metals on the d-band structure of Pt and its importance for catalysis has been elucidated with density functional theory.[56]

It is worthwhile to note that all samples fit the exponential dependence of TOF vs. Ag/Pt_s despite the different etching concentrations used to achieve the same Ag content, indicating that the observed effect is dominated by Ag content rather than an ancillary effect of HNO_3 etching. The TOF of a Pt(no Ag)/SBA-15 catalyst was unaffected by HNO_3 etching (Table 5.1). The etched Pt(shape)/SBA-15 catalysts hydrogenate ethylene at the same rate as Pt(no Ag), demonstrating that nitric acid etching can effectively

remove Ag to produce nearly pure Pt NPs. As a reference, a Pt/SiO_2 catalyst (~ 9 nm particle size) was prepared by electrostatic adsorption[30] and examined under identical reaction conditions. The TOF for this sample was calculated to be 8 s^{-1}, which is a factor of 3 lower than the most active catalysts studied in this investigation.

5.4 Conclusions

Silver can be selectively removed from shape-controlled platinum nanoparticles either before or after incorporation onto a silica support by etching with concentrated nitric acid (7 – 15 M) at 333 K. The shape – cubic, cuboctahedral, or octahedral – and size of the particles remains unchanged after etching as determined by high-resolution transmission electron microscopy. The etching of platinum nanoparticles suspended in solution leads to severe aggregation when the nitric acid concentration is greater than 10 M, due to decomposition of the stabilizing polymer, poly(vinylpyrrolidone). This decomposition leads to the formation of carbon monoxide and most likely cyanates bound to the Pt surface. Silver elemental analysis demonstrated the near-complete etching of silver from the platinum/silver nanoparticles at nitric acid concentrations greater than 7 M without loss of platinum. The activity for ethylene hydrogenation increased exponentially with decreasing $Ag:Pt_s$ ratio. The turnover frequency for a Pt(octahedra)/SBA-15 catalyst increased from 0.01 to 28 after etching with 10 M nitric acid. These results confirm that Ag used in the synthesis of shape-controlled Pt nanoparticles is confined to the surface and can be selectively removed, providing a new method for shape control of Pt nanoparticles.

5.5 References

(1) Somorjai, G. A. *Introduction to Surface Chemistry and Catalysis*; Wiley-Interscience: New York, 1994.

(2) Rioux, R. M.; Song, H.; Grass, M.; Habas, S.; Niesz, K.; Hoefelmeyer, J. D.; Yang, P.; Somorjai, G. A. *Top. Catal.* **2006**, *39*, 167.

(3) Song, H.; Rioux, R. M.; Hoefelmeyer, J. D.; Komor, R.; Niesz, K.; Grass, M.; Yang, P. D.; Somorjai, G. A. *J. Am. Chem. Soc.* **2006**, *128*, 3027.

(4) Roucoux, A.; Schulz, J.; Patin, H. *Chem. Rev.* **2002**, *102*, 3757.

(5) Rioux, R. M.; Song, H.; Hoefelmeyer, J. D.; Yang, P.; Somorjai, G. A. *J. Phys. Chem. B* **2005**, *109*, 2192.

(6) Gupta, G.; Stowell, C. A.; Patel, M. N.; Gao, X. X.; Yacaman, M. J.; Korgel, B. A.; Johnston, K. P. *Chem. Mater.* **2006**, *18*, 6239.

(7) Lee, H.; Habas, S. E.; Kweskin, S.; Butcher, D.; Somorjai, G. A.; Yang, P. D. *Angew. Chem. Int. Ed.* **2006**, *45*, 7824.

(8) Miyazaki, A.; Balint, I.; Nakano, Y. *J. Nanopart. Res.* **2003**, *5*, 69.

(9) Narayanan, R.; El-Sayed, M. A. *Nano Lett.* **2004**, *4*, 1343.

(10) Telkar, M. M.; Rode, C. V.; Chaudhari, R. V.; Joshi, S. S.; Nalawade, A. M. *Appl. Catal. A: Gen.* **2004**, *273*, 11.

(11) Tian, N.; Zhou, Z. Y.; Sun, S. G.; Ding, Y.; Wang, Z. L. *Science* **2007**, *316*, 732.

(12) Xu, R.; Wang, D. S.; Zhang, J. T.; Li, Y. D. *Chem. Asian J.* **2006**, *1*, 888.

(13) Chimentao, R. J.; Kirm, I.; Medina, F.; Rodriguez, X.; Cesteros, Y.; Salagre, P.; Sueiras, J. E.; Fierro, J. L. G. *Appl. Surf. Sci.* **2005**, *252*, 793.

(14) Ahmadi, T. S.; Wang, Z. L.; Green, T. C.; Henglein, A.; El-Sayed, M. A. *Science* **1996**, *272*, 1924.

(15) Bakshi, M. S.; Kaura, A.; Bhandari, P.; Kaur, G.; Torigoe, K.; Esumi, K. *J. Nanosci. Nanotechnol.* **2006**, *6*, 1405.

(16) Kim, F.; Connor, S.; Song, H.; Kuykendall, T.; Yang, P. D. *Angew. Chem. Int. Ed.* **2004**, *43*, 3673.

(17) Hoefelmeyer, J. D.; Niesz, K.; Somorjai, G. A.; Tilley, T. D. *Nano Lett.* **2005**, *5*, 435.

(18) Sun, J. L.; Zhang, J. H.; Liu, W.; Liu, S.; Sun, H. S.; Jiang, K. L.; Li, Q. Q.; Guo, J. H. *Nanotechnology* **2005**, *16*, 2412.

(19) Song, H.; Kim, F.; Connor, S.; Somorjai, G. A.; Yang, P. D. *J. Phys. Chem. B* **2005**, *109*, 188.

(20) Seo, D.; Park, J. C.; Song, H. *J. Am. Chem. Soc.* **2006**, *128*, 14863.

(21) Chen, J. Y.; Wiley, B.; McLellan, J.; Xiong, Y. J.; Li, Z. Y.; Xia, Y. N. *Nano Lett.* **2005**, *5*, 2058.

(22) Xu, Z. C.; Shen, C. M.; Xiao, C. W.; Yang, T. Z.; Zhang, H. R.; Li, J. Q.; Li, H. L.; Gao, H. J. *Nanotechnology* **2007**, *18*.

(23) Van Hardeveld, R.; Hartog, F. *Surf. Sci.* **1969**, *15*, 189.

(24) Martinez, L., Segarra, M., Fernandez, M., Espiell, F. *Metall. Trans. B* **1993**, *24B*, 827.

(25) Ozmetin, C., Copur, M., Yartasi, A., Kocakerim, M.M. *Chem. Eng. Technol.* **2000**, *23*, 707.

(26) Ozmetin, C., Copur, M., Yartasi, A., Kocakerim, M.M. *Ind. Eng. Chem. Res.* **1998**, *37*, 4641.

(27) Bancroft, W. D. *J. Chem. Soc.* **1924**, *28*, 973.

(28) Aqua regia is formed by freshly mixing concentrated nitric acid (15.7 M) and concentrated hydrochloric acid (12 M), usually in a volumetric ratio of one to three, respectively. The oxidation of Pt can be written with either nitric oxide or nitrogen dioxide as the nitrogen-containing product.

$$Pt(s) + 4NO_3^-(aq) + 8H^+(aq) = Pt^{4+}(aq) + 4NO_2(g) + 4H_2O(l) \quad (5.4)$$

$$3Pt(s) + 4\,NO_3^-(aq) + 16\,H^+(aq) = 3Pt^{4+}(aq) + 4NO(g) + 8H_2O(l) \quad (5.5)$$

The oxidized platinum ion then reacts with chloride ions resulting in the chloroplatinate ion removing them from solution.

$$Pt^{4+}(aq) + 6Cl^-(aq) \rightleftharpoons PtCl_6^{2-}(aq) \quad (5.6)$$

The reduction in the concentration of Pt^{4+} ions shifts the equilibria of eqn. (5.4) and (5.5) to the oxidized form. In the absence of Cl^- ions (as in the case of nitric acid only), the equilibrium constants for rxns (5.4) and (5.5) are so small that the etching of Pt doesn't occur to any appreciable extent.

(29) Lu, X. M.; Au, L.; McLellan, J.; Li, Z. Y.; Marquez, M.; Xia, Y. N. *Nano Lett.* **2007**, *7*, 1764.

(30) Miller, J. T.; Schreier, M.; Kropf, A. J.; Regalbuto, J. R. *J. Catal.* **2004**, *225*, 203.

(31) Anderson, J. R. *Structure of Metallic Catalysts*; Academic Press: London, 1975.

(32) Habas, S. E., University of California, Berkeley, 2008.

(33) Backman, A. L.; Masel, R. I. *J. Vac. Sci. Technol., A* **1988**, *6*, 1137.

(34) Balbaud, F.; Sanchez, G.; Santarini, G.; Picard, G. *Eur. J. Inorg. Chem.* **2000**, 665.

(35) Napper, D. H. *Polymeric Stabilization of Colloidal Dispersions*; Academic Press: London, 1983.

(36) Bischoff, H.; Jaeger, N. I.; Shulzekloff, G. *Z. Phys. Chem. (Leipzig)* **1990**, *271*, 1093.

(37) Schweinsberg, D. P.; Hope, G. A.; Trueman, A.; Otieno-Alego, V. *Corros. Sci.* **1996**, *38*, 587.

(38) Mayrhofer, K. J. J.; Arenz, M.; Blizanac, B. B.; Stamenkovic, V.; Ross, P. N.; Markovic, N. M. *Electrochim. Acta* **2005**, *50*, 5144.

(39) Anderson, J. A.; Rochester, C. H. *J. Chem. Soc., Faraday Trans.* **1991**, *87*, 1485.

(40) Unland, M. L. *J. Phys. Chem.* **1973**, *77*, 1952.

(41) Bamwenda, G. R.; Ogata, A.; Obuchi, A.; Oi, J.; Mizuno, K.; Skrzypek, J. *Appl. Catal. B: Environ.* **1995**, *6*, 311.

(42) Froben, F. W.; Rabin, i.; Ritz, M.; Schulze, W. *Z. Phys. D: At., Mol. Clusters* **1996**, *38*, 335.

(43) Hadjiivanov, K.; Knozinger, H. *J. Phys. Chem. B* **1998**, *102*, 10936.

(44) Contreras, A. M.; Grunes, J.; Yan, X. M.; Liddle, A.; Somorjai, G. A. *Catal. Lett.* **2005**, *100*, 115.

(45) Campostrini, R.; Giovanni, C.; Dire, S.; Scardi, P. *J. Mol. Catal.* **1989**, *53*, L13.

(46) Okamoto, H. *J. Phase Equilib. Diffus.* **1997**, *18*, 485.

(47) Roder, H.; Schuster, R.; Brune, H.; Kern, K. *Phys. Rev. Lett.* **1993**, *71*, 2086.

(48) Christensen, A.; Ruban, A. V.; Stoltze, P.; Jacobsen, K. W.; Skriver, H. L.; Norskov, J. K.; Besenbacher, F. *Phys. Rev. B* **1997**, *56*, 5822.

(49) Yasuda, H.; Mori, H. *J. Cryst. Growth* **2002**, *237*, 234.

(50) Lahiri, D.; Bunker, B.; Mishra, B.; Zhang, Z. Y.; Meisel, D.; Doudna, C. M.; Bertino, M. F.; Blum, F. D.; Tokuhiro, A. T.; Chattopadhyay, S.; Shibata, T.; Terry, J. *J. Appl. Phys.* **2005**, *97*.

(51) Doudna, C. M.; Bertino, M. F.; Blum, F. D.; Tokuhiro, A. T.; Lahiri-Dey, D.; Chattopadhyay, S.; Terry, J. *J. Phys. Chem. B* **2003**, *107*, 2966.

(52) Henglein, A. *Langmuir* **2001**, *17*, 2329.

(53) Lizmarzan, L. M.; Philipse, A. P. *J. Phys. Chem.* **1995**, *99*, 15120.

(54) Torigoe, K.; Nakajima, Y.; Esumi, K. *J. Phys. Chem.* **1993**, *97*, 8304.

(55) Rodriguez, J. A.; Kuhn, M. *J. Phys. Chem.* **1994**, *98*, 11251.

(56) Bligaard, T.; Norskov, J. K. *Electrochim. Acta* **2007**, *52*, 5512.

Chapter 6: Colloidal synthesis of size-controlled Rh nanoparticles, formation of Langmuir-Blodgett films, and reactivity for hydrogenation reactions

Size-tunable monodisperse Rh nanocrystals can offer unique properties for many heterogeneous catalytic reactions, such as hydrogenation, hydroformylation, and hydrocarbonylation, of both scientific and technological interest. Well-shaped, monodisperse Rh nanocrystals of 5-15 nm have been synthesized by a one-step polyol reduction at temperatures of 170-230 °C under Ar, using rhodium(III) acetylacetonate ($Rh(acac)_3$) as the source of metal ions, 1,4-butanediol as the reducing solvent, and poly(vinylpyrrolidone) as the capping agent. 2-D projections of the nanocrystals are polygons, dominated by hexagons, pentagons and triangles with catalytically active (111) surfaces (>65% in yield). More than 45% of the polygons are multiple (111) twinned particles (hexagons and pentagons). To achieve size uniformity, adjustment of the reduction kinetics of $Rh(acac)_3$ in the nucleation and crystal growth stages has been shown to depend upon several synthetic parameters including reaction temperature, time, and $Rh(acac)_3$ concentration. By controlling the polyol reduction kinetics, the size of the Rh nanocrystals can be tuned by changing the $Rh(acac)_3$ concentration in a proper range. Monolayer films of the Rh polygons have been formed on silicon wafers by the Langmuir-Blodgett method and used as model heterogeneous catalysts for ethylene hydrogenation.

6.1 Introduction

Noble metal nanocrystals with controlled size, shape, chemical composition, and surface structure are of fundamental and technological importance because of their unique catalytic activity and selectivity, and are employed for applications such as fine chemicals synthesis, oil refining processes, and fuel cell technology.[1-6] The ability to control shape, size, and size dispersity makes such nanocrystals ideal building blocks for constructing 2-D and 3-D model heterogeneous catalysts on various supports (e.g. silicon wafers, mesoporous oxide materials including SiO_2, Al_2O_3 and Ta_2O_5).[7, 8] Monodisperse noble metal nanocrystals have size and shape-defined fractions of surface atoms and catalytically relevant structural attributes such as exposed crystal faces and the ratio of corner, edge, and terrace atoms.[9] These properties make monodisperse nanocrystals good candidates for model catalytic studies and new catalytic technologies. Comprehensive understanding of the size and shape-dependent catalytic properties of noble metal nanocrystals (with respect to their bulk counterparts) and metal-support interactions can help to advance the development of heterogeneous catalysis theories and impact the fabrication of high performance noble metal nanocatalysts for practical applications. Certainly, the elucidation of size/shape-function relationships requires the exploration of new synthetic methods that can provide improved size/shape control in a reproducible manner.

Recently, much attention has been paid to the size/shape control of noble metal nanocrystals (Rh,[10-13] Ir,[14] Pd,[15] Pt,[1, 16-18] Ag,[19, 20], Au[21, 22]) by tuning the crystal growth kinetics in solution-phase syntheses, including seeded growth by polyol reduction,[10, 11] modified polyol methods,[1, 13, 23] thermolysis of organometallics,[12, 14] and micelle

techniques.[17, 19, 22] As one of the most important noble metals, Rh nanocatalysts are used in a wide range of heterogeneous reactions such as hydrogenation, hydroformylation, and hydrocarbonylation.[12, 24, 25] Size and shape control of Rh nanocrystals has thus become an important research focus. For example, the Somorjai and Tilley groups have reported the size and shape control of Rh nanocrystals (multipods, cubes, horns and cuboctahedra) by seeded growth in a polyol system.[10, 11] Xia and his colleagues investigated the polyol synthesis and stability of Rh multipods, which show interesting surface plasmonic properties.[13] By a non-hydrolytic organometallic approach, Son and coworkers prepared monodisperse oleylamine-capped Rh tetrahedral nanocrystals, which display excellent hydrogenation activity with a range of arenes.[12] However, there has been little work on the size control of monodisperse Rh nanocrystals over a wide range, or the synthesis of multiple (111) twinned Rh particles, prior to this study.

A one-step polyol synthesis of monodisperse, well-shaped Rh nanocrystals in the size range 5-15 nm at temperatures of 170-230 °C using rhodium(III) acetylacetonate ($Rh(acac)_3$) as the source of metal ions, 1,4-butanediol as the reducing solvent, and poly(vinylpyrrolidone) (PVP) as the capping agent is presented here. The nanocrystals are composed of hexagons, pentagons and triangles with (111) surfaces. The hexagons and pentagons have been identified as multiple (111) twinned particles. The mechanism of the polyol synthesis of the Rh nanocrystals is discussed by considering the $Rh(acac)_3$ reduction kinetics in the nucleation and crystal growth stages. Additionally, a Langmuir-Blodgett (LB) trough was used to fabricate monolayer films of the size-tunable Rh nanocrystals on Si wafers as model 2-D catalysts. Catalytic results of ethylene

hydrogenation over the PVP-capped Rh nanocrystal LB films confirm that the samples are active catalysts for hydrogenation reactions.

6.2 Experimental

6.2.1 Chemicals

Rhodium(III) acetylacetonate ($Rh(acac)_3$, 97%), 1,4-butanediol (99%; b.p. 230 °C), poly(vinylpyrrolidone) (PVP, *M*w = 55,000), acetylacetone (Hacac, ≥99%) were purchased from Sigma-Aldrich. All the solvents, including acetone, ethanol, hexane and chloroform, were of analytical grade, and were used without further purification.

6.2.2 Synthesis of Rh Nanocrystals

A given amount of $Rh(acac)_3$ (1.25-200 mg, 0.313-5 × 10^{-4} mol) and PVP (3.47-555 mg, 0.313-5×10^{-3} mol in terms of the repeating unit) at a fixed Rh/PVP ratio of 1:10, were added to 20 ml of 1,4-butanediol in a 50 ml three-necked flask at room temperature. The stock solution was heated to 140 °C in a Glas-Col electromantle (60 W; 50 ml) with a Cole-Parmer temperature controller (Diqi-sense®), and was evacuated at this temperature for 20 min to remove water and oxygen under magnetic stirring, resulting in an optically transparent orange-yellow solution. The flask was then heated to the desired reaction temperature, between 170 and 230 °C, at a rate of 10 °C min^{-1}, and maintained at this temperature (±2 ^{o}C) for 2 h under Ar. During the reaction, the color of the solution gradually turned from orange-yellow to black. When the reaction was complete, an excess of acetone was poured into the solution at room temperature to form a cloudy black suspension. This suspension was separated by centrifugation at 4200 rpm for 6

min, and the black product was collected by discarding the colorless supernatant. The precipitated Rh nanocrystals were washed with acetone once then re-dispersed in ethanol.

6.2.3 Fabrication of Langmuir-Blodgett (LB) Films

The Rh nanocrystals were washed several times by precipitation/dissolution in ethanol and then in chloroform (1 ml of Rh dispersion was precipitated by adding 4 ml of hexane, and re-dispersed in 1 ml of ethanol or chloroform with sonication), to remove the impurities and excess PVP. Monolayers of Rh nanocrystals were formed by placing drops of Rh nanocrystal chloroform solution onto the water subphase of a LB trough (Nima Technology, M611) at room temperature.[18] The surface pressure was monitored with a Wilhelmy plate that was adjusted to zero before spreading the nanocrystals. The resulting surface layer was compressed by moving the mobile barrier at a rate of 15 cm^2 min^{-1}. At different stages of compression, the Rh layers at the water-air interface were carefully transferred onto continuous carbon-coated copper grids using the Langmuir-Schäffer horizontal liftoff method. The surface coverage was evaluated by counting the particles on the same area of the copper grid. The Rh nanocrystals were deposited onto Si wafers (1 cm × 1 cm) by lift-up of the substrates at a rate of 1 mm min^{-1}.

6.2.4 Characterization Methods

The shape, size and lattice structure of the Rh nanocrystals were analyzed using a Philips FEI Tecnai 12 Transmission electron microscope (TEM) and Philips CM200/FEG high-resolution TEM (HRTEM), operated at 100 and 200 kV, respectively. The samples were prepared by placing a drop of a Rh nanocrystal sol in ethanol onto a continuous carbon-coated copper TEM grid. Powder X-ray diffraction (XRD) patterns were recorded on a Bruker D8 GADDS diffractometer using Co-K_α radiation (λ = 1.79 Å). All

UV-vis absorption spectra were measured on an Agilent 8453 UV-visible ChemStation equipped with a 1 cm path length quartz cuvette, with the samples prepared by diluting 0.1 ml of reaction solution (aspirated directly from the reaction system with a 1 ml plastic syringe) with 5 ml absolute ethanol. XPS experiments were performed on a Perkin-Elmer PHI 5300 XPS spectrometer with a position-sensitive detector and a hemispherical energy analyzer in an ion-pumped chamber (evacuated to 2×10^{-9} Torr). The Al-Kα (*BE* = 1486.6 eV) X-ray source of the XPS spectrometer was operated at 300 W with 15 kV acceleration voltage. The binding energy (*BE*) for the samples was calibrated by setting the measured *BE* of C 1s to 285 eV. The elemental ratio was calculated from the integrated peak areas of the Rh 3*d* and O 1*s* core levels, showing a deviation of around 10%.

6.2.5 Ethylene Hydrogenation

Catalytic reactions were studied in a Pyrex reactor connected to a ¼" stainless steel manifold containing mass flow controllers (Unit Instruments) for delivery of reactant gases. Ethylene (AirGas, CP grade), hydrogen (Praxair, UHP, 99.999%) and helium (Praxair, UHP, 99.999%) were used as received. The catalyst was mounted on a stainless steel cell with an o-ring seal and a Kapton heater mounted to the back of the sample (22.5 mm^2 in area). The temperature was measured by a thermocouple in contact with the front of the sample. Reactants and products were detected by gas chromatography (Hewlett Packard 5890) and quantified using Dietz tables.[26] Reaction rate measurements were conducted at differential conditions (all conversions, X < 10%). Prior to each catalytic test, the sample was pretreated first by heating to 90 °C in vacuum, then by reducing in 200 Torr H_2 using He as a makeup gas at 90 °C. All measurements were taken at 200

Torr H_2 and 20 Torr ethylene. The turnover frequency (TOF) was calculated from the surface coverage and sample size by assuming that the Rh nanocrystals were spherical and non-overlapping.

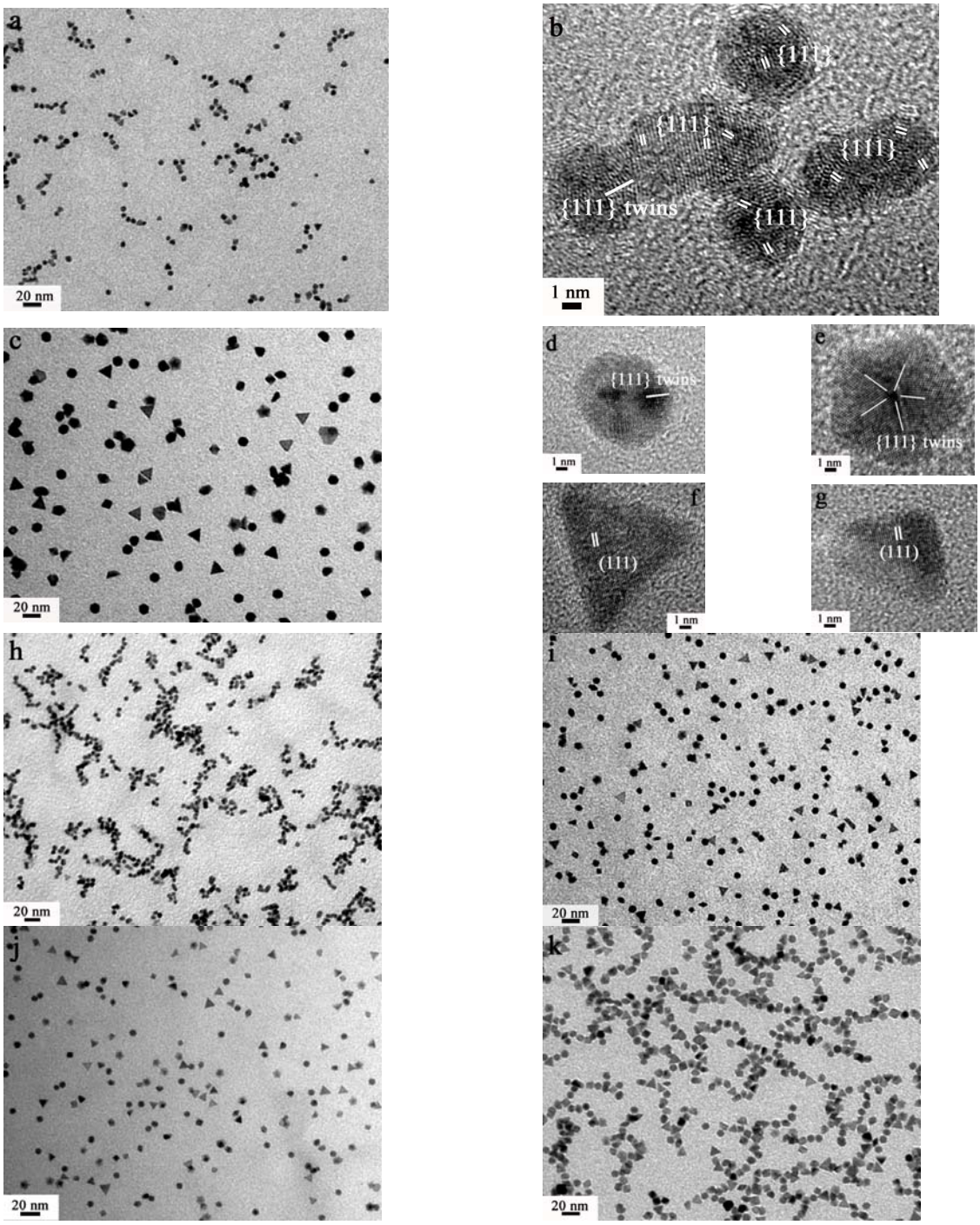

Figure 6.1. (a) TEM and (b) HRTEM images of 6.5 nm Rh nanocrystals. (c) TEM and (d-g) HRTEM images of 13.5 nm Rh nanocrystals. TEM images of (h) 5.4, (i) 7.7, (j) 8.3, and (k) 9.3 nm Rh nanocrystals.

6.3 Results and Discussion

6.3.1 Size, Shape and Surface Structure

Monodisperse Rh nanocrystals in the size range of 5-15 nm were prepared by polyol reduction (Table 6.1, Figure 6.1). TEM measurements indicate that the Rh nanocrystals have various polygonal shapes with 2D projections including hexagons, pentagons, triangles, squares, and rhombohedra, among which the former three dominate. 6.5 nm Rh nanocrystals are mainly composed of hexagons (Figure 6.1a) with a yield of 74%. HRTEM analyses reveal that the nanocrystals have (111) surface structures (interplanar distance: 0.21 nm), with {111} twins (Figure 6.1b). In addition, the nanocrystals exhibit significant lattice distortions, indicating that they are highly-strained, possibly due to the existence of a high density of defects on their surfaces.[27, 28] Figure 1c shows that the 13.5 nm Rh nanocrystals are comprised of 36% hexagons, 26% pentagons, and 17% triangles (Table 6.1). The hexagons and pentagons appear to have {111} twin planes (Figure 6.1d,e), while the triangles (probably tetrahedral in 3D) and imperfect triangles are both single-crystalline with exposed (111) facets (Figure 6.1f,g). The presence of a 5-fold symmetry axis in the HRTEM images of the pentagons indicates that they are multiple twinned particles (MTPs) such as decahedra. Moreover, the clear lattice fringes observed from the HRTEM images (Figure 6.1b,d-g) confirm that as-synthesized Rh nanocrystals are highly crystalline.

The yields of hexagons, pentagons and triangles are listed in Table 6.1. 6.4 nm Rh nanocrystals are made up of > 95% hexagons (Figure 6.1h), while the 7.7 nm nanocrystals contain 38% hexagons, 20% pentagons and 14% triangles (Figure 6.1i). The

8.3 nm nanocrystals contain 33% hexagons, 22% pentagons, and 22% triangles (Figure 6.1j), while 9.3 nm nanocrystals are composed of 33% hexagons, 15% pentagons, and 18% triangles (Figure 6.1k). The total yield of the hexagons, pentagons and triangles for all Rh nanocrystals is greater than 65%.

Line broadening observed in the x-ray diffractograms indicates that all of the samples are nanocrystalline (Figure 6.2). Three well-resolved diffraction peaks at 49.2°, 57.4° and 85.0° in 2θ value are ascribed to the (111), (200) and (220) crystal planes of face-centered-cubic (*fcc*) Rh metal (JCPDS No. 5-685). As listed in Table 6.1, the ratios of $I_{(111)}/I_{(200)}$ for the Rh polygons described here are in the range of 3.62-12.5, which are significantly higher than 1.82 for 12.7 nm Rh cubes (enclosed by six (100) facets),[11] and 3.1 for 4.87 nm Rh cuboctahedra (enclosed by six (100) facets and eight (111) facets).[10] This result strongly suggests that the Rh nanocrystals are dominated by (111) surface structures, consistent with HRTEM results.

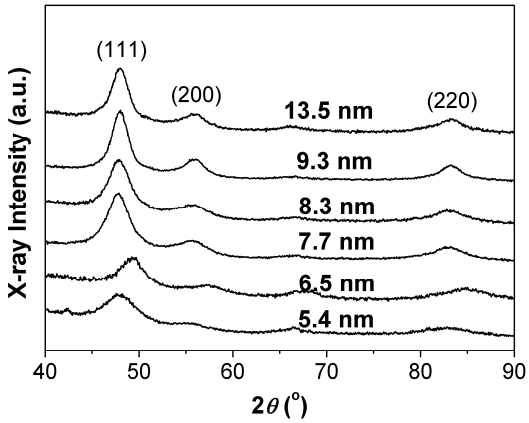

Figure 6.2. XRD patterns of as-synthesized Rh nanocrystals.

Table 6.1. Shape, Size, and $I_{(111)}/I_{(200)}$ Ratio of Monodisperse Rh Nanocrystals Synthesized in 1,4-Butanediol under Ar

Entry	$Rh(acac)_3$ (mM)	PVP (mM)	T (^oC)	t (h)	Shape (yield%); Number of counting	Size (nm)	$I_{(111)}/I_{(200)}$
1	0.313	3.13	225	2	Hexagon (>95%); 150	5.4 ± 0.5[a]	10.8
2	0.625	6.25	225	2	Hexagon (74%) and triangle (15%); 141	6.5 ± 0.5	12.5
3	1.25	12.5	225	2	Hexagon (39%), pentagon (16%) and triangle (14%); 278	7.1 ± 0.5	11.0
4	1.25	12.5	195	2	Hexagon (38%), pentagon (20%) and triangles (14%); 126	7.7 ± 0.7	4.71
5	1.25	12.5	205	2	Hexagon (33%), pentagon (22%) and triangle (22%); 162	8.3 ± 0.7	4.78
6	2.5	25	225	2	Hexagon (33%), pentagon (15%) and triangle (18%); 251	9.3 ± 0.8	3.69
7	5	50	225	2	Hexagon (36%), pentagon (22%) and triangle (12%); 174	10.7 ± 0.9	3.62
8	5	50	205	2	Hexagon (36%), pentagon (26%) and triangle (17%); 178	13.5 ± 1.4	4.22

[a] The standard deviation statistic from 150 nanocrystals.

6.3.2 Formation Conditions of Rh Nanocrystals

Alcohol reduction has been developed as a general approach for the synthesis of colloidal metal nanoparticles since the 1990s.[1, 5, 10, 11, 15, 18, 20, 21, 29] Size and shape control by this method is known to be governed by several factors, such as the reduction kinetics of a metal precursor by an alcohol (related to the intrinsic physical and chemical behaviors of a noble metal and its precursor compound, and the reducing power of an alcohol), the crystal growth regime (kinetic or thermodynamic), the coordinating ability of the capping agent, and the chemical environment inside the reaction media (oxidative or inert). In the present work, a set of condition-dependent experiments were carefully carried out to reveal the effects of various synthetic parameters on the Rh nanocrystal

characteristics (such as size distribution and shape). Reaction temperature, time, and the $Rh(acac)_3$ concentration have been demonstrated to be crucial factors responsible for the formation of monodisperse Rh nanocrystals with well-defined shapes.

6.3.3 Effect of Reaction Time

We conducted a TEM investigation of Rh nanocrystal crystal growth with time at 215 °C under Ar ([$Rh(acac)_3$] = 12.5 mM). As the temperature was increased from 140 to 195 °C in 5 min, the color of the solution gradually turned from orange-yellow to dark brown, indicating the formation of Rh nanocrystals as the $Rh(acac)_3$ was reduced by 1,4-butanediol. The Rh product consisted of small particles (~4 nm) and large polygons (~15 nm), indicating instant nucleation and subsequent rapid crystal growth (68% of nanocrystals smaller than 10 nm; Figure 6.3a). As the temperature subsequently rose to 215 °C in another 5 min, 11 nm Rh nanocrystals (34% of nanocrystals smaller than 10 nm) with undefined shapes were formed (Figure 6.3b). After 15 min of reaction at 215 °C, the Rh nanocrystals rapidly grew to 15.9 nm (7.3% of nanocrystals smaller than 10 nm) as the smaller crystals were consumed. Meanwhile, the nanocrystals developed highly faceted edges (Figures 6.3c). After 30 min, the nanocrystals were 16.1 nm (4.7% of nanocrystals smaller than 10 nm). At 45 min, the Rh nanocrystals enlarged to 16.6 nm at the complete expense of the small particles (2.1% of nanocrystals smaller than 10 nm; Figures 6.3d). At longer reaction times of 90, 120, and 180 min, the Rh nanocrystals showed no obvious changes in size, size distribution, or shape. Therefore, it is assumed that Ostwald ripening took place in 45 min during the growth of Rh nanocrystals. [9a]

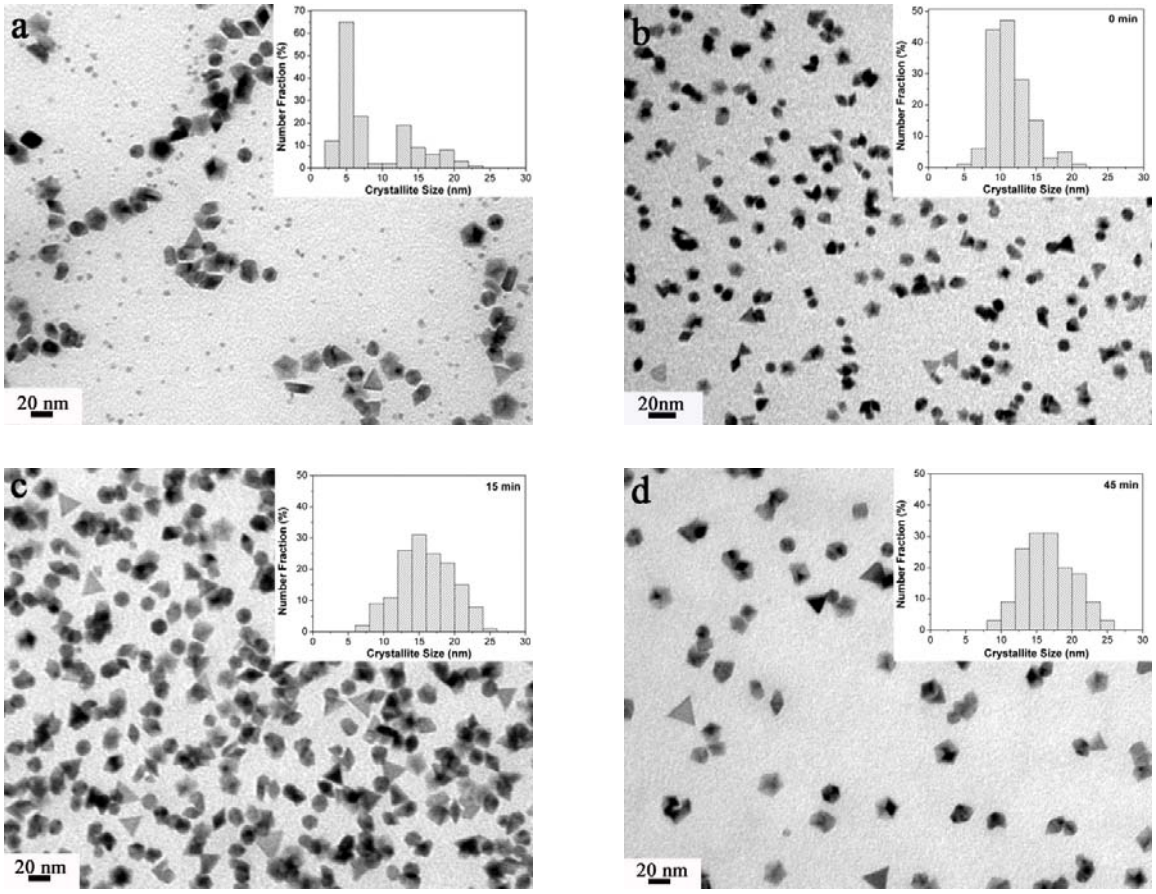

Figure 6.3. (a) TEM image of the Rh product collected at 195 °C as the temperature was elevated from 140 to 215 °C under Ar ([$Rh(acac)_3$] = 12.5 mM). TEM images of Rh nanocrystals synthesized at 215 °C for different periods of times under Ar ([$Rh(acac)_3$] = 12.5 mM): (b) 0 min; (c) 15 min; (d) 45 min. (Inset: size distribution histogram from 150 Rh nanocrystals).

6.3.4 Effect of Reaction Temperature

$Rh(acac)_3$ can be reduced to Rh(0) by 1,4-butanediol at temperatures above 170 °C under Ar. Panels a-c of Figure 6.4 show TEM images of Rh nanocrystals synthesized at different temperatures for 2 h under Ar ([$Rh(acac)_3$] = 5 mM). Below 195 °C, the Rh nanocrystals are polydisperse and not well-shaped (Figure 6.4a,b). The nanocrystals formed at this temperature are mainly twinned particles, favored by thermodynamics,[15]

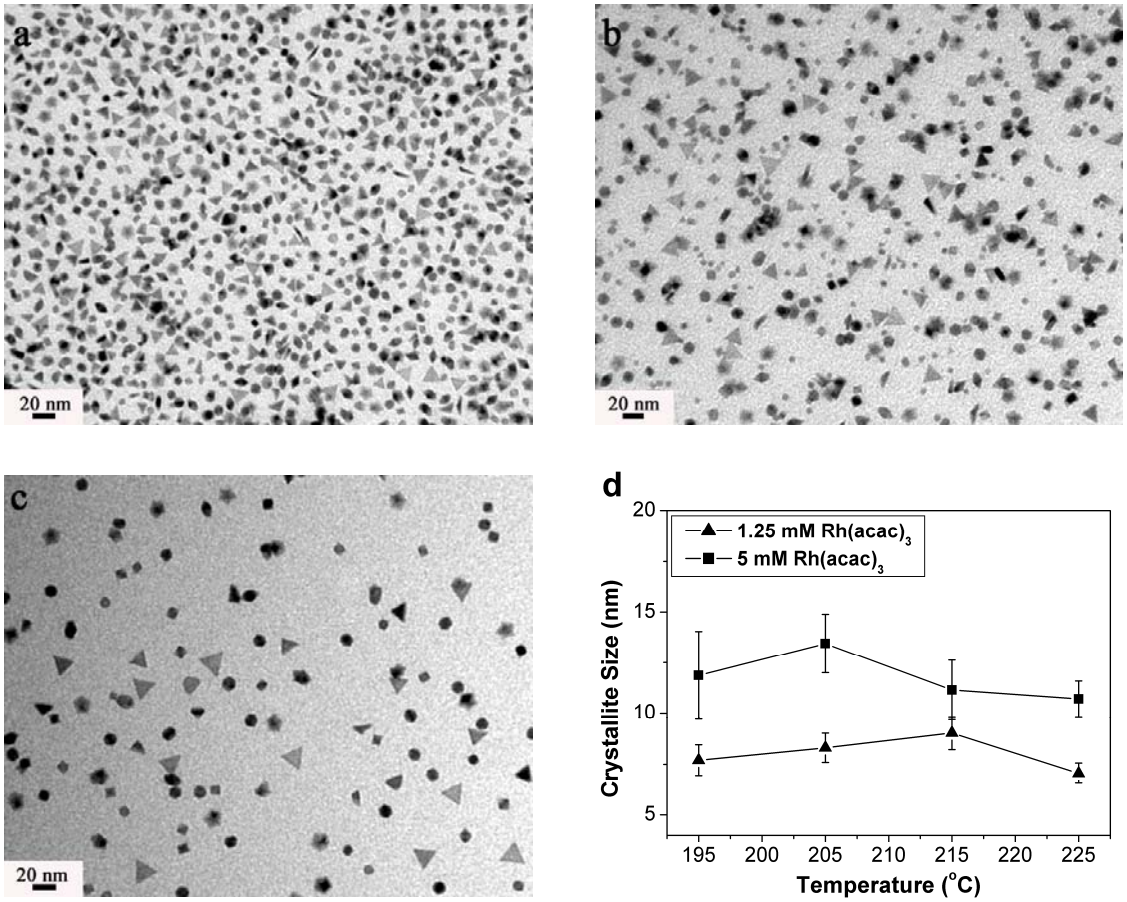

Figure 6.4. TEM images of Rh nanocrystals synthesized at different temperatures for 2 h under Ar ([$Rh(acac)_3$] = 5 mM): (a) 175 °C; (b) 185 °C; (c) 195 °C. (d) Plot of the size of the Rh nanocrystals as a function of temperature.

but with a significant fraction of nanorods, favored by kinetics.[30] At a reaction temperature of 195 °C, 11.9 nm Rh nanocrystals formed (S.D: 18%; Figure 6.4c). For reactions carried out at 205 and 225 °C, monodisperse Rh nanocrystals of 13.5 nm (S.D.: 10%; Figure 6.1c) and 10.7 nm (S.D.: 8.4%), respectively, were formed. It should be noted that the size distribution of the Rh nanocrystals synthesized at 225 °C was significantly narrowed, although the size decreased considerably for [$Rh(acac)_3$] = 5 mM or 1.25 mM (Figure 6.4d), indicating that a balance between the reduction rate of $Rh(acac)_3$ and crystal growth stages is reached at this temperature, resulting in nanocrystals of uniform size. Furthermore, we see that the size of the Rh nanocrystals

synthesized with [$Rh(acac)_3$] = 1.25 mM are considerably smaller and have a narrower size distribution than those synthesized with [$Rh(acac)_3$] = 5 mM at temperatures of 195-225 °C because a low $Rh(acac)_3$ concentration favors a decreased growth rate of the nanocrystals.

6.3.5 Effect of $Rh(acac)_3$ Concentration

At a given reaction temperature, the size of the Rh nanocrystals can be tuned by changing the concentration of $Rh(acac)_3$. For example, at 225 °C with [$Rh(acac)_3$] = 0.156 mM, the resulting Rh nanocrystals are 6.4 nm in size (S.D.: 17%; Figure 6.5a). With a doubling in precursor concentration ([$Rh(acac)_3$] = 0.313 mM), the Rh nanocrystals become more monodisperse with a size of 5.4 nm (S.D.: 9.0%; Figures 6.5a, 6.1h). Between 0.313 mM and 5 mM $Rh(acac)_3$, the resulting nanocrystal size increases with increasing concentration while the percent standard deviation in size remains constant at ~8%. Particles with a mean diameter of 6.5 nm (S.D.: 7.7%; Figures 6.5a, 6.1a), 7.1 nm (S.D.: 7.0%; Figure 6.5a), 9.3 nm (S.D.: 8.6%; Figures 6.5a, 6.1k), and 10.7 nm (S.D.: 8.4%; Figure 6.5a) were synthesized using [$Rh(acac)_3$] = 0.625, 1.25, 2.5, and 5 mM, respectively. Increasing the concentration to 10 mM formed larger 13.5 nm particles with a broadened size distribution (S.D.: 16%; Figure 6.5a). At a concentration of 25 mM, the nanocrystals again become smaller in size (9.5 nm), but still have a large size distribution (S.D.: 19%; Figure 6.5a,b).

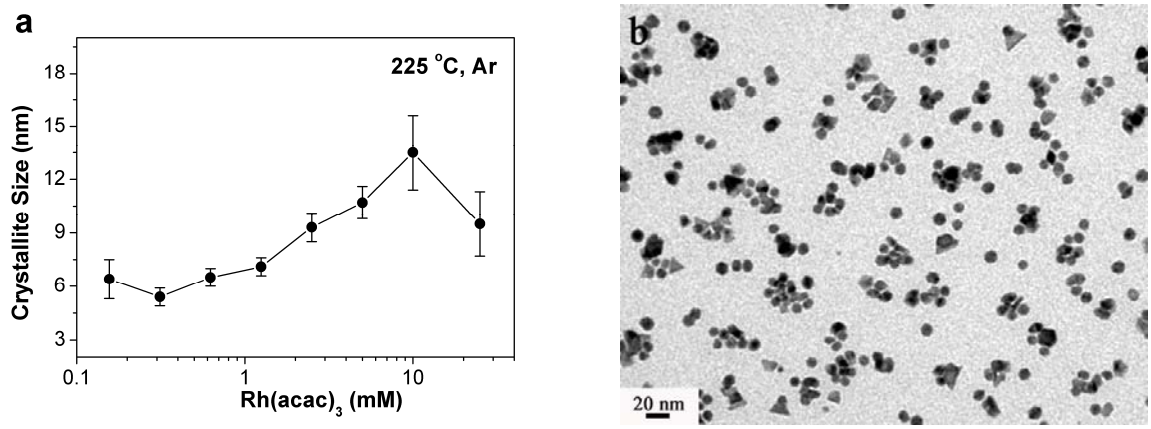

Figure 6.5. (a) Plot of the size of Rh nanocrystals synthesized at 225 °C for 2 h under Ar as a function of the $Rh(acac)_3$ concentration. (b) TEM image of Rh nanocrystals synthesized at 225 °C for 2 h under Ar ($[Rh(acac)_3]$ = 25 mM).

6.3.6 Formation Mechanism of Rh Nanocrystals

In order to obtain improved size/shape control for colloidal noble metal nanoparticles, intensive research has been devoted to the manipulation of the reduction kinetics of metal precursors in the nucleation and crystal growth stages involved in polyol methods.[11, 13, 15, 16, 18, 20, 21, 30, 31] It is believed that control of the reduction kinetics is a key to the formation of monodisperse nanocrystals with well-defined shape. The formation of monodisperse Rh nanocrystals by the polyol method described here is simply illustrated in Scheme 6.1.

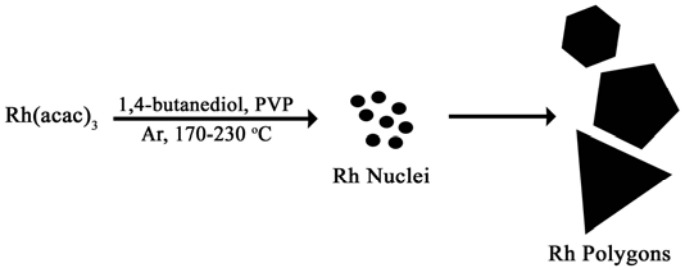

Scheme 6.1. Schematic for the one-step polyol synthesis of monodisperse well-shaped Rh nanocrystals.

We observe that $Rh(acac)_3$ dissolves completely in 1,4-butanediol upon heating above 110 °C, forming a transparent orange-yellow solution. As the solution is heated to 175 °C under Ar, the reduction of $Rh(acac)_3$ by 1,4-butanediol starts, characterized by the appearance of a color change. By either extending the reaction time at 175 °C or raising the reaction temperature above 175 °C, we observe a sequential color change from orange-yellow, to red, to brown, to dark brown, and finally to black. This indicates the gradational reduction of $Rh(acac)_3$ by 1,4-butanediol, presumably because the strongly chelating Rh–O bonds in the $Rh(acac)_3$ complex slow reduction. Therefore, Rh(0) atoms can be gradually produced from the controlled reduction of $Rh(acac)_3$.

Analysis of UV-vis spectroscopic measurements shows that PVP and Hacac ligands display very strong absorption peaks at 208 and 273 nm, respectively, while $Rh(acac)_3$ has peaks at 318 (moderately strong), 258 (weak) and 204 nm (very strong). The peak at ~320 nm is characteristic of $Rh(acac)_3$ and can be used to monitor the consumption of $Rh(acac)_3$ with time and temperature. Figure 6.6 shows UV-vis spectra for reaction aliquots under various conditions and after different reaction times. In contrast to the UV-vis spectrum of pure $Rh(acac)_3$, those taken during reduction show increased intensity for the peak at 265 nm relative to that at 320 nm, probably indicative of the formation of Hacac species following reduction of $Rh(acac)_3$ by 1,4-butanediol. $Rh(acac)_3$ is not completely reduced at 175 or 185 °C after 2 h for $[Rh(acac)_3]$ = 5 mM, as suggested by the presence of the peak at 320 nm (Figure 6.6a). At 195 °C, this peak disappears, corresponding to the complete reduction of $Rh(acac)_3$ after 2 h (Figure 6.6a). It was found that $Rh(acac)_3$ can be completely reduced in 30 min at 215 °C and 12.5 mM $Rh(acac)_3$ (see Figure 6.6b). Considering UV-Vis spectroscopy and TEM measurements (Figures

6.3, 6.4a-c, and 6.6), we can conclude that the consumption of $Rh(acac)_3$ not only occurs during the nucleation stage, but also in the early stages of nanocrystal growth and that higher temperatures favor faster reduction and rapid $Rh(acac)_3$ consumption.

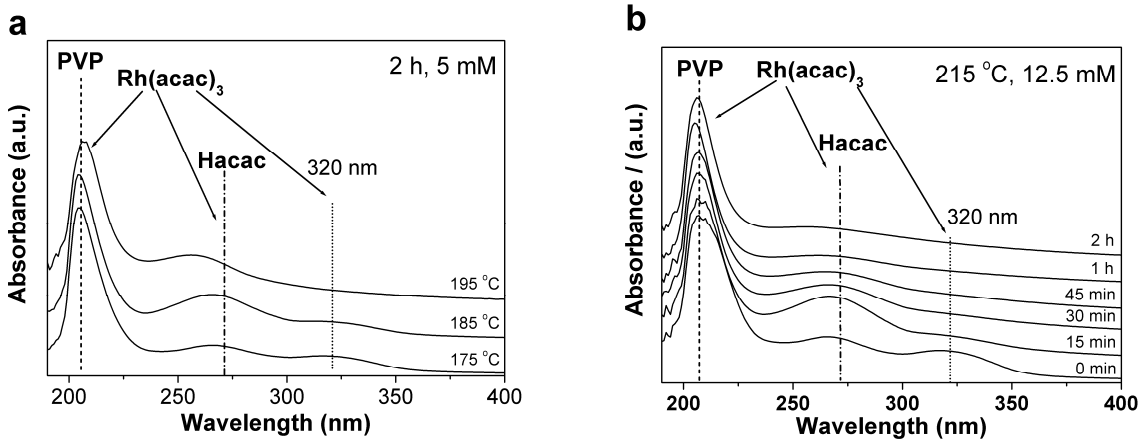

Figure 6.6. (a) UV-Vis spectra of solutions taken at different temperatures after reacting for 2 h under Ar ($[Rh(acac)_3]$ = 5 mM). (b) UV-vis spectra of solutions at increasing reaction times at 215 °C under Ar ($[Rh(acac)_3]$ = 12.5 mM).

For a fixed reaction temperature, it is noted that higher $Rh(acac)_3$ concentrations leads to faster reduction. For instance, when heating reaction solutions with $[Rh(acac)_3]$ = 12.5 mM and 5 mM, the orange-yellow to black color change occurs at 195 and 210 °C, respectively, with identical heating rates; when $[Rh(acac)_3]$ = 1.25 mM, the color changes at 225 °C. An appropriate reduction rate for the growth of monodisperse Rh nanocrystals is obtained at temperatures in excess of 190 °C and with $Rh(acac)_3$ concentrations of 0.313-5 mM. At a given temperature, a lower $Rh(acac)_3$ concentration gives a slower reduction rate and decreased consumption of Rh atoms during crystal growth, resulting in a slower growth rate of Rh nanocrystals. Under this condition, smaller monodisperse Rh

nanocrystals are produced and consequently the size of Rh nanocrystals decreases with the $Rh(acac)_3$ concentration within the range of 0.313-5 mM. This case is similar to the growth of monodisperse Rh nanoparticles by the seeded growth method, i.e., the addition of fewer monomers yields smaller nanocrystals.[10, 11] However, when the $Rh(acac)_3$ concentration is lower than 0.313 mM, a decreased reduction rate continuously produces Rh(0) atoms over a long period of time while suppressing Ostwald ripening; forming polydisperse Rh nanocrystals (Figure 6.5a). On the other hand, at concentrations greater than 5 mM, the rapid reduction rate generates many Rh(0) atoms in a short period of time for consumption during the crystal growth stage while suppressing Ostwald ripening, also resulting in size polydispersity (Figures 6.3 and 6.5a).

It is well known that the surface energies of *fcc* metals follow the order of (111) < (100) < (110) with the (111) surface being the most stable.[27, 28] MTPs ((111) twinned structures) have the lowest free energy and are thus thermodynamically favored for *fcc* noble metals.[15, 27, 28] Considering that our *fcc* Rh polygons (hexagons, pentagons and triangles) with (111) orientations are formed under a moderate reduction rate and relatively high reaction temperatures, and their morphologies appear unchanged with time in the presence or absence of oxidative etching, these shapes can be considered thermodynamically stable. Furthermore, the formation of Rh MTPs (hexagons and pentagons) in high population (>45%, see Table 6.1) is probably due to the high density of planar defects generated on the {111} planes of the Rh nanocrystals during synthesis.

6.3.7 Formation of LB Monolayers

The LB technique is a robust and versatile method for packing nanoscale building blocks such as quantum dots,[32, 33] nanorods[34] and nanowires[35] into long-range ordered 2-

D arrays on different substrates. This method has been successfully employed to make dense LB monolayers of PVP-capped Pt nanocrystals with various shapes (cubes, cuboctahedra and octahedra) for heterogeneous catalytic studies.[17, 18] In this work, we prepare monolayer films of size tunable monodisperse Rh nanocrystals on Si wafers with a LB trough and to investigate the effects of crystallite size on film formation.

After the Rh nanocrystals spread uniformly on the water surface in the LB trough, the resulting surface pressure is 2-4 mN/m, possibly due to the presence of PVP on the nanocrystal surfaces. Figure 10 shows TEM images of LB films formed at different surface pressures for 8.3 nm Rh nanocrystals. As the pressure steadily increases from 4.4 mN/m to 8.1 mN/m and then to 10.4 mN/m due to compression by the mobile barrier, the surface coverage of Rh gradually increases from 11% (Figure 6.7a) to 24% (Figure 6.7b) and then to 33% (Figure 6.7c). At this stage, the Rh nanocrystals are discretely distributed on the substrates, showing no aggregation. As the pressure is further increased to 12.9 mN/m, the monolayer starts to collapse and forms multilayers, as revealed by the observation of nanocrystal aggregates on the TEM grid (surface coverage: 53%; Figure 6.7d). As the LB film is further compressed, the surface pressure increases rapidly up to 23.3 mN/m, and Rh nanocrystal multilayers are formed (Figure 6.7e,f) with a surface coverage of 65-72%.

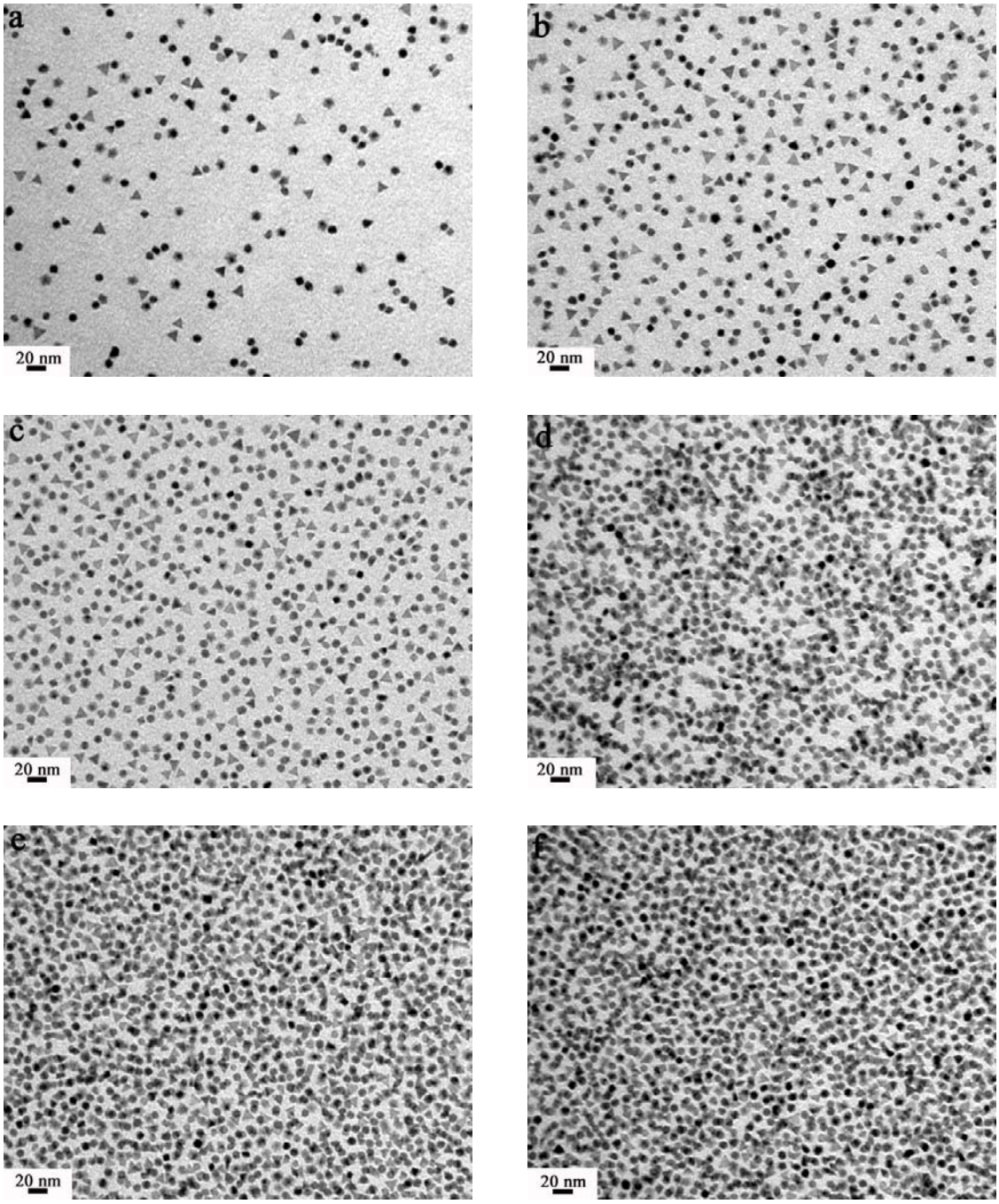

Figure 6.7. TEM images of Langmuir-Blodgett films of 8.3 nm Rh nanocrystals, formed under different surface pressures: (a) 4.4 mN/m; (b) 8.1 mN/m; (c) 10.4 mN/m; (d) 12.9 mN/m; (e) 16.6 mN/m; (f) 23.3 mN/m.

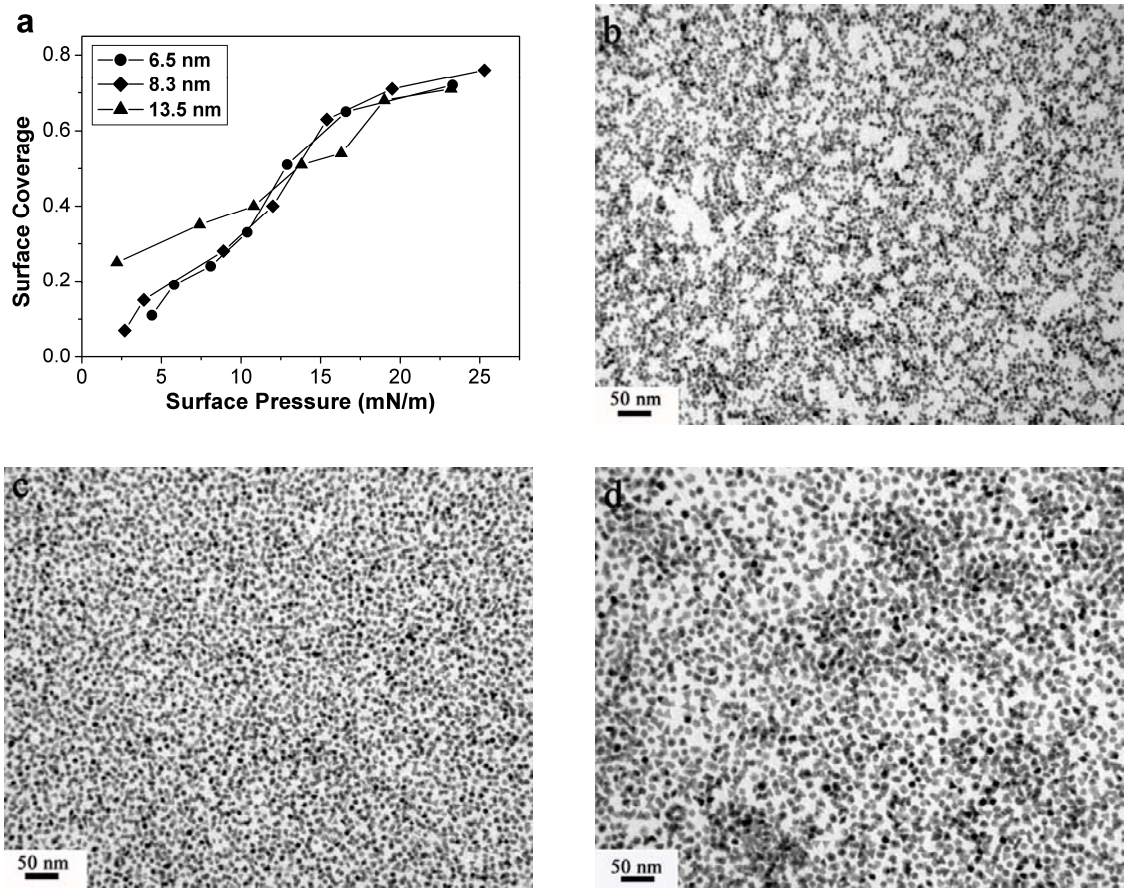

Figure 6.8. (a) Plot of the surface pressure as a function of the surface coverage of Rh Langmuir-Blodgett films. TEM images of the LB monolayers of Rh nanocrystals: (b) 6.5 nm, 10.3 mN/m; (c) 8.3 nm, 10.8 mN/m; (d) 10.7 nm, 10.9 mN/m.

Figure 6.8a depicts the dependence of surface pressure on Rh nanocrystal surface coverage. The surface coverage for the 13.5 nm sample is lower than that of the 6.5 and 8.3 nm samples below 10 mN/m, perhaps as a result of the slightly larger size distribution of the former sample (Table 6.1). In this case, a broadened size distribution for the nanocrystals might prevent effective packing into monolayers at low surface pressures. Beyond 10 mN/m, the curves for the three samples are nearly coincident, indicating that monolayers can be made in the same surface pressure range. Experimentally, for our size-tunable Rh nanocrystals, monolayers form at surface pressures of 10-11 mN/m and

have a surface coverage of 35-64% (Figure 6.8b-d). These monolayer films demonstrate only very short-range order; it is assumed that the shape diversity observed for the Rh nanocrystals, together with the entangled long carbon chain and the hydrophilic pyrrolidone ring of PVP, limits long-range ordering.[18]

6.3.8 Ethylene Hydrogenation

The LB films of Rh nanocrystals transferred onto Si wafers were tested for ethylene hydrogenation activity in a flow reactor. All samples were active for ethylene hydrogenation with turnover frequencies (TOF) of ~0.5 mol ethane/mol Rh_s/sec. The activity (in mmol ethane/cm^2/min) and TOF, along with the coverage of each LB sample, is listed in Table 6.2. The coverage was determined by measuring the fraction of the area of a TEM grid lifted off from the LB surface that was covered by Rh nanocrystals (Figure 6.8). The number of surface Rh atoms on a sample was calculated by geometric considerations by approximating each particle as a sphere. Ethylene hydrogenation rates were measured between 313 K and 373 K for each sample. At temperatures above 333 K deactivation is rapid, likely due to the formation of a carbonaceous overlayer, making an accurate determination of apparent activation energy difficult. The absence of a particle size dependence on TOF is consistent with previous research showing that ethylene hydrogenation is structure insensitive.[36] A TOF of ~0.5 mol ethane/mol Rh_s/sec is in the range of that reported for Rh clusters[37] and Rh single crystals.[38]

Table 6.2. Ethylene Hydrogenation TOF for the LB Monolayers of Differently-sized Rh Nanocrystals on Silicon Wafers

Size (nm)	Coverage[a]	Activity (mmol ethane/cm^2/min)	TOF (mol ethane/mol Rh_s/s)[b,c]
6.5	0.53	0.20	0.59
7.1	0.32	0.10	0.51
7.7	0.56	0.14	0.40
8.3	0.56	0.16	0.44
9.3	0.53	0.19	0.57
10.7	0.64	0.21	0.52

[a] Coverage determined from a 1 μm × 1 μm area of a TEM grid lifted from LB trough.
[b] Surface Rh (Rh_s) determined from geometric considerations.
[c] Reaction conditions were 20 Torr ethylene, 200 Torr H_2, 550 Torr He and 350 K.

6.4 Conclusions

Using $Rh(acac)_3$ as the metal precursor, we have demonstrated the synthesis of monodisperse PVP-capped Rh polygons with tunable sizes ranging from 5 to 15 nm in 1,4-butanediol at temperatures of 170-230 °C under Ar. The polygons are dominated by hexagons, pentagons and triangles exposing (111) surfaces (>65% in yield). Due to the generation of planar defects of the {111} twins in the present synthesis, multiple (111) twinned particles including hexagons and pentagons were formed in a high yield (>45%). Without the use of seeds, the size of the Rh nanocrystals can be manipulated by varying the $Rh(acac)_3$ concentration because of the well-controlled precursor reduction kinetics in the nucleation and crystal growth stages. The polyol method developed here has the merits of one-step synthesis, easy operation, and good reproducibility. Overall, it provides a good recipe for the size control of Rh nanocrystals in solution. By the LB technique, monolayer films were produced for the differently-sized Rh nanocrystals on Si

wafers, under nearly the same surface pressures. Preliminary catalytic tests reveal that the Rh nanocrystal monolayers are active for ethylene hydrogenation.

6.5 References

(1) Ahmadi, T. S.; Wang, Z. L.; Green, T. C.; Henglein, A.; ElSayed, M. A., *Science* **1996,** 272, 1924.

(2) Anderson, M. L.; Stroud, R. M.; Rolison, D. R., *Nano Lett.* **2003,** 3, 1321.

(3) Launay, F.; Roucoux, A.; Patin, H., *Tetrahedron Lett.* **1998,** 39, 1353.

(4) Narayanan, R.; El-Sayed, M. A., *J. Phys. Chem. B* **2005,** 109, 12663.

(5) Thomas, J. M.; Johnson, B. F. G.; Raja, R.; Sankar, G.; Midgley, P. A., *Acc. Chem. Res.* **2003,** 36, 20.

(6) Somorjai, G. A., *Introduction to Surface Chemistry and Catalysis*. Wiley: New York, 1994.

(7) Rioux, R. M.; Song, H.; Hoefelmeyer, J. D.; Yang, P.; Somorjai, G. A., *J. Phys. Chem. B* **2005,** 109, 2192.

(8) Song, H.; Rioux, R. M.; Hoefelmeyer, J. D.; Komor, R.; Niesz, K.; Grass, M.; Yang, P. D.; Somorjai, G. A., *J. Am. Chem. Soc.* **2006,** 128, 3027.

(9) Van Hardeveld, R.; Hartog, F., *Surf. Sci.* **1969,** 15, 189.

(10) Hoefelmeyer, J. D.; Niesz, K.; Somorjai, G. A.; Tilley, T. D., *Nano Lett.* **2005,** 5, 435.

(11) Humphrey, S. M.; Grass, M. E.; Habas, S. E.; Niesz, K.; Somorjai, G. A.; Tilley, T. D., *Nano Lett.* **2007,** 7, 785.

(12) Park, K. H.; Jang, K.; Kim, H. J.; Son, S. U., *Angew. Chem. Int. Ed.* **2007,** 46, 1152.

(13) Zettsu, N.; McLellan, J. M.; Wiley, B.; Yin, Y. D.; Li, Z. Y.; Xia, Y. N., *Angew. Chem. Int. Ed.* **2006,** 45, 1288.

(14) Stowell, C. A.; Korgel, B. A., *Nano Lett.* **2005,** 5, 1203.

(15) Xiong, Y. J.; Chen, J. Y.; Wiley, B.; Xia, Y. N., *J. Am. Chem. Soc.* **2005,** 127, 7332.

(16) Chen, J. Y.; Herricks, T.; Xia, Y. N., *Angew. Chem. Int. Ed.* **2005,** 44, 2589.

(17) Lee, H.; Habas, S. E.; Kweskin, S.; Butcher, D.; Somorjai, G. A.; Yang, P. D., *Angew. Chem. Int. Ed.* **2006,** 45, 7824.

(18) Song, H.; Kim, F.; Connor, S.; Somorjai, G. A.; Yang, P. D., *J. Phys. Chem. B* **2005,** 109, 188.

(19) Chen, S. H.; Carroll, D. L., *J. Phys. Chem. B* **2004,** 108, 5500.

(20) Tao, A.; Sinsermsuksakul, P.; Yang, P. D., *Angew. Chem. Int. Ed.* **2006,** 45, 4597.

(21) Seo, D.; Park, J. C.; Song, H., *J. Am. Chem. Soc.* **2006,** 128, 14863.

(22) Wu, H. Y.; Liu, M.; Huang, M. H., *J. Phys. Chem. B* **2006,** 110, 19291.

(23) Niesz, K.; Koebel, M. M.; Somorjai, G. A., *Inorg. Chim. Acta* **2006,** 359, 2683.

(24) Pellegatta, J. L.; Blandy, C.; Colliere, V.; Choukroun, R.; Chaudret, B.; Cheng, P.; Philippot, K., *J. Mol. Catal. A: Chem.* **2002,** 178, 55.

(25) Yoon, T. J.; Kim, J. I.; Lee, J. K., *Inorg. Chim. Acta* **2003,** 345, 228.

(26) Dietz, W. A., *J. Gas Chromatogr.* **1967,** 5, 68.

(27) Marks, L. D., *Rep. Prog. Phys.* **1994,** 57, 603.

(28) Wang, Z. L., *J. Phys. Chem. B* **2000,** 104, 1153.

(29) Narayanan, R.; El-Sayed, M. A., *J. Phys. Chem. B* **2003,** 107, 12416.

(30) Xiong, Y. J.; Cai, H. G.; Wiley, B. J.; Wang, J. G.; Kim, M. J.; Xia, Y. N., *J. Am. Chem. Soc.* **2007,** 129, 3665.

(31) Xiong, Y. J.; McLellan, J. M.; Yin, Y. D.; Xia, Y. N., *Angew. Chem. Int. Ed.* **2007,** 46, 790.

(32) Collier, C. P.; Saykally, R. J.; Shiang, J. J.; Henrichs, S. E.; Heath, J. R., *Science* **1997,** 277, 1978.

(33) Markovich, G.; Collier, C. P.; Henrichs, S. E.; Remacle, F.; Levine, R. D.; Heath, J. R., *Acc. Chem. Res.* **1999,** 32, 415.

(34) Kim, F.; Kwan, S.; Akana, J.; Yang, P. D., *J. Am. Chem. Soc.* **2001,** 123, 4360.

(35) Whang, D.; Jin, S.; Wu, Y.; Lieber, C. M., *Nano Lett.* **2003,** 3, 1255.

(36) Dorling, T. A.; Eastlake, M. J.; Moss, R. L., *J. Catal.* **1969,** 14, 23.

(37) Argo, A. M.; Odzak, J. F.; Goellner, J. F.; Lai, F. S.; Xiao, F. S.; Gates, B. C., *J. Phys. Chem. B* **2006,** 110, 1775.

(38) Quinlan, M. A. Structure Sensitivity Studies of Ethylene Hydrogenation on Platinum and Rhodium Surfaces. University of California, Berkeley, CA, 1996.

Chapter 7: Reactive Oxide Overlayer on Rh Nanoparticles during CO Oxidation and its Size Dependence Studied by In Situ Ambient Pressure XPS

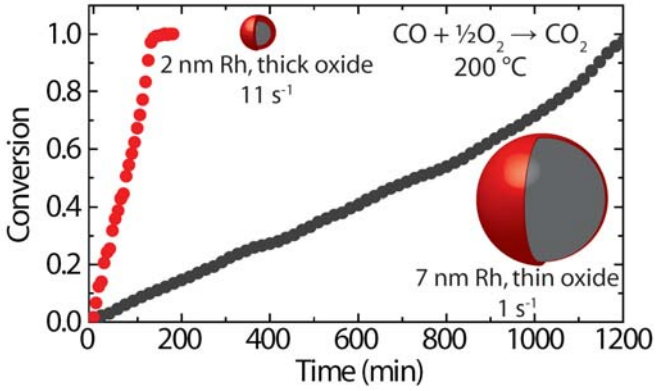

Advancements in nanoscale fabrication and in situ characterization over the past decade have led to a significant increase in understanding the surface structure of working catalysts. We report the first ambient pressure X-ray photoelectron spectroscopy (APXPS) study of Rh nanoparticles during CO oxidation by O2 with supporting catalytic studies. 2, 2.5, 3.5, 7, and 11 nm Rh nanoparticles were synthesized in the presence of poly(vinyl pyrrolidone) and deposited onto Si wafers by Langmuir-Blodgett deposition as model catalysts. The smaller particles are ~ 5 times more active for CO oxidation at an O_2/CO ratio of 2.5 and are significantly more oxidized during reaction as determined by APXPS. Additionally, a shoulder in the O 1s spectrum indicates the formation of a Rh oxide or reaction intermediate layer that is not present when heating in O2 alone, suggesting a unique surface structure during reaction. We postulate that the enhanced oxide formation on small nanoparticles is correlated with the increase in turnover frequency for CO oxidation.

7.1 Introduction

CO oxidation is one of the most studied heterogeneous reactions, being scientifically and industrially important, particularly for removal of CO from exhaust streams[1] and preferential oxidation for hydrogen purification in fuel cell applications[2]. The precious metals Ru, Rh, Pd, Pt, and Au are most commonly used for this reaction because of their high activity and stability. Despite the wealth of experimental and theoretical data, it remains unclear what is the active surface for CO oxidation under catalytic conditions for these metals. Here, we utilize *in situ* synchrotron ambient pressure X-ray photoelectron spectroscopy (APXPS) to monitor the oxidation state at the surface of Rh nanoparticles during CO oxidation and demonstrate that the active catalyst is a surface oxide, the formation of which is dependent on particle size. The particle size dependence of oxide formation correlates with an increase in reaction rate with decreasing particle size.

Many single crystal CO oxidation studies over Rh have suggested that the reaction is structure insensitive and that oxide formation decreases the reaction rate.[3, 4] However, recent advances in synthetic techniques and *in situ* experimentation have revealed that the oxidation state and stoichiometry of the surface oxide greatly affects CO oxidation rates[5-8]. At low temperatures or low O_2/CO ratios, the reaction is negative order in CO, which strongly adsorbs to the catalyst surface and inhibits O_2 adsorption. At high temperatures or high O_2/CO ratios, the catalyst surface becomes saturated with O atoms and the reaction proceeds more rapidly. It has been demonstrated that small nanoparticles (NPs) of Pd[6] are more active for CO oxidation than larger particles and single crystals, while the opposite is reported in the case of Pt.[9] For Rh NPs, no particle

size effect was observed for supported Rh catalysts,[10] but a strong particle size dependence was observed for Rh NPs prepared by electron beam evaporation for transient CO oxidation over NPs precovered with oxygen.[11]

For this investigation we have prepared small, polymer stabilized Rh NPs with a narrow size distribution and studied CO oxidation over these particles; polymer stabilized NP syntheses enable control of NP size, shape and/or composition for reaction studies.[12, 13] The turnover frequency (TOF) for CO oxidation increases from 5 to 28 times higher than over a Rh foil at 200 °C and the apparent activation decreases from 27.9 kcal mol^{-1} to 19.0 kcal mol^{-1}as the particle size decreases from 11 nm to 2 nm. APXPS of 2 nm and 7 nm Rh NPs during CO oxidation near 1 Torr provides the first *in situ* measurement of the oxidation state of Rh NPs during CO oxidation and demonstrates that smaller particles are more oxidized than larger particles during reaction at 150 – 200 °C. A surface oxygen species is also observed during CO oxidation that is not present when heating in O_2 alone, possibly indicating a unique active oxide phase on Rh NPs. This oxide phase may alter the relative bonding geometries of CO and/or O on the Rh surface, thereby lowering the activation energy for the reaction.[14]

7.2 Experimental

7.2.1 Nanoparticle Synthesis

The synthesis of 7 and 11 nm Rh NPs was described in Chapter 5. For the 2 nm Rh NPs, 0.1 mmol $Rh(acac)_3$, 0.3 mmol sodium citrate, and 1 mmol poly(vinylpyrrolidone) (PVP, 55K, molarity in terms of monomer units), were added to 20 ml of 1,4-butanediol in a 50 ml three-necked flask at room temperature. The stock solution was heated to 140 °C in a Glas-Col electromantle (60 W; 50 ml) with a Cole-

Parmer temperature controller (Diqi-sense®), and was evacuated at this temperature for 20 min to remove water and oxygen under magnetic stirring, resulting in an optically transparent orange-yellow solution. The flask was then heated to 220 °C at a rate of 10 °C min^{-1}, and maintained at this temperature (±2 °C) for 2 h under Ar. During the reaction, the color of the solution gradually turned from orange-yellow to black. When the reaction was complete, an excess of acetone was poured into the solution at room temperature to form a cloudy black suspension. This suspension was separated by centrifugation at 4200 rpm for 6 min, and the black product was collected by discarding the colorless supernatant. The precipitated Rh NPs were washed with acetone once then re-dispersed in ethanol. The 2.5 and 3.5 nm Rh NPs were synthesized similarly using 0.1 mmol and 0.025 mmol sodium citrate, respectively.

7.2.2 CO Oxidation

Catalytic reactions were studied in a Pyrex reactor connected to a ¼" stainless steel manifold containing mass flow controllers (Unit Instruments) for delivery of reactant gases. Carbon monoxide (Praxair, UHP, 99.99%), oxygen (Praxair, UHP, 99.995%) and helium (Praxair, UHP, 99.999%) were used as received. The catalyst (a silicon wafer of ~ 100 mm^2) was placed in a Pyrex tube placed in line with the Pyrex reactor system and inside a heater. The temperature was measured by a thermocouple in contact with the Pyrex tube near the sample. Reactants and products were detected by gas chromatography (Hewlett Packard 5890). The reactor was run in batch with the use of a recirculation pump. All measurements were taken at 20 Torr CO and 50 Torr oxygen and the recirculated volume was 160 mL. The TOF was calculated from the surface coverage

and sample size by assuming that the Rh nanocrystals were spherical and non-overlapping.

7.2.3 Ambient Pressure XPS

For these experiments, LB films of Rh NPs were formed on ~1 cm^2 pieces of silicon wafer and the samples were stored in a desiccator for about one week prior to the ambient pressure XPS (APXPS) experiments. When mounted, the sample is in contact with a button heater and thermocouple for temperature control. The aperture for electron collection is ~ 1 mm from the sample surface and has a diameter of 0.3 mm.[15] Each of the two samples were treated similarly and the full set of experiments involved initially taking scans of the O 1s at a photon energy of 725 eV, N 1s at 600 eV, Rh 3d at 510 eV, C 1s at 485 eV, and the Fermi edge region at each of the photon energies used. Beam damage was investigated by taking successive scans of the Rh 3d and O 1s regions. It was determined that the 7 nm NP sample was not affected by the X-ray beam, but the 2 nm NP sample was. Further, we observed that only the Rh 3d region changed over time with beam damage and as a result, all spectra reported for the 2 nm sample are from a fresh location on the sample immediately after opening the shutter for the X-ray beam.

After this initial set of scans, 200 mTorr CO was introduced into the chamber. In order to maintain 200 mTorr CO, a leak valve is opened (which is located on the far side of the chamber) and kept open as gasses are constantly pumped out through the lens aperture near the sample surface. After CO is introduced, scans were obtained at room temperature, 100 °C, 150 °C, and 200 °C. The sample was then cooled to 30 °C and scans were again obtained followed by evacuation of the chamber to ~ 5×10^{-8} Torr and another set of scans was obtained. Each full set of scans took about 30 minutes. This

procedure was then repeated for 500 mTorr O_2 and the reaction mixture of 200 mTorr CO and 500 mTorr O_2. The actual partial pressure of gases during reaction was estimated by mass spectrometry during dark runs. During reaction, the chamber contains 20 mTorr, CO, 180 mTorr CO_2, and 410 mTorr O_2. The majority of the turnover is attributed to Pt wires that connect to the heater.

Kinetic measurements for CO oxidation on the Rh NP films were carried out as previously described,[16] but using flow rates of O_2 and CO to obtain pressures of 50 Torr O_2 and 20 Torr CO in the batch reactor cell. Reaction rates were measured over the temperature range 150 to 225 °C Turnover frequencies were calculated using a geometric consideration of the total number of surface Rh atoms for each sample.

7.2.4 XPS Peak Fitting

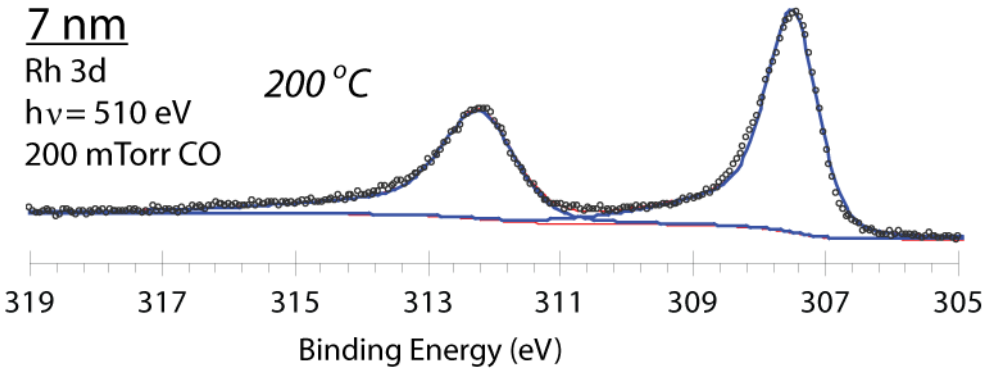

Figure 7.1: Rh 3d spectrum for the 7 nm film under 200 mTorr CO fit with a single peak.

First, the binding energy for all spectra was shifted such that the maximum in the C 1s peak aligned with the reported value of 285.4 eV for PVP.[17] The peak parameters were initially determined for Rh 3d for the 7 nm NP film heated to 200 °C in CO. This sample was considered to be completely reduced and thus could be used to simplify the initial fitting procedure. Using XPS Peak 4.1 (Freeware available at

http://www.phy.cuhk.edu.hk/~surface), the spectrum was fit with a Shirley background. The literature value of the spin orbit splitting (S.O.S. = 4.74 eV) and the known ratio of the $3d_{5/2}$ to $3d_{3/2}$ (3:2) were used. The peaks were optimized by allowing the %Lorenzian/Gaussian (% L-G) and full width at half maximum (FWHM) to adjust automatically and manipulating the asymmetry and tail manually until an optimum fit was achieved. The resulting parameters are: TS = 0.155, TL = 180 (TS and TL are parameters for the asymmetric tail of peaks), 30% L-G; $3d_{5/2}$: binding energy (BE) = 306.51 eV, FWHM = 0.91 eV; $3d_{3/2}$: FWHM = 1.29 eV (Figure 7.1).

The same TS, TL, and % L-G were used for all peaks and all spectra. The next spectral region to be fit was the Rh 3d peak for the 2 nm NP film under 500 mTorr O_2 at 200 °C because this was considered to be the most oxidized sample (not including samples during reaction). Using the same parameters for the Rh(0) peak from before, a second peak was added. It was found that a third peak was needed to properly fit the spectrum, so one Rh(0) peak and two Rh(X+) peaks were used and optimized using XPS Peak 4.1. For the remaining spectra, the same relative peak shifts for the three peaks were used, although the absolute BE was allowed to move up to 0.2 eV to account for inaccuracy in BE corrections and also for uncertainties in how the BE shifts with particle size and particle separation for these samples.[18, 19] The peak positions of the two Rh(X+) peaks is +0.91 and +2.01 relative to Rh(0).

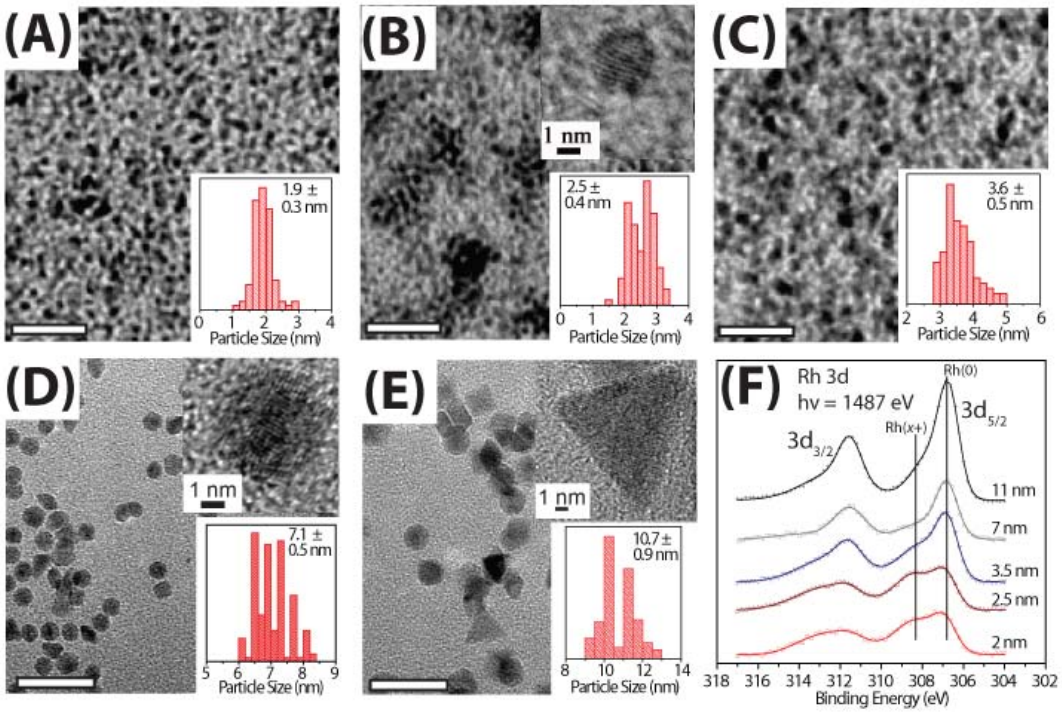

Figure 7.2: TEM images with insets of particle size distribution histograms of 100 particles for (A) 2 nm, (B) 2.5 nm, (C) 3.5 nm, (D) 7 nm, and (E) 11 nm Rh NPs. All scale bars are 20 nm except for the HRTEM insets. (F) Rh 3d XPS spectra of the 2, 2.5, and 3.5 nm Rh NPs together with previously synthesized 7 and 11 nm Rh NPs, showing the increase in oxidized Rh as the particle size decreases.

7.3 Results and Discussion

7.3.1 Nanoparticle Synthesis

The synthesis of monodisperse Rh NPs by polyol reduction using polyvinylpyrrolidone (PVP) as a capping agent and $Rh(acac)_3$ as a Rh precursor[20] was extended to smaller sizes by the addition of sodium citrate. Using this approach, Rh NPs of 2 nm (1.9 ± 0.3 nm), 2.5 nm (2.5 ± 0.4 nm), and 3.5 nm (3.6 ± 0.5 nm) were produced. Monolayer films of these particles were then prepared in a Langmuir-Blodgett (LB) trough and characterized with transmission electron microscopy (TEM) and XPS (Figure 7.2). In a detailed study using PVP stabilized polyol reduction for Rh NP synthesis, we

previously synthesized Rh NPs of 5 – 15 nm.[20] Using the same general procedure, 2 nm, 2.5 nm, and 3.5 nm Rh NPs were formed with the addition of 1.25 mM, 7.5 mM, or 15 mM sodium citrate, respectively. Panels (A), (B), and (C) of Figure 7.2 show TEM images of the NPs with insets of size distribution histograms taken from 100 particles. Figure 7.2(F) shows X-ray photoelectron spectra for the Rh 3d peak of the as-synthesized particles after LB deposition onto a silicon wafer. It is clear that the ratio of oxidized Rh to reduced Rh increases as the particle size decreases.

X-ray diffractograms are shown in Figure 7.3. Well-resolved diffraction peaks are only present for the particles > 2.5 nm and broadening of the peaks reveals the nanostructuring of the Rh particles.

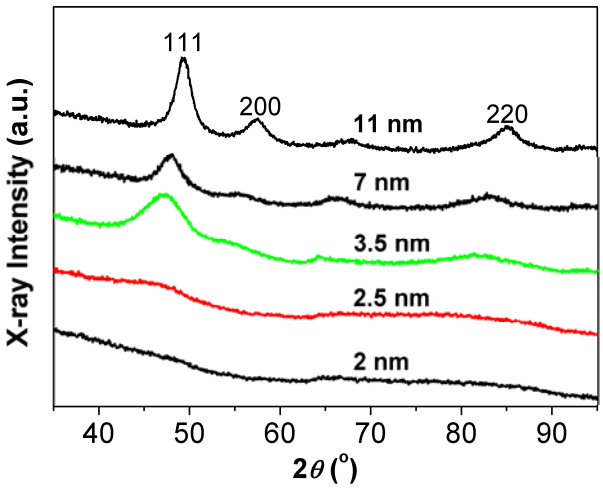

Figure 7.3: X-ray diffractograms of 11, 7, 3.5, 2.5, and 2 nm Rh NPs showing the 111, 200, and 220 diffraction peaks.

7.3.2 CO Oxidation

The three samples of small Rh NPs (2, 2.5, and 3.5 nm) and two samples previously synthesized, 7 nm (7.1 ± 0.5 nm) and 11 nm (10.7 ± 0.9 nm) (Figure 7.2 (D) and (E)) were tested for catalytic activity in CO oxidation by O_2 in a batch reactor monitored with a gas chromatograph. The pressures of CO and O_2 were 20 Torr and 50

Torr, respectively, with a back pressure of He to reach 900 Torr. The activity was measured at 150, 175, 200, and 225 °C to determine the apparent activation energy. Figure 7.4(A) shows the TOF and apparent activation energy of the five samples relative to a Rh foil. The TOF of a Rh foil was measured using the same procedure as a standard reference. The TOF increases from 5.5 times that of Rh foil over 11 nm Rh NPs to 28.0 times that of Rh foil over 2 nm Rh at 200 °C (Rh foil TOF = 0.28 s^{-1}). The apparent activation energy concurrently decreases from 27.9 kcal mol^{-1} to 19.0 kcal mol^{-1}. Both the TOF and apparent activation energy fit to an exponential, which is consistent with the thermodynamics of oxide stability for nanoparticles as a function of size (Equation (7.1)).

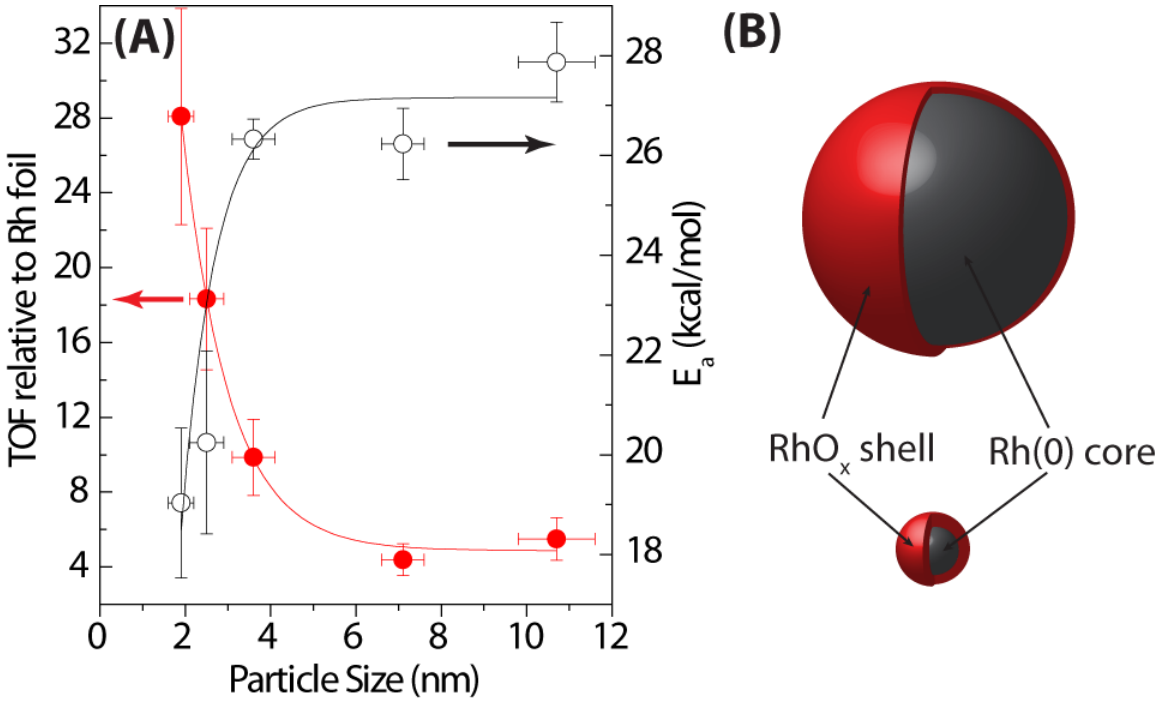

Figure 7.4: (A) Turnover Frequency relative to a Rh foil at 50 Torr O_2, 20 Torr CO, and 200 °C and activation energy (150 – 225 °C) for CO oxidation are both particle size dependent. (B) The thickness of the oxide shell scales with particle size; 2 nm and 7 nm NPs are illustrated here with the oxide layers shown to scale, as determined by APXPS.

7.3.3 Ambient Pressure XPS

The Rh 3d spectra in the presence of 200 mTorr CO and 500 mTorr O_2 at 150 and 200 °C are shown in Figure 7.5. The NPs of both samples are initially oxidized because they were previously exposed to O_2 at 200 °C; the surface of the 7 nm NPs are 54% Rh(*X*+) and the 2 nm NPs are 70% Rh(*X*+) when CO and O_2 are first introduced into the chamber. Both samples initially reduce in the reaction mixture, with the amount of Rh(*X*+) decreasing to 8% for the 7 nm NPs and to 43% for the 2 nm NPs at 150 °C.

Continued heating, however, results in re-oxidation of the Rh surface, indicating that the coverage of CO on the NP surface decreases and there is a simultaneous increase in O coverage. The fraction of Rh(*X*+) increases to 25% for the 7 nm NPs and to 67% for the 2 nm NPs at 200 °C. This data confirms that the active phase for Rh in CO oxidation is a surface oxide or an oxide of a few atomic layers. It also provides *in situ* evidence that smaller NPs more readily form this surface oxide under reaction conditions, which is consistent with TOF and activation energy measurements (Figure 7.4(A)).

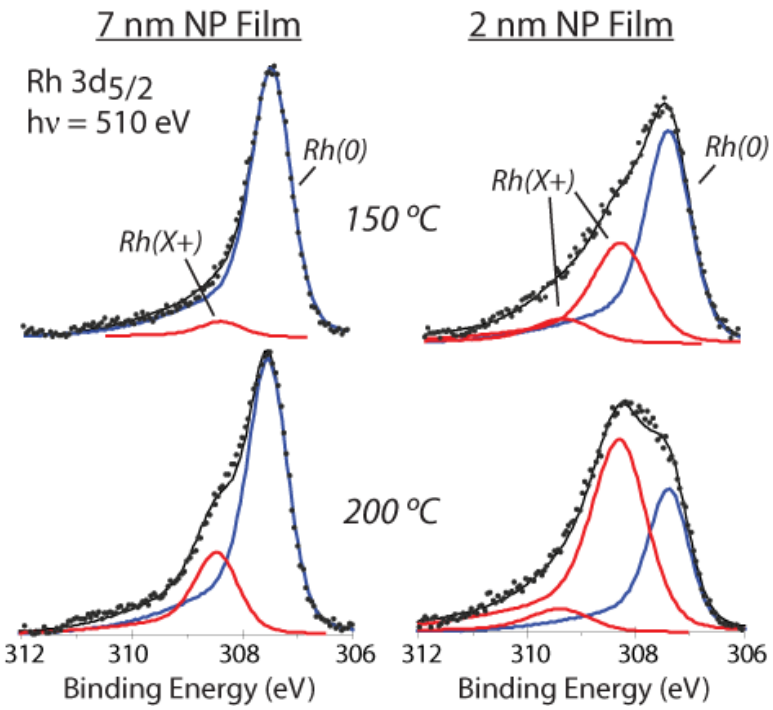

Figure 7.5: APXPS spectra of the Rh $3d_{5/2}$ peak with fits for reduced Rh (blue) and oxidized Rh (red). The NPs of both samples initially reduce and then oxidize at higher temperatures. The 2 nm NPs are more oxidized at all temperatures. The two Rh(*X*+) peaks are attributed to Rh atoms in two different oxidation states or coordinated to a different number of oxygen atoms.

If the mean free path (MFP) of the photoelectrons is taken to be 0.5 nm,[21] then the thickness of the oxide layer formed can be roughly estimated by considering the nanoparticles as spheres and the XPS intensity from each layer decreasing exponentially with depth. For example, for a 1.9 nm NP, the first layer comprises 52% of the atoms and 67% of the XPS intensity and the second layer comprises 30% of the atoms and 25% of the XPS intensity. Using this method, the oxide overlayer is estimated to be 0.6 of a layer, 1, and 1.6 layers for the 2 nm NPs at 150, 200, and 275 °C, respectively. For the 7 nm NPs, there is only 0.2 and 0.6 of a layer at 150 and 200 °C, respectively, indicating incomplete oxide formation of even a single layer over the larger NPs. A comparison of the two samples at 200 °C is illustrated to scale in Figure 7.4(B). It should be noted that

Rh coordinated to a single O atom has been reported at -0.22 eV from the bulk Rh(0), but is not resolved in this study.[22, 23]

Under the conditions of these experiments, the oxygen chemical potential is high enough that the bulk oxide is thermodynamically stable (μ_O = -0.36 eV at 25 °C, -0.62 eV at 200 °C), but it has been shown that for Rh single crystals under similar temperatures and pressures, the oxide formation is kinetically controlled.[22] Although this system is also likely under kinetic control, it is instructive to understand how NP size affects oxide stability. A simple thermodynamic model for nanoparticles, similar to that developed for thin films,[24] has been formulated and used to understand the dissociation pressure of a RhO_2 NP as a function of particle size (see Appendix):

$$P_{O_2}^{NP} = P_{O_2}^{bulk} \exp\left(-\frac{21\text{ nm}}{r_0}\right) \tag{7.1}$$

Where P is the dissociation pressure of a RhO_2 NP and r_0 is the size of the corresponding metal Rh NP. From this equation, the dissociation pressure of a 7 nm RhO_2 NP is 20 times lower than that of the bulk, while for a 2 nm Rh NP, the dissociation pressure is decreased by a factor of 4×10^4. The increased stability of a thin oxide film has been explored[24] and appears to be even more pronounced for nanoparticles.

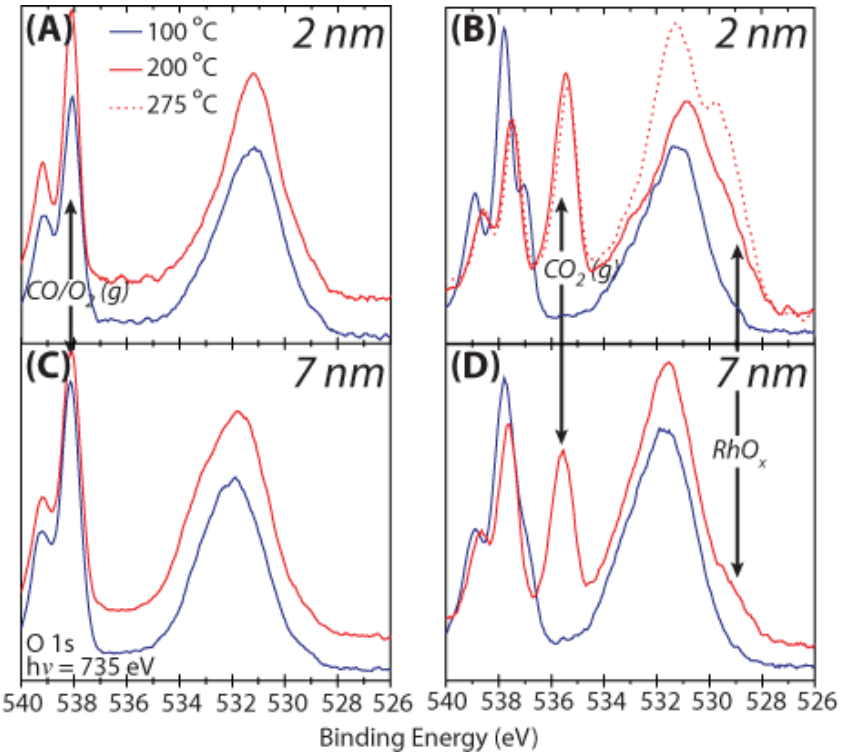

Figure 7.6: O 1s spectra of 2 nm and 7 nm Rh NPs in 500 mTorr O_2 ((A) and (C)) and during reaction (410 mTorr O2, 20 mTorr CO) ((B) and (D)). When exposed to both O_2 and CO, a peak at higher binding energy forms, which is attributed to a RhO_x species.

In addition to the increase in oxidized Rh observed in the Rh 3d spectra at 200 °C under reaction conditions, a low BE (~529.5 eV) peak in the O 1s spectrum is also observed under these conditions (Figure 7.6 (B) and (D)) that is not present during heating in O_2 alone ((A) and (C)). This suggests that a distinct oxide forms during CO oxidation that is stabilized by CO or a reaction intermediate that does not form when the NPs are simply heated in O_2.[5] The peak associated with this "reactive oxide" overlayer diminishes upon evacuation of the reaction chamber, further establishing that this oxide is intimately correlated with the CO oxidation reaction. Most of O1s intensity associated with surface O (peak centered at ~ 531 eV) is attributed to PVP. Further characterization of this oxide and its size dependence is necessary and may enhance theoretical models for understanding nanoparticle activity as a function of metal type and particle size; current

models usually assume that the active surface is metallic because this surface oxide is not well characterized or understood.[25] Gas phase O_2, CO, and CO_2 are also observed in Figure 7.6 and we will utilize this added information in future studies.

In a recent theoretical study, Gong *et al.* carried out DFT calculations for CO + O $\rightarrow$ CO_2 on metal and oxide surfaces including Rh(111) and found that the reaction barrier is lower over the oxide than over the metal.[14] In this study we have directly correlated the amount of surface oxide on two different sizes of Rh NPs with the TOF and apparent activation energy. The observed particle size dependence of CO oxidation over Rh NPs in this study appears to result from the increased oxide formation over small particles, which is the more active phase.

7.4 Conclusions

In situ studies are invaluable to the understanding of a working catalyst and this communication demonstrates the first observation of the active phase of a Rh nanoparticle catalyst during CO oxidation by photoelectron spectroscopy, providing evidence for the observed size dependence of this reaction. Further studies are required to understand the form of the reactive oxide that is formed and the role, if any, of PVP in the formation of the oxide.

7.5 Appendix

A simple thermodynamic model for the dissociation pressure of metal oxide nanoparticles can be developed by building on the same concepts used by Campbell for thin films of oxides.[24]

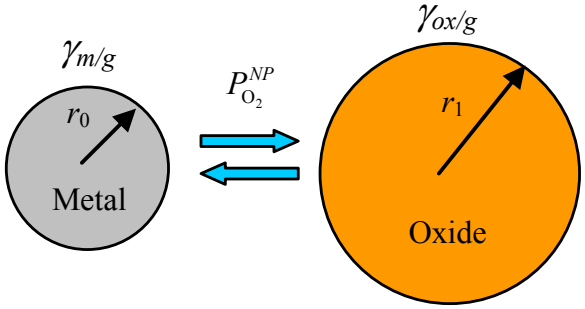

Figure 7.7: A metal sphere in equilibrium with its fully-oxidized counterpart. r_0 and r_1 are the radii of the metal and oxide sphere, respectively and γ is the surface/interface tension.

When a metal sphere is in equilibrium with its fully-oxidized counterpart, the radius of the metal sphere is related with the radius of its oxide, since they contain the same number, n_M, of metal atoms. For the reaction $M(s)+\mathrm{O}_2 \rightleftarrows M\mathrm{O}_2(s)$, we have

$$n_M = \frac{4}{3}\frac{\pi r_0^3}{v_M} = \frac{4}{3}\frac{\pi r_1^3}{v_{MO_2}} \tag{7.2}$$

so

$$\frac{r_0}{r_1} = \left(\frac{v_M}{v_{MO_2}}\right)^{1/3}, \tag{7.3}$$

here v_M and v_{MO_2} are the molar volumes of the metal and the metal oxide, respectively.

From the total surface free energy of the metal particle,

$$G_M^S = \gamma_M S = 4\pi r_0^2 \gamma_M, \tag{7.4}$$

and that of the oxide particle,

$$G_{MO_2}^S = 4\pi r_1^2 \gamma_{MO_2}, \tag{7.5}$$

we can obtain the surface free energy change for converting one mole of metal atoms into their oxide,

$$\Delta G^S = \frac{G^S_{MO_2} - G^S_M}{n_M} = 3\left(\frac{v_{MO_2}\gamma_{MO_2}}{r_1} - \frac{v_M\gamma_M}{r_0} \right) \tag{7.6}$$

Using Eq. (7.3), we further have

$$\Delta G^S = 3\left(1 - \frac{\alpha}{\beta}\right)\frac{v_{MO_2}\gamma_{MO_2}}{r_1}, \tag{7.7}$$

where $\alpha = \frac{\gamma_M}{\gamma_{MO_2}}$, and $\beta = \left(\frac{v_{MO_2}}{v_M}\right)^{2/3}$.

Including this surface free energy contribution, the dissociation pressure of the oxide sphere can be given as

$$P^{film}_{O_2} = P^{bulk}_{O_2} \exp\left[-3\left(\frac{\alpha}{\beta} - 1\right)\frac{\gamma_{ox}v_{ox}}{RTr_1} \right] \tag{7.8}$$

Eq.(7.8) shows that, if $\frac{\alpha}{\beta} > 1$, the smaller the oxide particle, the more stable it is. This is true for most metals, since $\alpha = \frac{\gamma_M}{\gamma_{MO_2}}$ is typically greater than $\beta = \left(\frac{v_{MO_2}}{v_M}\right)^{2/3}$.

At any given temperature and pressure, α can be estimated from the oxygen chemical potential[26] and the surface free energy of the oxide of interest at that chemical potential.[22, 23] Additionally, β can be calculated from the known molar volumes of the metal and the oxide. Employing the work of Reuter and Scheffler[26] together with that by Kohler, et al.[23] we obtain an estimate for the surface energy of the RhO_2 at 200 °C and 500 mTorr O_2:

$$\alpha = \frac{\gamma_{Rh}}{\gamma_{RhO_2}} \approx \frac{0.1 \text{ eV}}{0.8 \text{ eV}} = 8 \tag{7.9}$$

The molar volumes for Rh and RhO_2 are 8.29 cm^3/mol and 18.74 cm^3/mol, respectively, which allows us to calculate the exponential in Equation (7.8) to obtain:

$$P_{O_2}^{NP} = P_{O_2}^{bulk} \exp\left(-\frac{21\text{ nm}}{r_0}\right) \tag{7.1}$$

7.6 References

(1) Kummer, J. T., *J. Phys. Chem.* **1986,** 90, 4747.

(2) Carrette, L.; Friedrich, K. A.; Stimming, U., *Chemphyschem* **2000,** 1, 162.

(3) Berlowitz, P. J.; Peden, C. H. F.; Goodman, D. W., *J. Phys. Chem.* **1988,** 92, 5213.

(4) Peden, C. H. F.; Goodman, D. W.; Blair, D. S.; Berlowitz, P. J.; Fisher, G. B.; Oh, S. H., *J. Phys. Chem.* **1988,** 92, 1563.

(5) Ackermann, M. D.; Pedersen, T. M.; Hendriksen, B. L. M.; Robach, O.; Bobaru, S. C.; Popa, I.; Quiros, C.; Kim, H.; Hammer, B.; Ferrer, S.; Frenken, J. W. M., *Phys. Rev. Lett.* **2005,** 95, 255505.

(6) Chen, M. S.; Cal, Y.; Yan, Z.; Gath, K. K.; Axnanda, S.; Goodman, D. W., *Surf. Sci.* **2007,** 601, 5326.

(7) Gabasch, H.; Knop-Gericke, A.; Schlogl, R.; Borasio, M.; Weilach, C.; Rupprechter, G.; Penner, S.; Jenewein, B.; Hayek, K.; Klotzer, B., *PCCP* **2007,** 9, 533.

(8) Schalow, T.; Brandt, B.; Starr, D. E.; Laurin, M.; Shaikhutdinov, S. K.; Schauermann, S.; Libuda, J.; Freund, H. J., *PCCP* **2007,** 9, 1347.

(9) Herskowitz, M.; Holliday, R.; Cutlip, M. B.; Kenney, C. N., *J. Catal.* **1982,** 74, 408.

(10) Oh, S. H.; Eickel, C. C., *J. Catal.* **1991,** 128, 526.

(11) Nehasil, V.; Stara, I.; Matolin, V., *Surf. Sci.* **1996,** 352, 305.

(12) Narayanan, R.; El-Sayed, M. A., *J. Am. Chem. Soc.* **2003,** 125, 8340.

(13) Park, J. Y.; Zhang, Y.; Grass, M.; Zhang, T.; Somorjai, G. A., *Nano Lett.* **2008,** 8, 673.

(14) Gong, X. Q.; Liu, Z. P.; Raval, R.; Hu, P., *J. Am. Chem. Soc.* **2004,** 126, 8.

(15) Bluhm, H.; Andersson, K.; Araki, T.; Benzerara, K.; Brown, G. E.; Dynes, J. J.; Ghosal, S.; Gilles, M. K.; Hansen, H. C.; Hemminger, J. C.; Hitchcock, A. P.; Ketteler, G.; Kilcoyne, A. L. D.; Kneedler, E.; Lawrence, J. R.; Leppard, G. G.; Majzlam, J.; Mun, B. S.; Myneni, S. C. B.; Nilsson, A.; Ogasawara, H.; Ogletree, D. F.; Pecher, K.; Salmeron, M.; Shuh, D. K.; Tonner, B.; Tyliszczak, T.; Warwick, T.; Yoon, T. H., *J. Electron. Spectrosc. Relat. Phenom.* **2006,** 150, 86.

(16) Zhang, Y.; Grass, M. E.; Kuhn, J. N.; Tao, F.; Habas, S. E.; Huang, W.; Yang, P.; Somorjai, G. A., *J. Am. Chem. Soc.* **2008,** 130, 5868.

(17) Beamson, G.; Briggs, D., *High Resolution XPS of Organic Polymers: The Scienta ESCA300 Database*. John Wiley & Sons: New York, 1992; p 295.

(18) Mason, M. G., *Phys. Rev. B* **1983,** 27, 748.

(19) Liu, H. J.; Mun, B. S.; Thornton, G.; Isaacs, S. R.; Shon, Y. S.; Ogletree, D. F.; Salmeron, M., *Phys. Rev. B* **2005,** 72,

(20) Zhang, Y. W.; Grass, M. E.; Habas, S. E.; Tao, F.; Zhang, T. F.; Yang, P. D.; Somorjai, G. A., *J. Phys. Chem. C* **2007,** 111, 12243.

(21) Powell, C. J.; Jablonski, A. *NIST Electron Inelastic-Mean-Free-Path Database*, 1.1; National Institute of Standards and Technology: Gaithersburg, MD, 2000.

(22) Gustafson, J.; Mikkelsen, A.; Borg, M.; Lundgren, E.; Kohler, L.; Kresse, G.; Schmid, M.; Varga, P.; Yuhara, J.; Torrelles, X.; Quiros, C.; Andersen, J. N., *Phys. Rev. Lett.* **2004,** 92, 126102.

(23) Kohler, L.; Kresse, G.; Schmid, M.; Lundgren, E.; Gustafson, J.; Mikkelsen, A.; Borg, M.; Yuhara, J.; Andersen, J. N.; Marsman, M.; Varga, P., *Phys. Rev. Lett.* **2004,** 93, 035406.

(24) Campbell, C. T., *Phys. Rev. Lett.* **2006,** 96, 066106.

(25) Falsig, H.; Hvolbæk, B.; Kristensen, Iben S.; Jiang, T.; Bligaard, T.; Christensen, Claus H.; Nørskov, Jens K., *Angew. Chem. Int. Ed.* **2008,** 47, 4835.

(26) Reuter, K.; Scheffler, M., *Phys. Rev. B* **2002,** 65,

Chapter 8: Colloidally synthesized monodisperse Rh nanoparticles supported on SBA-15 for size- and pretreatment-dependent studies of CO oxidation

CO oxidation by O_2 at 40 Torr CO and 100 Torr O_2 has been investigated over a series of colloidally prepared, PVP stabilized Rh nanoparticles supported on mesoporous silica SBA-15. The Rh nanoparticles studied are 1.9, 2.4, 3.6, 5.1, 6.7, and 11.3 nm with a particle size distribution less than 10% for all samples. The turnover frequency at 443 K increases from 0.4 to 1.7 s^{-1} as the particle size decreases from 11.3 to 1.9 nm. Following a high temperature O_2 calcination and H_2 reduction, however, the turnover frequency is ~ 0.25 for all catalysts independent of particle size. The activation for all catalysts is ~ 30 kcal/mol independent of particle size. We have used infrared spectroscopy of CO adsorbed on the Rh nanoparticles to understand the treatment influenced particle size dependence for CO oxidation over PVP stabilized Rh nanoparticles. The observation of a ligand-induced particle size effect for colloidally synthesized transition metal nanoparticles may open a new possibility for the tailoring of metal catalysts using solution nanoparticle synthesis methods.

8.1. Introduction

A new class of catalysts has been developed over the past twenty years involving synthesis of metal nanoparticles by colloidal methods.[1] Many studies have been undertaken to understand the catalytic properties of noble metal nanoparticles (NPs) stabilized by poly(vinylpyrrolidone) (PVP) in solution and/or after deposition onto a solid support.[2-15] One of the advantages of this method of catalyst preparation that is often cited is the control of particle size that can be achieved using this method. Colloidal routes to the formation of nanoparticles for supported catalysts give rise to a much narrower particle size distribution (PSD) than for nanoparticles formed by traditional catalyst preparation methods, such as wetness impregnation or ion exchange. In fact, these methods of catalyst preparation often result in the formation of isolated metal atoms or small clusters on the support, which would not be observed in TEM analysis. In addition to enhanced size control that these systems offer, an important question arises: what is the effect of PVP (or other organic stabilizers) on catalytic performance? This question has been addressed by a few studies regarding solution phase catalysis[11, 16] and our group has studied the interaction of PVP with supported Pt and Rh NPs in the gas phase.[17, 18] The decomposition of PVP on Pt NPs in N_2 has also been studied,[19] but its effect on catalytic properties in gas phase reactions is not understood.

There a limited number of studies involving the use of PVP protected metal nanoparticles supported on oxides for gas phase catalysis. Our group has used PVP protected Pt nanoparticles for hydrogenation reactions after a high temperature oxygen pretreatment and assumed that the PVP was completely removed during the pretreatment.[9, 20] Venezia, *et al.* studied PVP protected Au/Pd bimetallic NPs supported

on SiO_2 for CO oxidation and claim that calcination at 673 K in air completely removed PVP.[12] Einaga, *et al.* immobilized PVP stabilized Pt NPs on TiO_2 and also calcined in O_2 at 673 K to remove PVP. IR spectroscopy of the catalysts during the calcination treatment indicate that the C=O stretch of PVP is greatly diminished by calcination at 673 K, but it is impossible to ensure complete removal because of the lack of sensitivity for IR and an overlapping band from adsorbed water.[21] Our group has also studied similar PVP protected Pt nanoparticles with no high temperature pretreatment (such that PVP is certainly still mostly intact) and found no deleterious effect for the turnover frequency of ethylene hydrogenation.[22, 23] Ma, *et al.* compared various Pt/zeolite catalysts with and without PVP for conversion of methane to higher hydrocarbons and found that PVP had little effect on catalytic performance, but did electronically shield the Pt NPs from the support, as evidenced by X-ray photoelectron spectroscopy (XPS).[24] It is clear from numerous studies that PVP does not completely block catalytic activity in gas phase reactions, but its role in modifying catalytic activity has not been adequately examined.

For this investigation, we have prepared a series of PVP stabilized Rh NPs with sizes of 1.9, 2.4, 3.6, 5.1, 6.7, and 11.3 nm[25, 26] and supported them on mesoporous silica SBA-15 by nanoparticle encapsulation.[20] Using these catalysts, we studied CO oxidation in excess O_2 as a function of particle size and catalyst pretreatment. The role of pretreatment in the particle size dependence of CO oxidation is unexpected and we have analyzed this result using infrared spectroscopy.

CO oxidation is a well studied reaction with many investigations on Rh catalysts, including on single crystals,[27-31] supported catalysts,[31-39] and model NP catalysts in which Rh NPs are supported on a flat oxide substrate.[40-44] The dependence of the rate of CO

oxidation on the size of Rh NPs is somewhat unclear. This is partly due to the fact that many studies of CO oxidation have been performed under widely varying conditions and using samples with very different synthetic conditions. In two studies of CO desorption from model Rh NP catalysts, it was found that CO desorbs at a lower temperature from smaller NPs.[40, 43] When the same study was performed over Pt particles, the opposite trend was observed with a much stronger dependence on particle size.[40] CO oxidation at low pressures over O-precovered Rh surfaces is structure sensitive, with Rh(100) being more active than Rh(111)[29] and smaller particles being more active than larger particles.[42] At higher pressures, steady state measurements of CO oxidation in a 1:1 mixture of CO and O_2 demonstrated no particle size dependence or structure sensitivity over single crystal Rh.[31, 36, 37] The presence or absence of a particle size dependence for CO oxidation over Rh may be an indication of the surface structure of the Rh NPs

In this investigation we compare a series of SBA-15 supported Rh NPs for CO oxidation activity in order to further understand both the NP size dependence of CO oxidation and the role of PVP in affecting gas phase catalytic reactions over Rh catalysts.

8.2. Experimental

8.2.1 Synthesis and Characterization of Rh Nanocrystals

Rhodium(III) acetylacetonate, 1,4-butanediol (99%; bp 503 K), poly(vinylpyrrolidone) (PVP, *M*w = 55,000), and sodium citrate were purchased from Sigma-Aldrich. All solvents, including acetone, ethanol, and hexane, were of analytical grade and were used without further purification. 1,4-butanediol was dried with a molecular sieve for at least two days before use to reduce water contamination.

A series of Rh nanoparticles (NPs) in the range of 1.9 – 11.3 nm were synthesized following the one-step polyol synthesis method described in earlier publications.[25, 26] The sizes of Rh NPs were controlled by changing the concentrations of $Rh(acac)_3$ and sodium citrate. Smaller sized Rh NPs (1.9, 2.4, 3.6, and 5.1 nm) were synthesized in the presence of sodium citrate; larger NPs (6.7 and 11.3 nm) were prepared without the use of sodium citrate.

For the synthesis of Rh(1.9 nm), 80.0 mg of $Rh(acac)_3$, 222 mg of PVP, and 58.8 mg of sodium citrate (2 mmol) were added to 40 mL of 1,4-butanediol in a 100 mL three-necked flask at room temperature. The reaction mixture was heated to 413 K under vacuum, and was further evacuated at this temperature for 20 min to remove water and oxygen with magnetic stirring. The mixture was then heated to 493 K at a rate of 10 K min^{-1} and maintained at this temperature for 2 h under Ar.

When the reaction was complete, an excess of acetone was added at room temperature to form a cloudy black suspension. This suspension was separated by centrifugation at 4200 rpm for 6 min, and the black product was collected by discarding the colorless supernatant. The precipitated Rh NPs were washed with acetone once and then redispersed in ethanol.

Table 8.1: Synthetic conditions for Rh nanocrystals

Sample	$Rh(acac)_3$ (mM)	PVP, 55K (mM)	Na Citrate (mM)	Butanediol (mL)	Final Temp (K)	TEM Size (nm)
Rh(1.9 nm)	5	50	15	40	493	1.9 ± 0.3
Rh(1.9 nm)a	5	50	5	40	493	1.9 ± 0.3
Rh(2.4 nm)	5	50	1.25	40	493	2.4 ± 0.4
Rh(3.6 nm)	5	50	0.5	40	493	3.6 ± 0.6
Rh(5.1 nm)	5	50	0.25	40	493	5.1 ± 0.7
Rh(6.7 nm)	1.25	12.5	0	120	498	6.7 ± 0.7
Rh(11.3 nm)	5	50	0	40	478	11.3 ± 1.6

The other Rh NPs were synthesized using the same protocol, but with varying reagent concentrations and temperatures. The experimental conditions and sizes of Rh NPs are summarized in Table 8.1.

The nanoparticle sizes were analyzed using a Philips FEI Tecnai 12 transmission electron microscope (TEM) operated at 100 kV. X-ray diffraction (XRD) patterns were recorded on a Bruker D8 GADDS diffractometer using Co Kα radiation (λ = 1.79 Å).

8.2.2 Catalyst Synthesis and Characterization

Pluronic P123 (EO20PO70EO20, BASF), tetramethyl orthosilicate (TMOS, 98%, Aldrich), and sodium fluoride (99.99%, Aldrich) were used as received.

The Rh(*X*)/SBA-15 catalysts (*X* = 1.9, 2.4, 3.6, 5.1, 6.7, or 11.3 nm) were synthesized by nanoparticle encapsulation (NE).[20] 2.5 g of Pluronic P123 was completely dissolved in 50.5 mL of deionized water (DI) and the Rh NP colloids dispersed in aqueous solution (27.0 mL, 5.93 mM based on total Rh) were mixed with the P123 solution and stirred for 1 h at 313 K. To this solution 0.375 mL of 0.5 M aqueous NaF and 3.91 mL TMOS were quickly added to the reaction mixture, followed by stirring for 20 h at 313 K. The reaction mixture was further aged for 24 h at 373 K in a closed vessel. The precipitates were separated by centrifugation, thoroughly washed with DI and ethanol, and dried at room temperature for 2 days. The resulting samples were designated as Rh(*X*)/SBA-15, where *X* denotes the particle size in nm of the Rh NPs. In order to test the effect of high temperature O_2 calcination, a fraction of each sample was pretreated in O_2 at 100 mL min^{-1}. Rh(1.9 nm)/SBA-15 and Rh(2.4 nm)/SBA-15 samples were calcined at 623 K for 24 h, Rh(3.6 nm)/SBA-15 and Rh(5.1 nm)/SBA-15 were calcined at

623 K for 36 h, and Rh(6.7 nm)/SBA-15 and Rh(11.3 nm)/SBA-15 were calcined at 723 K for 36 h. These samples are denoted Rh(*X*)/SBA-15-c.

Both the calcined and uncalcined catalysts were analyzed by TEM and XRD as indicated above. The mesoprorosity and structure of the SBA-15 was investigated using small angle X-ray scattering (SAXS) and nitrogen adsorption at 77 K with a Quantachrome Autosorb 1 automated sorption analyzer. Additionally, the Rh content was determined by inductively coupled plasma optical emission spectroscopy (ICP-OES) (Mikroanalytishes Labor Pascher) and electron probe microanalysis (EPMA).[45] Active metal surface area was determined by room temperature adsorption of H_2 and CO using the Autosorb-1. The uncalcined samples Rh(*X*)/SBA-15 were also characterized using combined thermogravimetric analysis and differential temperature analysis (TGA-DTA; TA Instruments SDT 2960) by heating from room temperature to 1273 K at a rate of 10 K min^{-1} in a flow of pure O_2 at 100 mL min^{-1}.

8.2.3 CO Oxidation Measurements

Catalytic measurements were carried out in a home built Pyrex reaction system operated as a plug flow reactor.[9] Flow rates of oxygen (Praxair, 99.995%), carbon monoxide (Praxair, 99.99%), and helium (Praxair, 99.999%) were controlled using mass flow controllers (Porter Instruments) and reactants and products were analyzed by gas chromatography (HP 5890 Series II). In a typical experiment, 20 – 120 mg of catalyst was mixed with acid washed and calcined quartz and loaded into the reactor. The reacter was purged with He and the catalyst was heated to 373 in flowing He for 1 h, then a total flow rate of 80 mL min^{-1} with 40 Torr CO, 100 Torr O_2, and a background of He was established at room temperature and the sample was then heated to reaction temperatures

(403 – 503 K). For the calcined samples, an in situ 1 hr reduction in 100 Torr H_2 in He at 623 K preceded the reaction studies.

8.2.4 Diffuse Reflectance Infrared Spectroscopy of CO on Rh/SBA-15

Diffuse reflectance FTIR spectroscopy (DRIFTS) was used to investigate the adsorption of CO to the Rh(*X*)/SBA-15 catalysts as-synthesized, after calcination, and following a subsequent reduction in H_2 at 573 K. Experiments were conducted with a Nicolet Nexus 670 spectrometer equipped with a Thermo Spectra-Tech controlled atmosphere-diffuse reflectance cell. For studies of as-synthesized samples (Rh(*X*)/SBA-15), ~ 7 mg of sample was loaded into the diffuse reflectance cell and purged at 393 K in N_2 (80 mL min^{-1}) to remove gas-phase and weakly bound water. The samples were cooled, then exposed to 1% CO/He (30 mL min^{-1}) for 5 min and the cell was then purged with N_2 for 15 min. Reported spectra of CO exposed catalysts are after subtraction of spectra before CO exposure. For the study of calcined samples (Rh(*X*)/SBA-15-c), the calcination was performed *ex situ* as described above, and the sample was treated in the same way as the as-synthesized samples in the DRIFTS cell. For reduced samples, an *in situ* reduction was carried out on Rh(*X*)/SBA-15-c at 593 K in 10% H_2/He (30 sccm) for 1 h followed by a 30 min purge in N_2 (80 sccm) at the same temperature following the initial N_2 purge and before exposure to CO. All spectra are an average of 256 scans at 4 cm^{-1} resolution.

8.3. Results and Discussion

8.3.1 Synthesis and Characterization of Rh Nanoparticles

The synthesis and characterization of Rh NPs in the size range 5.4 – 13.5 nm[25] and the synthesis of Rh NPs below 5 nm have been previously reported.[26] TEM images

(Figure 8.1) and XRD patterns (Figure 8.2) for these samples are consistent with our previous work, although the exact particle size from a given preparation varies somewhat. The final column of Table 8.1 lists the particle sizes and standard deviation from an analysis of 100 particles via TEM. The XRD patterns show a broadening of the peaks along with a shift to lower 2θ, consistent with the Scherer equation and a relaxation of the Rh-Rh bond distance in smaller particles. This relaxation is 5% from Rh(11.3 nm) to Rh(1.9 nm). The measured crystallite size by the Scherer equation is smaller than the particle size observed by TEM, which is expected because a significant fraction of the particles are not single crystalline, but {111} twinned particles.

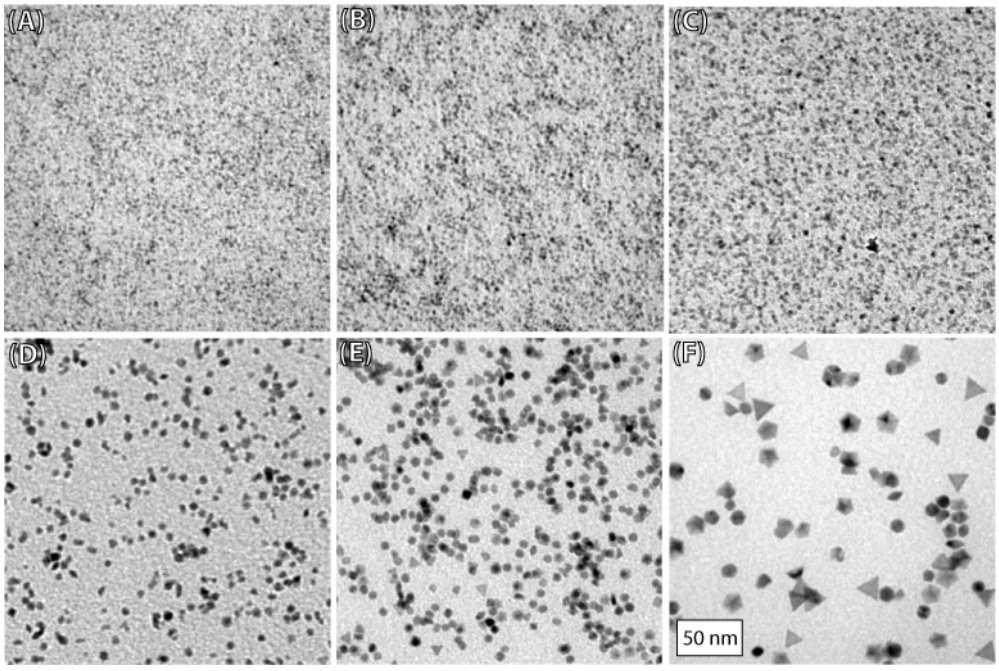

Figure 8.1. TEM images of (A) Rh(1.9 nm), (B) Rh(2.4 nm), (C) Rh(3.6 nm), (D) Rh(5.1 nm), (E) Rh(6.7 nm), and (F) Rh(11.3 nm). The large (> 5 nm) particles show well defined facets. The scale for all images is the same.

8.3.2 Synthesis and Characterization of Rh/SBA-15 Catalysts

The Rh/SBA-15 catalysts have been characterized by elemental analysis, XRD, TEM, TGA, and H_2 and CO chemisorption. Elemental analysis and TEM were

performed after the samples were calcined, XRD was measured before and after calcination, and chemisorption was performed after calcination and an *in situ* reduction. Table 8.2 contains a summary of the calcination protocols for all samples, the Rh loading by ICP-OES,[45] and EPMA, and H/Pt and CO/Pt from H_2 and CO chemisorption. All samples were prepared with a nominal loading of 1% Rh by weight assuming 100% yield for the synthesis of the NPs and full incorporation of the NPs in the preparation of the catalysts. The Rh loading data indicates that the overall yield for the NP synthesis and encapsulation is 50 – 90% with a typical preparation having ~ 80% yield. There are not many reports of yield for nanoparticle syntheses in the literature, so it is not clear if this is typical for a polyol synthesis, though it is consistent with our previous work with Pt NPs.[20]

Table 8.2: Characterization of Rh in calcined catalysts

Sample	Calcination Procedure	% Rh (ICP-OES)	% Rh (EPMA)	H/Rh	CO/Rh	Theoretical Dispersion (TEM)
Rh(1.9 nm)/SBA-15-c	24 h, 623 K	0.73	.79	0.49	0.29	0.65
Rh(1.9 nm)a/SBA-15-c	24 h, 623 K	0.78	.85	0.49	0.31	0.65
Rh(2.4 nm)/SBA-15-c	24 h, 623 K	0.78	.87	0.48	0.29	0.51
Rh(3.6 nm)/SBA-15-c	24 h, 723 K	0.77	.82	0.23	0.11	0.34
Rh(5.1 nm)/SBA-15-c	24 h, 723 K	0.53	.57	0.13	0.02	0.24
Rh(6.7 nm)/SBA-15-c	36 h, 723 K	0.84	.88	0.16	0.03	0.18
Rh(11.3 nm)/SBA-15-c	36 h, 723 K	0.82	.85	0.31	0.04	0.11

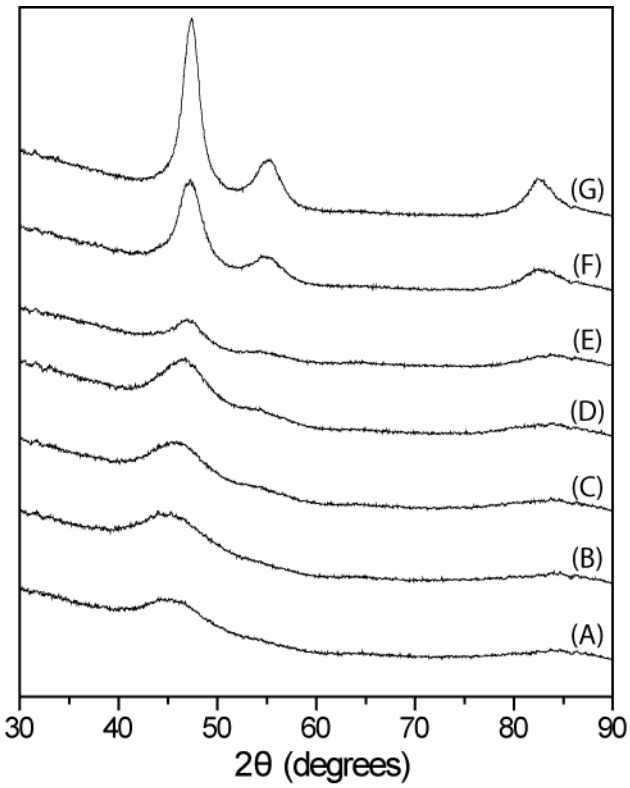

Figure 8.2. X-ray diffractograms of (A) Rh(1.9 nm), (B) Rh(1.9 nm)a, (C) Rh(2.4 nm), (D) Rh(3.6 nm), (E) Rh(5.1 nm), (F) Rh(6.7 nm), and (G) Rh(11.3 nm). The 111 diffraction peak broadens as the particle size decreases, consistent with the Scherrer equation. For the smallest particles, only the 111 reflection is intense enough to observe.

TEM analysis of Rh(*X*)/SBA-15-c (Figure 8.3) reveals that the NPs do not aggregate in the nanoparticle encapsulation or calcination procedures, but the larger particles do tend to deposit in the support as clusters of particles, as previously observed.[22] A particle size distribution analysis of the Rh(*X*)/SBA-15 catalysts is consistent with the particle size distribution obtained for the as-synthesized NPs before encapsulation.

XRD peaks are only observed for samples with larger NPs and thus sharper diffraction peaks (Rh(6.7 nm)/SBA-15, Rh(11.3 nm)/SBA-15) after encapsulation in SBA-15. The diffraction peaks appear at the same position and have the same FWHM as

for the as-synthesized particles, but completely disappear for all samples after calcination without a subsequent reduction (Figure 8.4). It appears that the calcination protocol (Table 8.2) causes oxidation of the Rh NPs and formation of an amorphous Rh oxide, as no diffraction peaks from the oxide are observed. After reduction in H_2 at 673 K for 1 h followed by CO oxidation at ~ 473 K, the diffraction peaks are restored, indicating that the particles reduce under those conditions. The oxidation state of the Rh NPs during reaction was the subject of a previous study.[26]

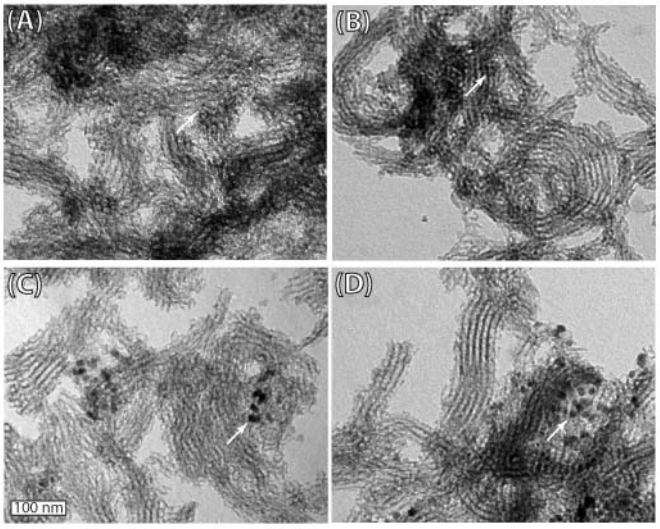

Figure 8.3. TEM images of calcined Rh nanoparticle catalysts, (A) Rh(1.9 nm)/SBA-15-c, (B) Rh(2.4 nm)/SBA-15-c, (C)Rh(6.7 nm)/SBA-15-c, and (D)Rh(11.3 nm)/SBA-15-c. While the particles tend to bunch together in certain regions, the particles do not agglomerate even after the high temperature calcination. The arrows indicate the location of a Rh NP on the SBA-15 support.

The weight loss of the as-synthesized catalysts was analyzed in air by TGA-DTA (Figure 8.5). At low temperatures (< 373 K), there is an initial weight loss of ~ 4% corresponding to the loss of water and volatile organic compounds, such as ethanol used for washing. A second weight loss event begins at ~ 438 K and corresponds to combustion of the templating surfactant, P123. This weight loss accounts for an

additional 16 – 18% mass loss and is accompanied by an exotherm at the onset (near 438 K). The temperature of the blank SBA-15 and all Rh(*X*)/SBA-15 samples except Rh(11.3)/SBA increases by < 1 K relative to an inert reference and the weight loss profiles are similar to those shown in Figure 8.5 for Rh(1.9 nm)/SBA-15 and Rh(5.1 nm)/SBA-15. The one exception is Rh(11.3 nm)/SBA-15: both the TGA and DTA plots for this sample are distinctly different. In that case, the second weight loss event begins at ~ 438 K and the weight loss is extremely rapid and accompanied by a 35 K exotherm. The main difference between this sample and the others is that the NPs are larger than the size of the mesopores of the support (~ 8 nm). It is thus possible that the particles block the pores and the initial combustion thus generates a pressure buildup and subsequent exotherm and rapid, enhanced combustion of the remaining surfactant. It is not clear what affect this has on the mesopores or the Rh particles in terms of their final orientation, but no evidence for particle or support degradation can be seen in TEM images or the N_2 adsorption isotherms of the calcined samples. We have observed a similar phenomenon for Pt(9.1)/SBA catalysts during temperature programmed reduction and further study of this process may be warranted.

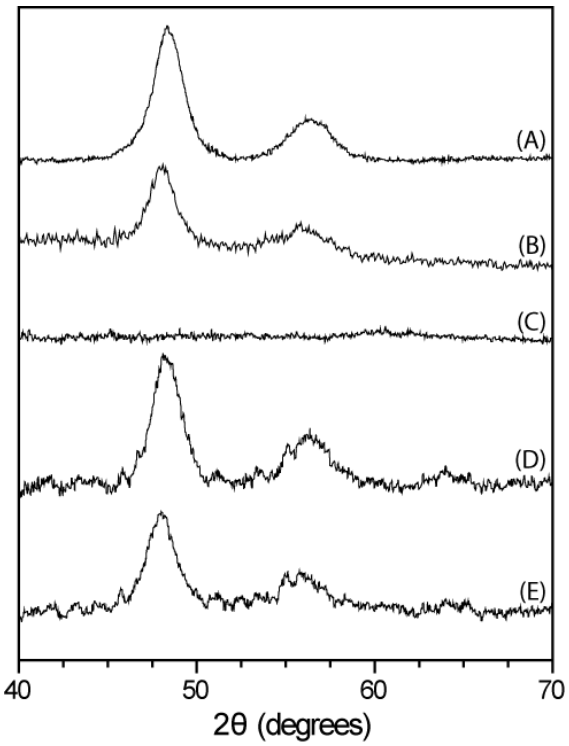

Figure 8.4. X-ray diffractograms of (A) Rh(11.3 nm), (B) Rh(11.3 nm)/SBA-15, (C) Rh(11.3 nm)/SBA-15-c, (D) Rh(11.3 nm)/SBA-15 after CO oxidation, and (E) Rh(11.3 nm)/SBA/-15-c after CO oxidation indicate that the structure of the Rh(11.3 nm) nanoparticles is maintained after encapsulation, but calcination results in the formation of an amorphous Rh oxide. The Rh fcc structure is again observed upon subsequent reduction or reaction.

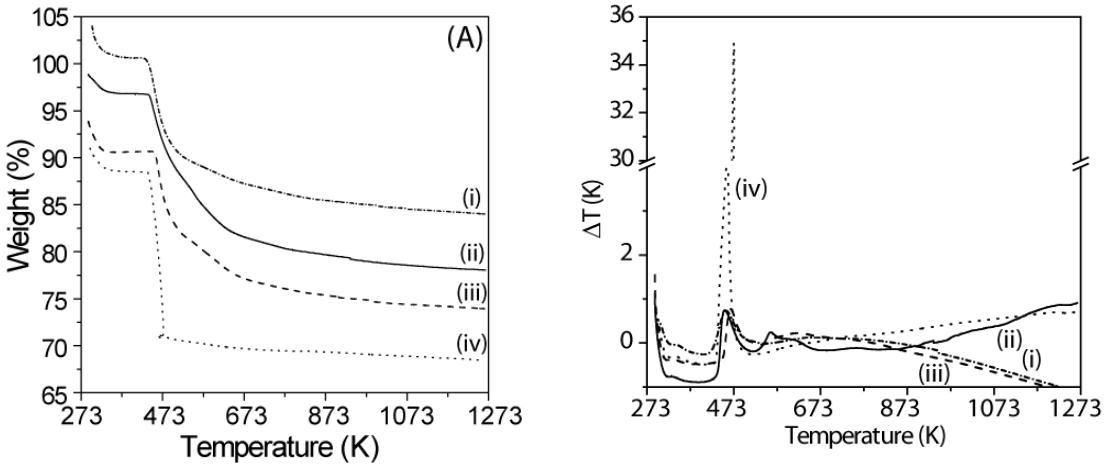

Figure 8.5. Combined (A) thermogravimetric analysis and (B) differential thermal analysis of (i) SBA-15, (ii) Rh(1.9 nm)/SBA-15, (iii) Rh(5.1 nm)/SBA-15, and (iv) Rh(11.3 nm)/SBA-15. The major weight loss (~15% of total weight) is due to decomposition of the templating surfactant and is similar for pure SBA-15 and for Rh(*X*)/SBA-15 with the notable exception of Rh(11.3 nm)/SBA-15.

8.3.3 CO Oxidation

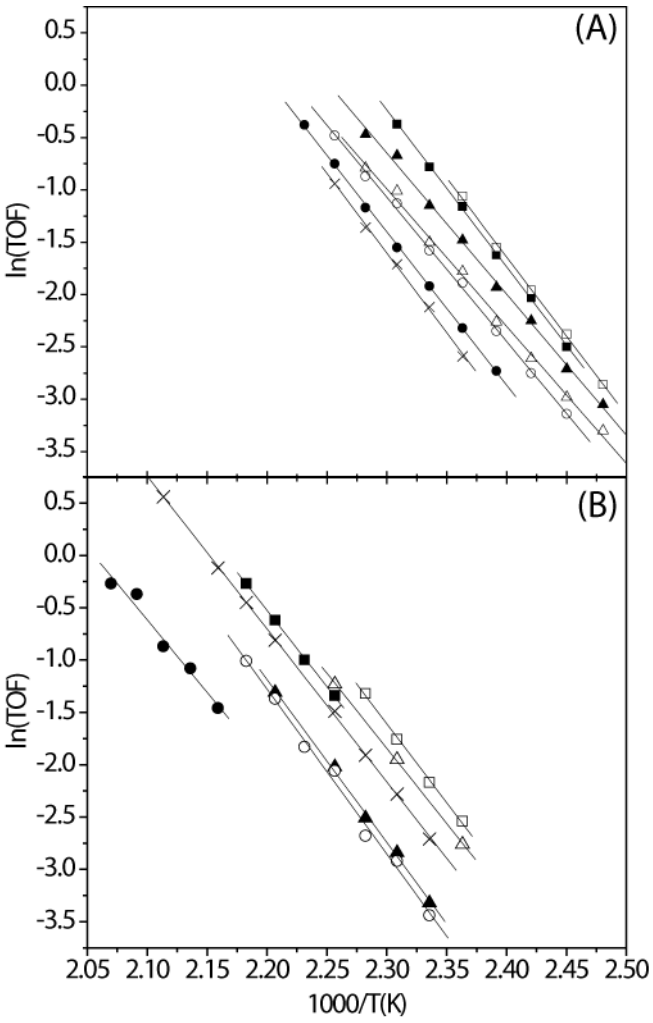

Figure 8.6. Arrhenius plots for (A) Rh(*X*)/SBA-15 and (B) Rh(*X*)/SBA-15-c, *X* = 1.9 nm (■), 1.9 nm(a) (□), 2.4 nm (▲), 3.6 nm (Δ), 5.1 nm (●), 6.7 nm (○), and 11.3 nm (×). The overall rate of reaction is higher for the uncalcined samples, Rh(*X*)/SBA-15 series of catalysts. The activation energy for all samples is similar. The partial pressures of the reactants are 40 Torr CO and 100 Torr O_2.

All catalysts were tested for CO oxidation activity at pressures of 40 Torr CO and 100 Torr O_2 and at temperatures below the ignition temperature, which ranged between 440 and 500 K depending on the catalyst and the amount loaded. Arrhenius plots for CO oxidation are shown in Figure 8.6 and the apparent activation energy and TOF at 443 K

are summarized in Table 8.3. A few general trends are readily observed. The activation energy for CO oxidation is ~ 30 kcal mol^{-1} for each catalyst and there is no trend in the activation energy as a function of either particle size or pretreatment. The CO and O_2 reaction orders were tested for selected catalysts (not shown) and agreed with literature steady state measurements taken at similar pressures and temperatures – the reaction orders were approximately +1 in O_2 and –1 in CO.

Table 8.3: Summary of catalytic results for CO oxidation

Sample	Apparent E_a (kcal/mol)[a]		TOF (s^{-1})[b]	
	Uncalcined	Calcined	Uncalcined	Calcined
Rh foil	–	–	0.035	
Rh(1.9 nm)/SBA-15	29.8 ± 0.3	28.8 ± 0.6	1.52	0.26
Rh(1.9 nm)a/SBA-15	30.0 ± 0.6	30.0 ± 1.0	1.69	0.38
Rh(2.4 nm)/SBA-15	26.8 ± 0.4	31.8 ± 1.6	0.94	0.13
Rh(3.6 nm)/SBA-15	26.1 ± 0.7	28.6 ± 0.5	0.65	0.30
Rh(5.1 nm)/SBA-15	29.1 ± 0.3	27.4 ± 2.7	0.47	0.06
Rh(6.7 nm)/SBA-15	27.4 ± 0.4	31.3 ± 1.2	0.63	0.11
Rh(11.3 nm)/SBA-15	30.2 ± 0.7	28.7 ± 0.2	0.39	0.22

[a] Determined at 40 Torr CO, 100 Torr O_2, 423 – 523 K

[b] Determined at 40 Torr CO, 100 Torr O_2, 443 K and calculating the number of surface sites from TEM and ICP-OES.

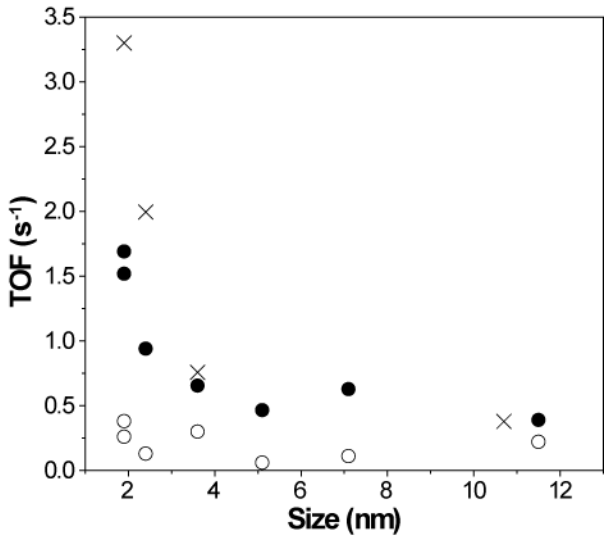

Figure 8.7. Turnover frequency as a function of particle size for Rh(*X*)/SBA-15 (●), Rh(*X*)/SBA-15-c (○), and Rh(*X*) as a 2 dimensional film on a silicon wafer (×).[26] The reaction conditions are 443 K, 40 Torr CO, and 100 Torr O_2.

From the TOF at 443 K listed in Table 8.3 and shown graphically is Figure 8.7, a few clear trends emerge. First, the entire set of catalysts exhibit higher turnover than Rh foil measured at the same pressures of O_2 and CO in the same reactor. Additionally, the uncalcined samples (Rh(*X*)/SBA-15) are more active than the calcined samples (Rh(*X*)/SBA-15-c). The TOF for Rh(11.3 nm)/SBA-15 decreases by a factor of 1.8 upon calcination and all other catalysts suffer a loss in specific activity greater than this. The largest decrease in TOF is found for Rh(2.4 nm)/SBA-15, for which the TOF decreases by a factor of 7.3, from 1.69 s^{-1} to 0.38 s^{-1} at 443 K (Table 8.3). The decrease in catalytic activity after calcination and reduction is discussed further in light of IR spectroscopy investigations of CO adsorbed on these catalysts in section 3.5.

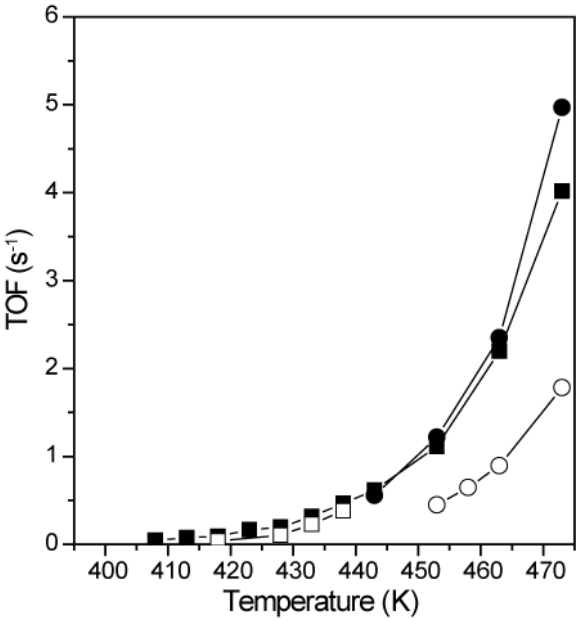

Figure 8.8. CO oxidation TOF for Rh(11.3 nm)/SBA-15 when first placed into the reactor (■) and after 5 h reaction at 473 K (●), and also Rh(11.3 nm)/SBA-15-c when first placed into the reactor (□) and after 5 h reaction at 473 K (○). The uncalcined samples do not deactivate, while the calcined sample do. The reaction pressures are 40 Torr CO, and 100 Torr O_2.

The TOF increases monotonically with decreasing particle size from 0.39 s^{-1} for Rh(11.3 nm)/SBA-15 to 1.69 s^{-1} for Rh(1.9)a/SBA-15 for the catalysts that have not been calcined. This increase is demonstrated in an Arrhenius plot in Figure 8.6(A) and also in Figure 8.7. The particle size dependence observed for these catalysts is similar to the trend we observed in a previous study of similar NPs, which were deposited onto silicon wafers by Langmuir-Blodgett deposition.[26] In that work, we also observed that smaller particles are more facilely oxidized during CO oxidation and attributed the observed size dependent TOF to this phenomenon. An increase in activity for CO oxidation with decreasing particle size for Pd NPs has recently been reported by Chen, *et al.* and was also attributed to the fact that smaller NPs oxidize more easily.[46]

The initial deactivation of Rh(*X*)/SBA-15 and Rh(*X*)/SBA-15-c was examined and is shown in Figure 8.8. A fresh Rh(11.3 nm)/SBA-15 catalyst was placed in the reactor, purged with He at 373 K, then heated to 408 K in the presence of CO and O_2 as described above. The reaction temperature was increased in steps of either 5 or 10 K to 473 K, then the catalyst was cooled to 443 K and the reaction rate was measured in steps of 10 K again. At all temperatures, the reaction rate was stable and no deactivation was observed. The same experiment was repeated for the case of Rh(11.3 nm)/SBA-15-c. The calcined catalyst was first reduced in a flow of 100 Torr H_2 at 623 K, then purged with He and cooled to 408 K for the start of the reaction. The reaction rate was monitored as the catalyst was heated in steps, but deactivation was observed at temperatures above 438 K. At this stage, the catalyst was heated to 473 K and the reaction was monitored until a steady state rate was observed and reaction rates were measured between 453 and 473 K. From Figure 8.8, it is clear that a large degree of deactivation occurs for the calcined

sample, but not for the uncalcined sample. This calcination dependent deactivation is not currently understood, but may be the result of the formation of a "bulk-like" oxide during reaction at higher temperatures. While surface oxides or chemisorbed oxygen on metal surfaces are quite active for reaction with CO, the "bulk-like" oxides are stable and not reactive towards CO.[47]

8.3.4 Diffuse Reflectance Infrared Spectroscopy

In order to explore the change in particle size dependence observed for samples before and after high temperature calcination, we have studied the adsorption of CO on the NP surfaces before calcination, after calcination, and after calcination followed by *in situ* reduction. After pretreatment (if any) and an initial purging with N_2, the sample was exposed to CO at room temperature, and then evacuated and spectra were recorded. For the as-synthesized samples, peaks at ~1900 and ~2025 cm^{-1} are clearly observed (Figure 8.8). After calcination, these peaks disappear and are replaced by peaks at ~2070 and ~2100 cm^{-1}. After reduction in H_2 at 693 K, only the peak at ~2070 cm^{-1} remains. The peaks at ~1900 and ~2025 cm^{-1} on the freshly synthesized catalysts are attributed to bridge bonded CO on Rh of oxidation state 0 and 1, respectively. The peaks observed after calcination can similarly be attributed to linearly bound CO to Rh of oxidation state 0 (~2070 cm^{-1}) or 1 (~2100 cm^{-1}) and after reduction only linear bound CO on zero valent Rh is present.[48-54] This change in available binding sites in schematically represented in Figure 8.9(A).

One interesting discrepancy between these samples and conventionally prepared Rh/SiO_2 or Rh/Al_2O_3 catalysts is that the CO peaks observed are drastically different. For conventionally prepared catalysts, bridge and atop CO are observed, but also peaks at

~2100 and ~2025 cm^{-1} corresponding to the antisymmetric and symmetric stretches of rhodium gem-dicarbonyl for which two CO molecules are adsorbed to a single Rh(I) atom. This type of CO adsorption occurs only on isolated Rh atoms (not Rh atoms of NPs). The absence of these peaks in any of our spectra attest to the fact that all Rh exists on the support in NP form without any isolated Rh atoms. Such an observation strengthens the argument that colloidal synthesis produces NPs with low PSD: atomically dispersed Rh is absent from these catalysts.

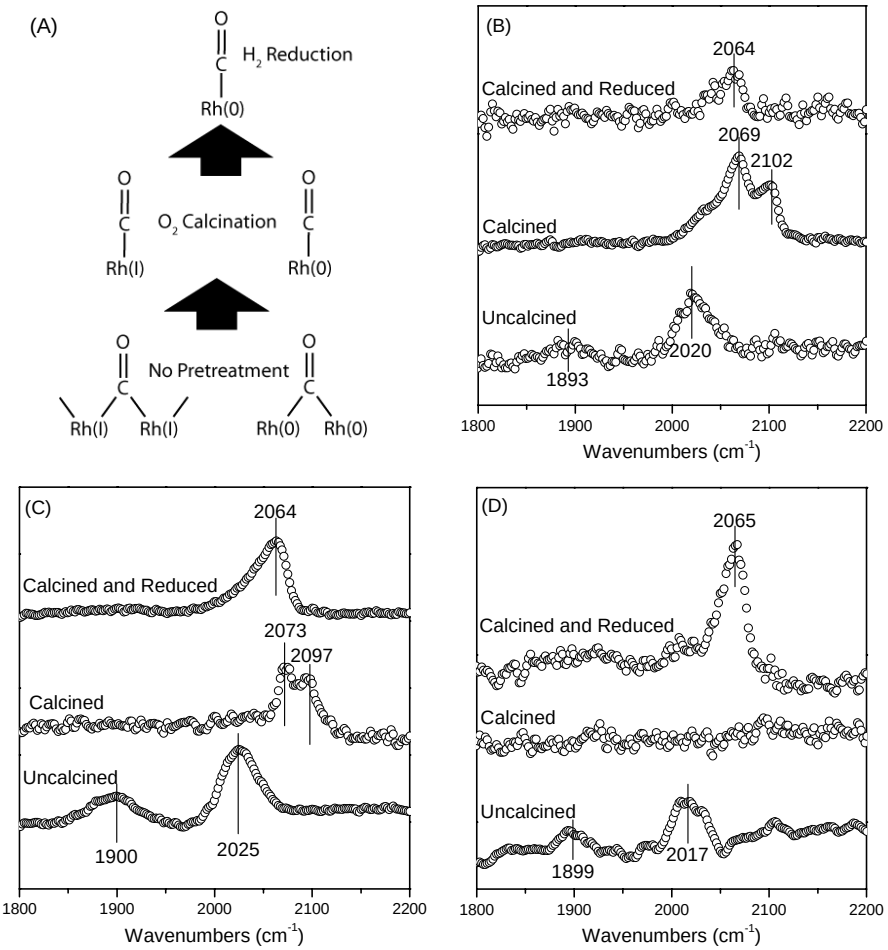

Figure 8.9. DRIFTS of CO adsorbed on the Rh catalysts with (A) a schematic of the binding of CO to Rh after different pretreatments, and infrared spectra of CO at room temperature on (B) Rh(1.9 nm)a/SBA-15, (C) Rh(2.4 nm)/SBA-15, and (D) Rh(6.7 nm)/SBA-15.

8.3.5 Comparison of Infrared Results and Catalytic Activity

In the series of studies that we have performed on this set of Rh NPs, the size dependence appears to be lost after a high temperature O_2 treatment followed by high temperature H_2 treatment. No change in particle size was observed by TEM after calcination (Figure 8.3), which leads us to speculate that the change is a result of decomposition of the stabilizing polymer PVP and/or the templating surfactant P123. It is difficult to characterize the nature of the polymers at the Pt interface because of the large excess of P123 within the support that is not in near proximity with Pt NPs as well as the changes that occur to SBA-15, such as formation or decomposition of surface silanols. Instead, we have used CO as a probe molecule to characterize changes at or near the Pt surface.

We see a clear change in the available adsorption sites on these catalysts after different pretreatments. For the as-synthesized catalysts (no pretreatment), CO preferentially adsorbs to bridge sites on Rh with contribution from adsorption sites in at least two different chemical environments. In previous works, these sites have been attributed to bonding at Rh sites of valence 0 and 1.[52] After calcination in O_2, CO adsorbs solely to atop Rh sites, with both Rh(0) and Rh(I) available. Following *in situ* reduction by H_2, all Rh is converted to Rh(0) and only atop CO on Rh(0) is observed. The major question in this case, of course, is if/how this change in adsorption changes the reaction rate and bestows structure sensitivity to the reaction.

For the calcined and reduced catalysts, it appears that atop CO on Rh(0) sites reacts with surface oxygen in a fashion that is structure insensitive, while the reaction between bridge bound CO and surface oxygen is structure sensitive. Additionally, the

uncalcined samples, on which CO adsorbs at bridge sites, exhibit higher catalytic activity. In this study, the uncalcined samples are most active, followed by the calcined and reduced samples, and the calcined samples without reduction were least active for CO oxidation. *In situ* infrared studies of CO oxidation over supported Rh catalysts have demonstrated that *gem*-dicarbonyl CO species that form on isolated Rh(I) sites are inactive for oxidation by O_2, while atop and bridge CO species are both active.[33, 34, 48] In one study, it was proposed that CO adsorbed at Rh(0) sites is most active,[34] while in another it was proposed to be atop CO adsorbed at Rh(I) sites.[33] In our study, comparing the infrared spectra to CO oxidation results, bridge sites are most active, followed by atop CO adsorbed at Rh(0) sites, followed by atop CO adsorbed at Rh(I) sites.

Using DFT calculations, Gong *et al.* demonstrated that metal oxides are more active for CO oxidation than the corresponding metal surface as a result of the change in adsorption geometry of O adatoms that participate in the reaction. Specifically, they demonstrated that the reaction barrier for atop CO and atop O to react on an oxide surface is lower than the barrier for reaction between atop CO and bridge O on a metallic surface.[55] In our study, it appears that PVP alters the binding geometry of CO to the Rh surface. If O adatoms are adsorbed at bridge sites in both cases, then shifting CO adsorption from atop sites to bridge sites would provide a geometrically advantageous setup for reaction between CO and O adatoms. Constraining CO and O to both adsorb at bridge sites, the reaction barrier will be lowered relative to the case involving atop CO and bridge O because the surface reactants are in a closer confined geometry. The induced structure sensitivity may arise from two different sources. In our previous work, we demonstrated that the smaller PVP capped Rh NPs are more oxidized during CO

oxidation than the larger particles.[26] This increased oxidation may give rise to a larger percentage of more active surfaces (i.e. the more active oxide surface studied by Gong *et al.*). A second possible explanation arises from the infrared spectroscopy presented here. CO adsorbed at bridge sites may be more influenced by the particle size than atop CO, which involves a single surface Rh atom. Distinguishing between these possibilities is beyond the scope of this paper, but ligand-induced structure sensitivity clearly deserves a more thorough examination.

8.4. Conclusions

We have described the synthesis, characterization, and catalytic properties for CO oxidation catalysis of a series of PVP stabilized Rh NPs between 1.9 and 11.3 nm supported on mesoporous SiO_2. The synthesis of Rh NPs of narrow size distribution allows for careful studies of particle size effects in catalysis, but this study demonstrates a complicating, but perhaps useful, issue in the use of colloidally prepared NPs for catalytic applications. Having studied this series of PVP stabilized Rh NP catalysts before and after calcination in O_2 at ~ 673 K, we have concluded that (1) uncalcined PVP stabilized Rh NP catalysts exhibit a higher TOF for CO oxidation than calcined catalysts, (2) CO oxidation TOF increases with decreasing particle size for uncalcined catalysts, but CO oxidation is particle size independent for calcined catalysts, and (3) CO adsorbs at bridge sites before the catalysts are calcined, but on atop sites after calcination, with or without reduction in H_2. By comparing infrared studies to TOF measurements for CO oxidation, we propose that PVP affects how CO binds to Rh and thus affects the TOF for CO oxidation. The presence of intact PVP results in preferential adsorption of CO at bridge

sites, which causes an increase in catalytic activity as well as an observed particle size dependence for CO oxidation.

8.5. References

(1) Aiken, J. D.; Finke, R. G., *J. Mol. Catal. A: Chem.* **1999,** 145, 1.

(2) Gniewek, A.; Trzeciak, A. M.; Ziolkowski, J. J.; Kepinski, L.; Wrzyszcz, J.; Tylus, W., *J. Catal.* **2005,** 229, 332.

(3) Jiang, Y. J.; Gao, Q. M., *J. Am. Chem. Soc.* **2006,** 128, 716.

(4) Li, Y.; Boone, E.; El-Sayed, M. A., *Langmuir* **2002,** 18, 4921.

(5) Li, Y.; Hong, X. M.; Collard, D. M.; El-Sayed, M. A., *Organic Letters* **2000,** 2, 2385.

(6) Narayanan, R.; El-Sayed, M. A., *J. Am. Chem. Soc.* **2003,** 125, 8340.

(7) Pellegatta, J. L.; Blandy, C.; Colliere, V.; Choukroun, R.; Chaudret, B.; Cheng, P.; Philippot, K., *J. Mol. Catal. A: Chem.* **2002,** 178, 55.

(8) Porta, F.; Prati, L.; Rossi, M.; Coluccia, S.; Martra, G., *Catal. Today* **2000,** 61, 165.

(9) Rioux, R. M.; Song, H.; Hoefelmeyer, J. D.; Yang, P.; Somorjai, G. A., *J. Phys. Chem. B* **2005,** 109, 2192.

(10) Shiraishi, Y.; Toshima, N., *J. Mol. Catal. A: Chem.* **1999,** 141, 187.

(11) Stowell, C. A.; Korgel, B. A., *Nano Lett.* **2005,** 5, 1203.

(12) Venezia, A. M.; Liotta, L. F.; Pantaleo, G.; La Parola, V.; Deganello, G.; Beck, A.; Koppany, Z.; Frey, K.; Horvath, D.; Guczi, L., *Appl. Catal. A: Gen.* **2003,** 251, 359.

(13) Wan, B. S.; Liao, S. J.; Xu, Y.; Yu, D. R., *J. Mol. Catal. A: Chem.* **1998,** 136, 263.

(14) Zuo, X. B.; Liu, H. F.; Guo, D. W.; Yang, X. Z., *Tetrahedron* **1999,** 55, 7787.

(15) Lee, H.; Habas, S. E.; Kweskin, S.; Butcher, D.; Somorjai, G. A.; Yang, P., *Angew. Chem. Int. Ed.* **2006,** 45, 7824.

(16) Li, Y.; El-Sayed, M. A., *J. Phys. Chem. B* **2001,** 105, 8938.

(17) Borodko, Y.; Habas, S. E.; Koebel, M.; Yang, P. D.; Frei, H.; Somorjai, G. A., *J. Phys. Chem. B* **2006,** 110, 23052.

(18) Borodko, Y.; Humphrey, S. M.; Tilley, T. D.; Frei, H.; Somorjai, G. A., *J. Phys. Chem. C* **2007,** 111, 6288.

(19) Du, Y. K.; Yang, P.; Mou, Z. G.; Hua, N. P.; Jiang, L., *J. Appl. Poly. Sci.* **2006,** 99, 23.

(20) Song, H.; Rioux, R. M.; Hoefelmeyer, J. D.; Komor, R.; Niesz, K.; Grass, M.; Yang, P. D.; Somorjai, G. A., *J. Am. Chem. Soc.* **2006,** 128, 3027.

(21) Einaga, H.; Harada, M., *Langmuir* **2005,** 21, 2578.

(22) Grass, M. E.; Yue, Y.; Habas, S. E.; Rioux, R. M.; Teall, C. I.; Yang, P.; Somorjai, G. A., *J. Phys. Chem. C* **2008,** 112, 4797.

(23) Rioux, R. M.; Song, H.; Grass, M.; Habas, S.; Niesz, K.; Hoefelmeyer, J. D.; Yang, P.; Somorjai, G. A., *Top. Catal.* **2006,** 39, 167.

(24) Ma, J. H.; Reng, S. H.; Pan, D. H.; Li, R. F.; Xie, K. C., *Reactive & Functional Polymers* **2005,** 62, 31.

(25) Zhang, Y. W.; Grass, M. E.; Habas, S. E.; Tao, F.; Zhang, T. F.; Yang, P. D.; Somorjai, G. A., *J. Phys. Chem. C* **2007,** 111, 12243.

(26) Grass, M.; Zhang, Y.; Butcher, D.; Park, J. Y.; Bluhm, H.; Bratlie, K.; Zhang, T.; Somorjai, G. A., *Submitted* **2008**,

(27) Baraldi, A.; Gregoratti, L.; Comelli, G.; Dhanak, V. R.; Kiskinova, M.; Rosei, R., *Appl. Surf. Sci.* **1996,** 99, 1.

(28) Bowker, M.; Quo, Q.; Li, Y.; Joyner, R. W., *Catal. Lett.* **1993,** 18,

(29) Hopstaken, M. J. P.; Niemantsverdriet, J. W., *J. Chem. Phys.* **2000,** 113, 5457.

(30) Leibsle, F. M.; Murray, P. W.; Francis, S. M.; Thornton, G.; Bowker, M., *Nature* **1993,** 363, 706.

(31) Peden, C. H. F.; Goodman, D. W.; Blair, D. S.; Berlowitz, P. J.; Fisher, G. B.; Oh, S. H., *J. Phys. Chem.* **1988,** 92, 1563.

(32) Anderson, J. A.; Solymosi, F., *J. Chem. Soc., Faraday Trans.* **1991,** 87, 3435.

(33) Cavers, M.; Davidson, J. M.; Harkness, I. R.; Rees, L. V. C.; McDougall, G. S., *J. Catal.* **1999,** 188, 426.

(34) Kiss, J. T.; Gonzalez, R. D., *J. Phys. Chem.* **1984,** 88, 898.

(35) Newton; Dent, A. J.; Diaz-Moreno, S.; Fiddy, S. G.; Jyoti, B.; Evans, J., *Chem. Eur. J.* **2006,** 12, 1975.

(36) Oh, S. H.; Eickel, C. C., *J. Catal.* **1991,** 128, 526.

(37) Oh, S. H.; Fisher, G. B.; Carpenter, J. E.; Goodman, D. W., *J. Catal.* **1986,** 100, 360.

(38) Solymosi, F.; Pasztor, M., *J. Phys. Chem.* **1985,** 89, 4789.

(39) Van't Blik, H. F. J.; Van Zon, J. B. A. D.; Huizinga, T.; Vis, J. C.; Koningsberger, D. C.; Prins, R., *J. Phys. Chem.* **1983,** 87, 2264.

(40) Altman, E. I.; Gorte, R. J., *Surf. Sci.* **1988,** 195, 392.

(41) Nehasil, V.; Stara, I.; Matolin, V., *Surf. Sci.* **1997,** 377, 813.

(42) Nehasil, V.; Stara, I.; Matolin, V., *Surf. Sci.* **1996,** 352, 305.

(43) Nehasil, V.; Stara, I.; Matolin, V., *Surf. Sci.* **1995,** 333, 105.

(44) Nehasil, V.; Zafeiratos, S.; Ladas, S.; Matolín, V., *Surf. Sci.* **1999,** 433-435, 215.

(45) For sample Rh(11.3)/SBA-c, Galbraith Laboratories reported 0.018% Rh by ICP-OES, Desert Analytics 0.27% by ICP-MS, and Mikroanalytishes Labor Pascher 0.82% Rh by ICP-OES. Electron probe microanalysis analysis at UC Berkeley reported 0.84% Rh assuming Rh was the only other element present in a silica matrix with a stoichiometry of SiO_2 (8 spots analyzed).

(46) Chen, M. S.; Cal, Y.; Yan, Z.; Gath, K. K.; Axnanda, S.; Goodman, D. W., *Surf. Sci.* **2007,** 601, 5326.

(47) Gabasch, H.; Knop-Gericke, A.; Schlogl, R.; Borasio, M.; Weilach, C.; Rupprechter, G.; Penner, S.; Jenewein, B.; Hayek, K.; Klotzer, B., *PCCP* **2007,** 9, 533.

(48) Anderson, J. A., *J. Chem. Soc., Faraday Trans.* **1991,** 87, 3907.

(49) Cavanagh, R. R.; Yates, J. T., *J. Chem. Phys.* **1981,** 74, 4150.

(50) Dubois, L. H.; Somorjai, G. A., *Surf. Sci.* **1980,** 91, 514.

(51) Harrod, J. F.; Roberts, R. W.; Rissmann, E. F., *J. Phys. Chem.* **1967,** 71, 343.

(52) Rice, C. A.; Worley, S. D.; Curtis, C. W.; Guin, J. A.; Tarrer, A. R., *J. Chem. Phys.* **1981,** 74, 6487.

(53) Solymosi, F.; Rasko, J.; Bontovics, J., *Catal. Lett.* **1993,** 19, 257.

(54) Yates, J. T.; Duncan, T. M.; Worley, S. D.; Vaughan, R. W., *J. Chem. Phys.* **1979,** 70, 1219.

(55) Gong, X. Q.; Liu, Z. P.; Raval, R.; Hu, P., *J. Am. Chem. Soc.* **2004,** 126, 8.

Chapter 9: Conclusions and Future Directions

9.1 Conclusions

In this dissertation, I have studied colloidally synthesized Pt and Rh nanoparticles for use in hydrogenation reactions and in the oxidation of CO by O_2. Pt nanoparticles were synthesized over the size range of 1.7 – 7.1 nm and also with shape control – cubes, cuboctahedra, and octahedra of ~ 10 nm each, all of which were stabilized with poly(vinylpyrrolidone) (PVP). Rh nanoparticles were synthesized in the size range of 1.9 – 13.5 nm and all particles were terminated by (111) faces and were also stabilized by PVP. Both Pt and Rh nanoparticles were supported on mesoporous silica SBA-15 for catalytic tests, and Rh nanoparticles were also supported on silicon wafers as 2-dimensional model catalyst. SBA-15 supported nanoparticle catalysts were characterized using transmission electron microscopy, X-ray diffraction and small angle X-ray scattering, thermogravimetric analysis, elemental analysis by electron probe microanalysis and atomic emission spectroscopy, infrared spectroscopy, and chemisorption and physisorption. The 2-dimensional model catalysts were also characterized with electron microscopy and X-ray diffraction, as well as X-ray photoelectron spectroscopy.

PVP stabilized Pt nanoparticles of controlled size were supported on SBA-15 for the study of gas phase crotonaldehyde hydrogenation by colloidally synthesized Pt nanoparticles. The turnover frequency for the disappearance of crotonaldehyde as well as the formation of each product – butyraldehyde, crotyl alcohol, butanol, and C_3 hydrocarbons – were monitored between 353 and 393 K after *ex situ* calcination in O_2 and *in situ* reduction in H_2. The turnover frequency over the largest particles (7.1 nm)

was more than twice the turnover frequency for the smallest particles (1.7 nm), increasing from 2.1×10^{-2} to 4.8×10^{-2} s^{-1} with increasing particle size. Additionally, the selectivity towards crotyl alcohol, the desired product, increases from 14% to 34% with increasing particle size. The apparent activation energy, on the other hand, remained constant at ~ 11 kcal/mol independent of particle size. The affect of reduction temperature was also studied over 1.7 and 7.1 nm Pt nanoparticles. At reduction temperatures of 673 – 723 K, the turnover frequency and selectivity to crotyl alcohol both reach a maximum. TEM analysis indicates that there is no sintering of Pt nanoparticles and it is known that there is no metal support interaction between Pt and SiO_2. Thus, the dependence on reduction temperature is attributed to an interaction between crotonaldehyde and residual carbon from PVP decomposition on the Pt nanoparticle surface.

The dependence of catalytic selectivity over Pt nanoparticles over the same range of sizes was also studied for the reaction of cyclohexene in excess hydrogen – hydrogenation to cyclohexene and dehydrogenation to benzene. The temperature dependence of the reaction is characterized by three regimes: hydrogenation only at low temperature (≤400 K); simultaneous hydrogenation and dehydrogenation at intermediate temperatures ($400 \leq T \leq 550$ K), and predominantly dehydrogenation at high temperatures (> 550 K). During simultaneous hydrogenation-dehydrogenation, the rate of hydrogenation decreases with increasing temperature (non-Arrhenius behavior), while benzene formation behaves in a normal Arrhenius manner. The rate of dehydrogenation of cyclohexene to benzene decreases monotonically over the experimental particle size and the apparent activation increases linearly as the metallic dispersion increases. The hydrogenation of cyclohexene to cyclohexane is structure-insensitive under conditions of

reversible H_2 adsorption at low temperatures, but becomes structure sensitive at high temperatures due to a particle size dependence on reactive hydrogen coverage. The selectivity was particle size dependent in the pressure regime studied here (H_2:C_6H_{10} = 20-60) due to a particle-size reactive hydrogen coverage dependence that causes the hydrogenation pathway to become structure sensitive at temperatures where the dehydrogenation of cyclohexene to benzene is structure sensitive.

In a study of Pt nanoparticles of different shapes (cubes, cuboctahedra, and octahedra), it was previously shown that the Ag used for control of shape remained somewhere in the catalysts and poisoned hydrogenation activity associated with Pt. In order to obtain shape controlled Pt nanoparticles which are catalytically active, a method for the removal of Ag from the Pt nanoparticle catalysts was developed which retained the shape of the Pt nanoparticles. SBA-15 supported Pt nanoparticles were etched in nitric acid between 7 and 15 M, which greatly reduced the amount of Ag present (below detectable limits for high nitric acid concentrations) without disruption of the SBA-15 mesoporous structure or the shape of the nanoparticles. Concurrent with the decrease in Ag content, the turnover frequency for ethylene hydrogenation increased from 0.01 s^{-1} before etching to 28 s^{-1} after etching for a sample of Pt octahedra, further confirming the removal of Ag from the shape controlled Pt nanoparticles.

Rh nanoparticles between 1.9 and 13.5 nm were synthesized using $Rh(acac)_3$ as the metal precursor, PVP as a stabilizing polymer, and 1,4-butanediol as the solvent and reducing agent. Control of size and morphology was achieved by reducing the Rh precursor under Ar for 2 h and carefully controlling the reaction conditions. Rh nanoparticles between 5.4 and 13.5 nm were synthesized by varying the concentration of

$Rh(acac)_3$ between 0.313 mM (5.4 nm particles) and 5 mM (10.7 and 13.5 nm particles). The temperature was also varied between 468 and 498 K to further control the particle size. The synthesis of smaller Rh nanoparticle was achieved by the addition of sodium citrate between 0.25 mM (5.1 nm particles) and 15 mM (1.9 nm particles) at a constant concentration of $Rh(acac)_3$ and PVP and at a constant temperature.

The Rh nanoparticles were supported on silicon wafers as model catalysts and used for the hydrogenation of ethylene and oxidation of CO by O_2. The turnover frequency for ethylene hydrogenation was ~ 0.5 s^{-1} for all particles between 6.5 and 10.7 nm at reaction conditions of 20 Torr ethylene, 200 Torr H_2, and at 350 K. Ethylene hydrogenation rates were similar to those measured over other Rh catalysts and it was therefore determined that these Rh nanoparticles are good model catalysts for the investigation of particle size effects by colloidally synthesized Rh nanoparticles.

The turnover frequency measured for CO oxidation at 50 Torr O_2, 20 Torr CO, and at 573 K is 5.5 times higher over 11.3 nm Rh nanoparticles than over Rh foil measured in the same way. The turnover frequency for 1.9 nm Rh particles is 28 times that of Rh foil. The apparent activation energy also decreased from 27.9 to 19.0 kcal mol^{-1} as the particle size decreased from 11.3 to 1.9 nm. In order to help explain this particle size dependence, synchrotron based X-ray photoelectron spectroscopy was performed during CO oxidation at 200 mTorr CO and 500 mTorr O_2. Under these conditions, smaller (1.9 nm) Rh nanoparticles exhibited 0.6 of a monolayer of oxidized Rh at 423 K and a full layer of oxidized Rh at 473 K. Larger (7.1 nm) Rh nanoparticles contained only 0.2 and 0.6 of a monolayer at 423 K and 473 K, respectively. The deeper oxidation of smaller particles coincides with an increase in the reaction rate. A simple

thermodynamic model for the oxidation of metal nanoparticles was also developed, which demonstrates that smaller nanoparticles oxidize more easily than larger nanoparticles.

A series of Rh nanoparticles between 1.9 and 11.3 nm was also supported on mesoporous silica SBA-15 for a continued study of the size dependence of CO oxidation as well as a study of the role of PVP in gas phase catalysis. The deposition of the particles on SBA-15 allows for the ability to treat the nanoparticles at high temperatures in O_2 and/or H_2 without sintering of the particles, which occurs easily on the silicon wafers. PVP stabilized Rh NP catalysts were studied for CO oxidation before and after calcination in O_2 at ~ 673 K. We have concluded that (1) uncalcined PVP stabilized Rh NP catalysts exhibit a higher turnover frequency for CO oxidation than calcined catalysts by a factor of 2 – 5, (2) CO oxidation turnover frequency increases from 0.39 to 1.52 s^{-1} with decreasing particle size from 11.3 to 1.9 nm for uncalcined catalysts, but CO oxidation is particle size independent for calcined catalysts (~ 0.25 s^{-1} for all samples), and (3) CO adsorbs at bridge sites before the catalysts are calcined, but on atop sites after calcination, with or without reduction in H_2 as monitored by infrared spectroscopy. By comparing infrared studies to turnover frequency measurements for CO oxidation, we propose that PVP affects how CO binds to Rh and thus affects the turnover frequency for CO oxidation.

9.2 Future Directions

The main focus of this work has been on how the particle size of Pt and Rh nanoparticles affects catalytic activity and selectivity by using PVP stabilized colloidally synthesized nanoparticles. This work is continuing in our laboratory for the study of

addition model reactions such as pyrrole hydrogenation and the synthetic procedures for nanoparticle synthesis are widening to include synthesis of Rh and Pt nanoparticles using dendrimers as organic templates as well as synthesis of bimetallic and trimetallic noble metal nanoparticles using either PVP or dendrimers as stabilizers.

In the course of this research, it has become evident that PVP plays a role in gas phase heterogeneous reactions that is important and can either increase or decrease catalytic performance. With an increased interest in colloidally synthesized nanoparticles for use in catalysis, understanding how the stabilizing molecule interacts with the metal nanoparticle and with reactants and products during catalysis will be very important. An in-depth investigation of this phenomenon should involve the study of multiple metal nanoparticles and multiple stabilizing molecules in addition to PVP. *In situ* techniques such as infrared spectroscopy and ambient pressure X-ray techniques such as photoelectron spectroscopy and X-ray absorption spectroscopy can be used to probe the nature of the stabilizer, metal, and reactant molecules during reaction. Careful consideration of stabilizing molecule and pretreatment may lead to the development of another route for control of catalytic performance for specialized reactions.

We have also recently been studying bimetallic nanoparticles using ambient pressure X-ray photoelectron spectroscopy. This has allowed us to elucidate the structure of the bimetallic nanoparticles during catalytic reactions – specifically CO oxidation by NO or O_2 – such as core/shell or homogeneous mixture. Using this technique, it may be possible not only to study working catalysts during gas phase reactions, but also understand surface segregation and diffusion in nanostructures. While many studies

indicate that alloying and diffusion are both affected by reducing dimensions to the nanoscale, neither is understood at these small dimensions.